



ITNT - 2022



**SAMARA
UNIVERSITY**

VIII International Conference on Information Technology and Nanotechnology (ITNT-2022), Samara (Russia), 23-27 May, 2022

A review on radial carpet beams (RCBs) and some new studies on the self-healing of the RCBs

Saifollah Rasouli

(Institute for Advanced Studies in Basic Sciences, Iran)



**Institute for Advanced Studies
in Basic Sciences**
Gava Zang, Zanjan, Iran

The VIII International Conference on Information Technology and Nanotechnology

23-27 May, 2022

Samara, Russia

- **First, I would like to thank to the organizing committee of this valuable scientific activity for the invitation and letting me this opportunity to have a talk in this activity.**
- **One of the (good) effects of the COVID-19 epidemic is that many international meetings are held in the cyberspace, by saving the time of the attendees without paying any considerable costs! This is a new opportunity to increase the scientific contacts and collaborations.**



**Institute for Advanced Studies
in Basic Sciences**
Gava Zang, Zanjan, Iran

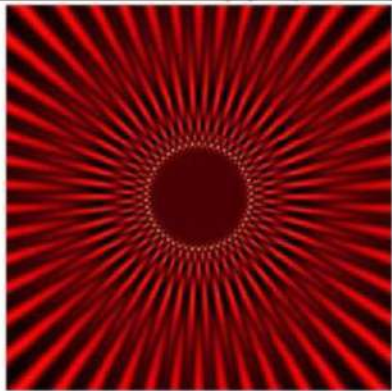


**Department of Physics,
Institute for Advanced Studies in Basic Sciences(IASBS),
Zanjan, Iran.**

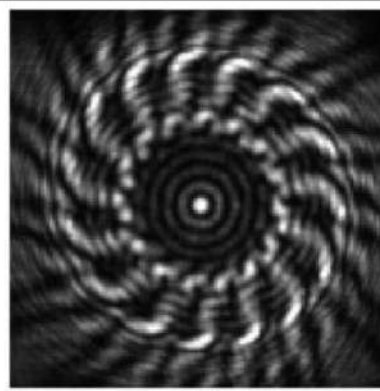


Outline:

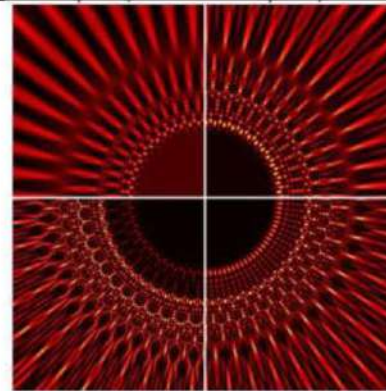
- **Fresnel and Fraunhofer approximations**
 - Talbot effect under diffraction of a plane wave from a periodic structure
 - Realization of the Talbot carpet in the longitudinal plane
- **Diffraction of plane wave from amplitude radial gratings**
 - Talbot carpet at the transverse plane
 - Curved boundaries between optical regimes
- **Rotatable annular multiple trapping with radial carpet beams**
- **Colorful radial Talbot carpet at the transverse plane**
- **Diffraction of plane wave from radial phase gratings**
 - **Radial carpet beams: A class of nondiffracting, accelerating, and self-healing beams**
 - Self-healing of carpet beams, self-reconstruction of a removed main lobe under propagation
- **Combined half-integer Bessel-like beams: A set of solutions of the wave equation**
 - Radial carpet beams
 - Petallike beams,
 - Ringlike vortex beams or twisted-intensity ringlike vortex beams
- **Controlled intensity sharing among different diffraction orders**
- **Talbot effect of azimuthally periodic Bessel-based structures**



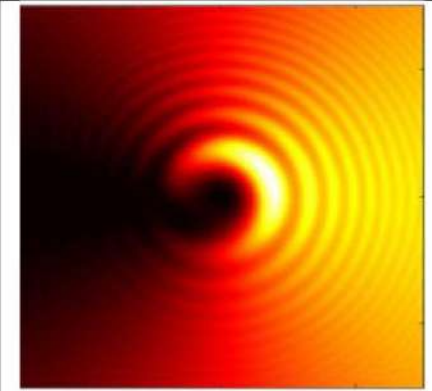
Transverse plane Talbot carpet



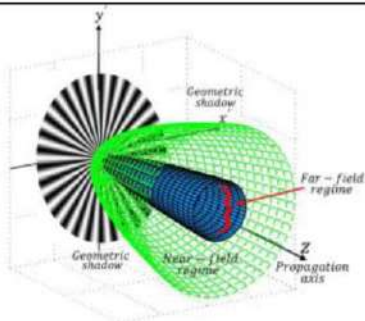
Arago-Poisson-like spot



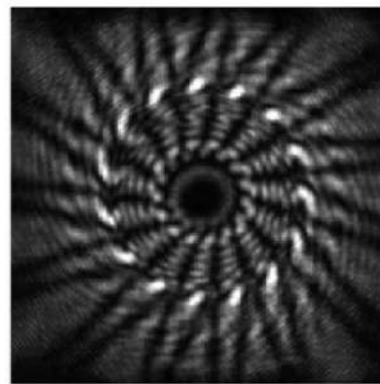
(quarter parts of) radial carpet beams



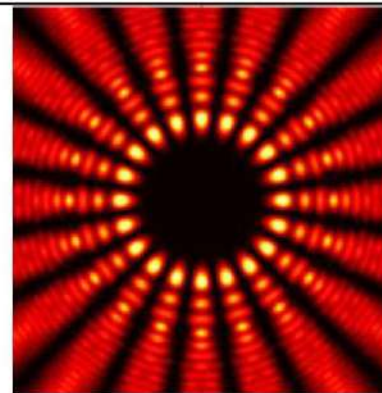
spatially asymmetric beam



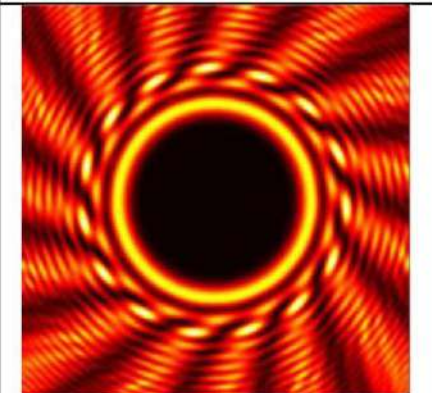
curved boundaries between the optical regimes



in the absence of the Arago-Poisson-like spot



Petallike beam



twisted-intensity ringlike vortex beam

Fig.1: Illustration of transverse plane Talbot carpet, curved boundaries between the optical regimes, Arago-Poisson-like spot, and intensity profiles of spatially asymmetric, radial carpet, petallike, and twisted-intensity ringlike vortex beams.

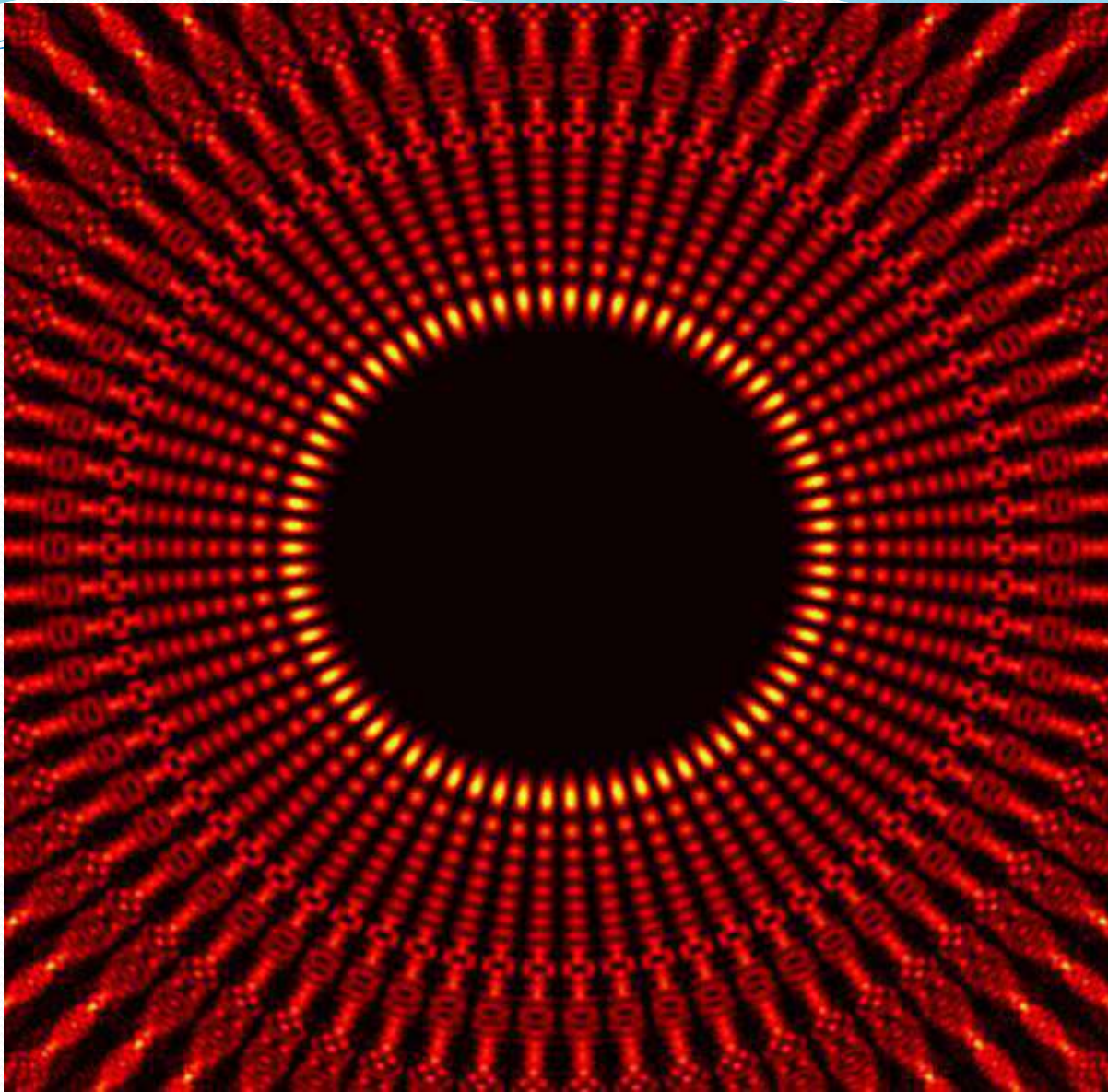
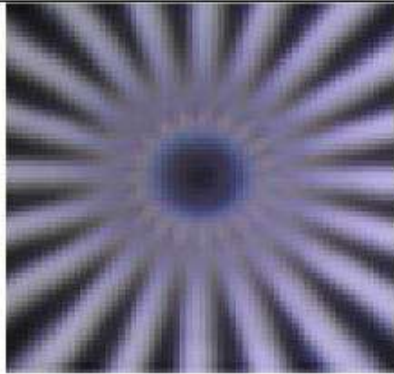
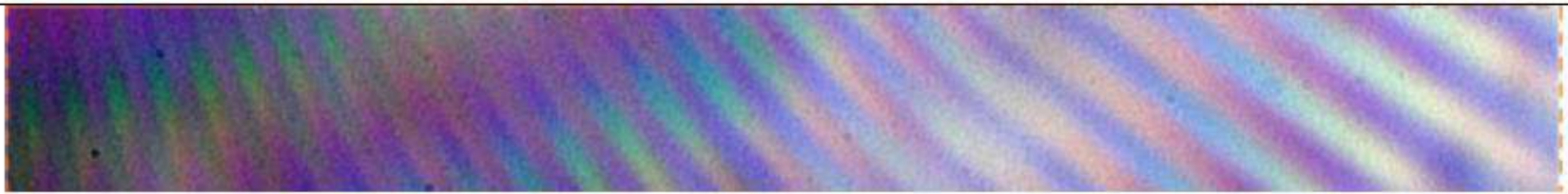
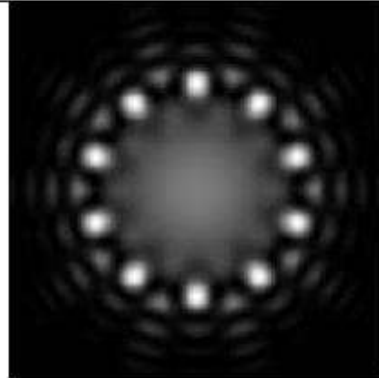


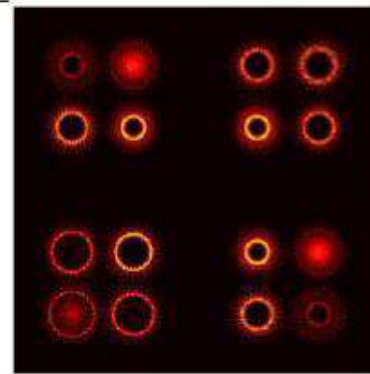
Fig.2 Intensity profile at the transverse plane of a radial carpet beam that can be produced in the diffraction of a plane wave from a binary radial phase grating. The number of spokes, amplitude of phase variation, and aperture ratio of the grating respectively are $m = 35$, $\gamma = \pi/2$, and $h=1/2$.



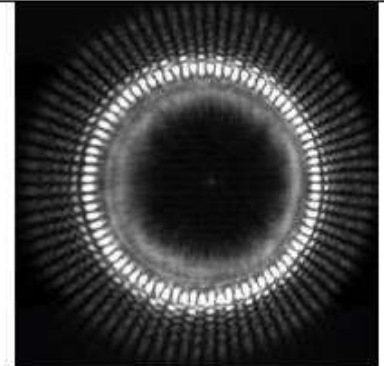
White light Talbot carpet at the transvers plane



Rotatable annular multiple trapping



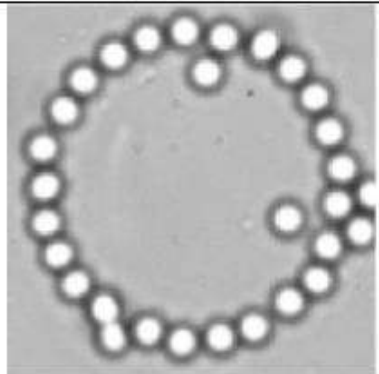
Diffraction from phase hologram radial gratings



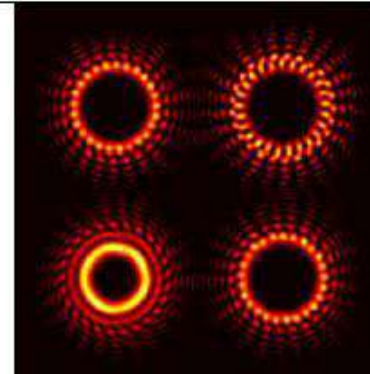
Propagation of RCBs through atmospheric turbulence



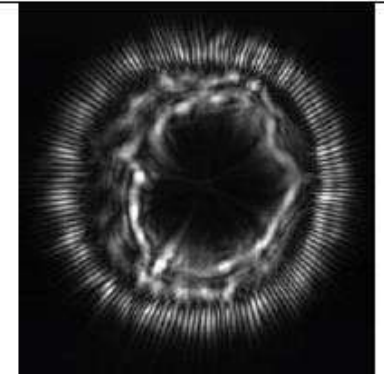
Diffraction-based rainbow and radial grating-based spectrometry



Rotatable annular multiple trapping



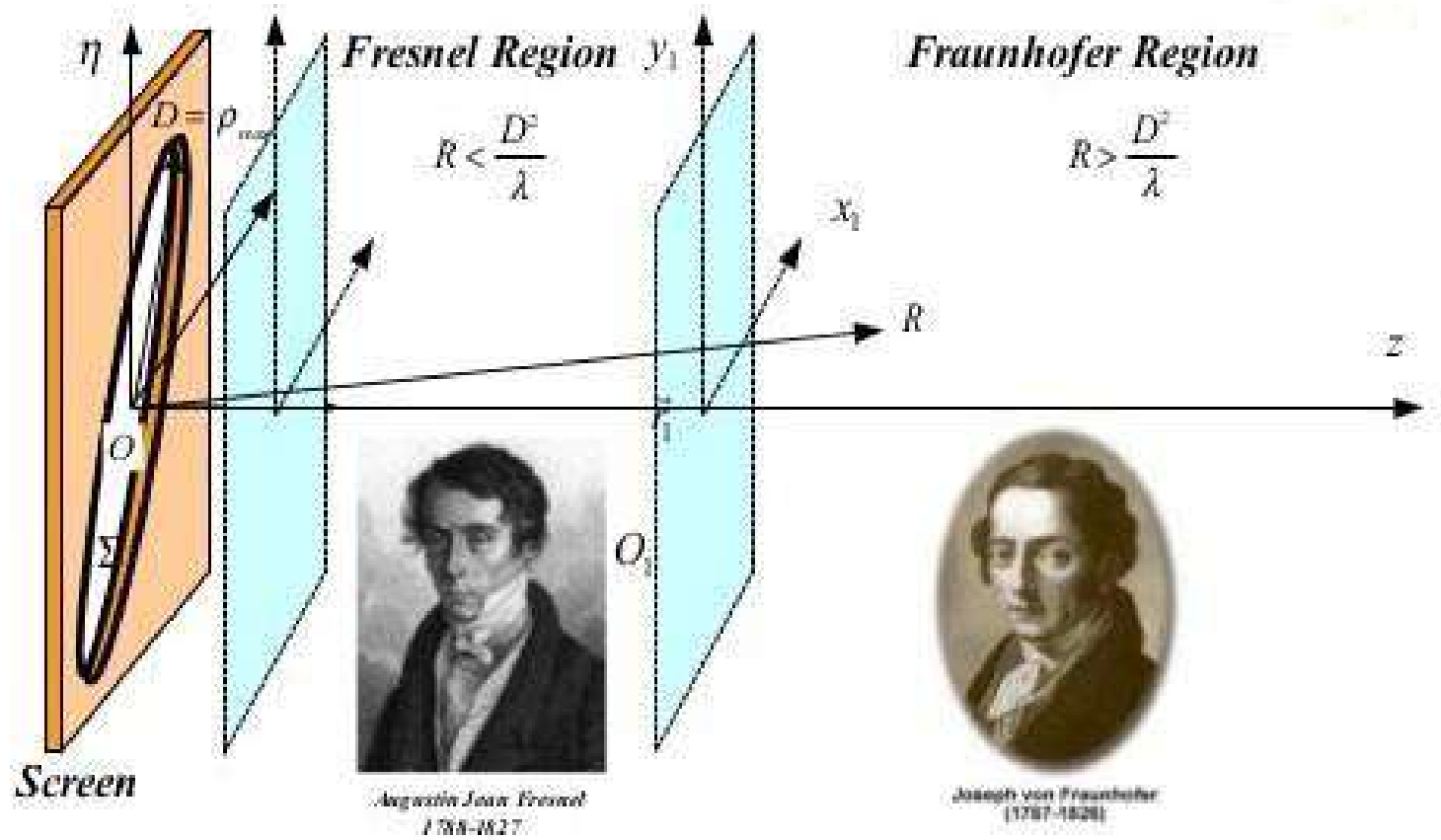
Family of beams



RCBs-based communication

Fig.3: Illustration of white light Talbot carpet and diffraction-based rainbow, rotatable annular multiple trapping, generation of family beams, propagation of RCBs through atmospheric turbulence and RCBs-based communication.

Diffraction, Fresnel and Fraunhofer approximations



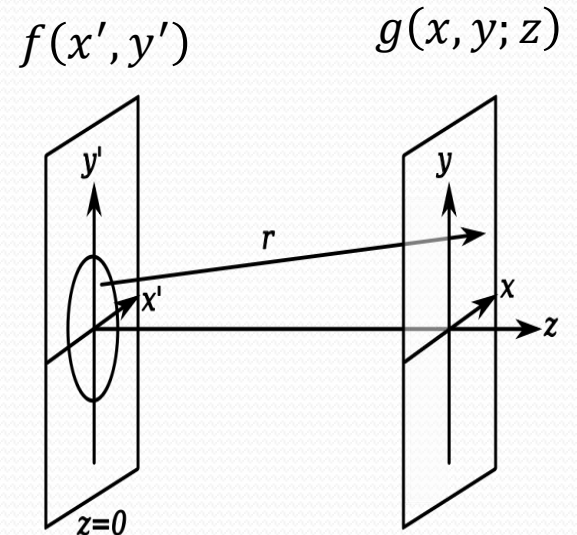
Near- and far- field diffraction



Augustin Fresnel
(1788-1827)

$$g(x, y; z) = h_0 \iint_{-\infty}^{\infty} f(x', y') \exp \left\{ \frac{i\pi}{\lambda z} [(x - x')^2 + (y - y')^2] \right\} dx' dy'.$$

$$h_0 = \frac{\exp(ikz)}{i\lambda z}$$



$$g_{Far}(x, y; z) = h_0 F(\xi, \eta) \Big|_{\xi = \frac{x}{\lambda z}, \eta = \frac{y}{\lambda z}}$$

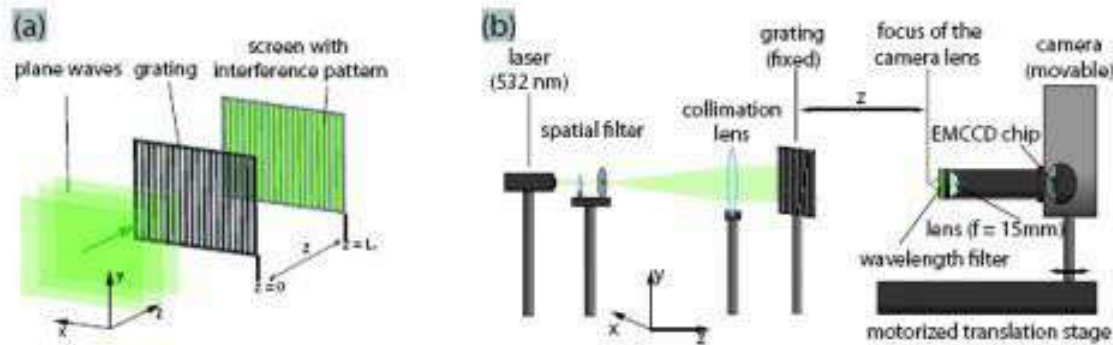
$$F(\xi, \eta) = \mathcal{F}_2\{f(x, y)\}$$

$$= \iint_{-\infty}^{\infty} f(x, y) \exp[-2i\pi(\xi x + \eta y)] dx dy$$

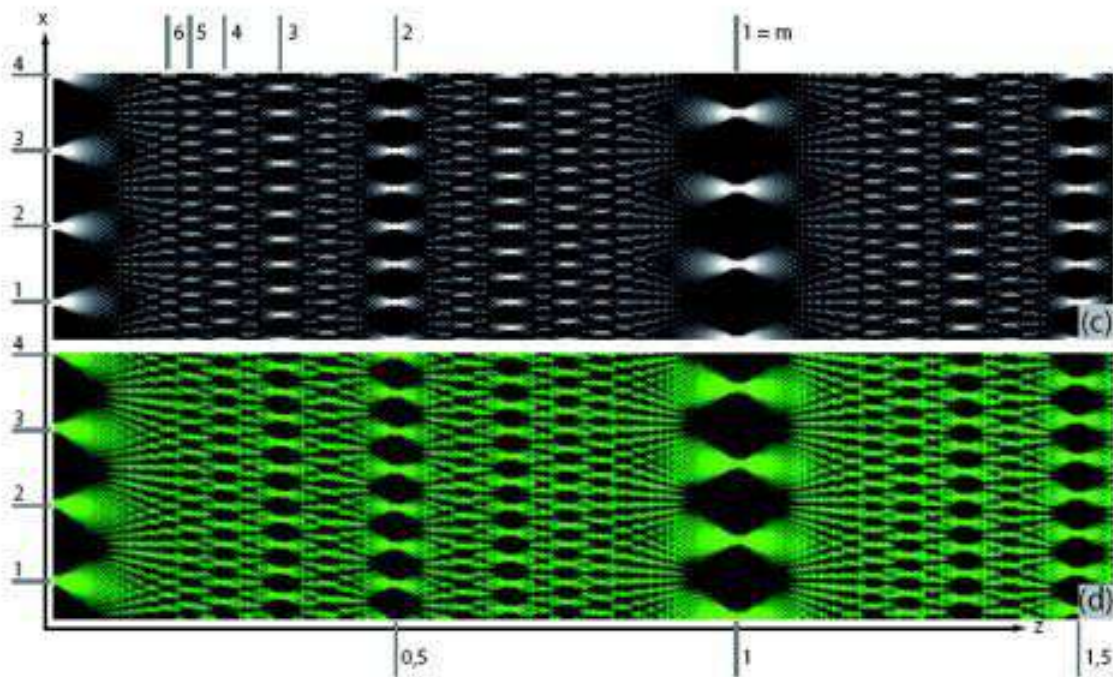


Joseph von Fraunhofer
(1787-1826)

Talbot effect and realization of the Talbot carpet in the longitudinal plane



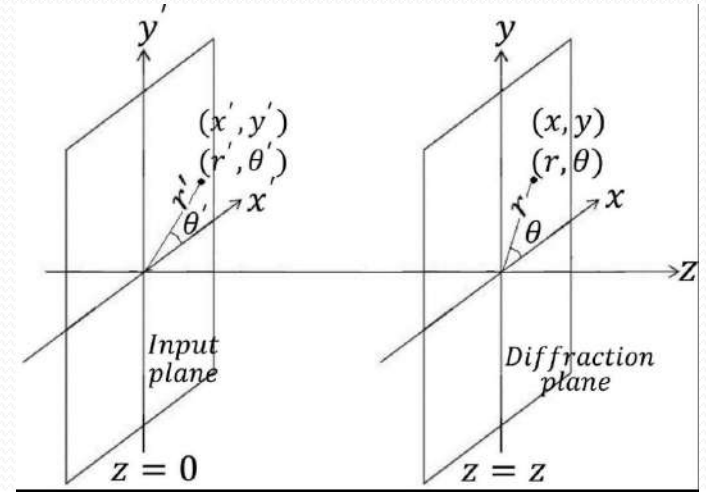
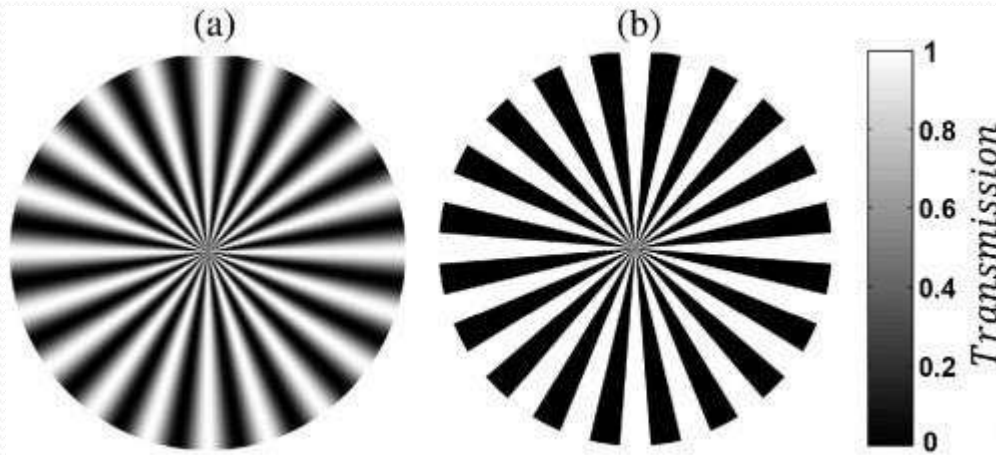
Talbot effect under a monochromatic light illumination: The coherent, lensless self-imaging of light fields, was discovered by Henry Fox Talbot in 1936.



Talbot carpet can be shown when a plane wave diffracting through a grating, and a carpet like pattern can be imagine in the plain of the propagation axis and grating vector by displacing the recording camera long propagation direction.

Talbot carpet at the transverse plane produced in the diffraction of plane wave from amplitude radial gratings

Diffraction of plane wave from amplitude radial gratings



$$g(r, \theta) = h_0 e^{i\alpha r^2} \int_0^\infty \int_0^{2\pi} r' dr' d\theta' f(r', \theta') e^{i\alpha r'^2} e^{-2i\alpha r r' \cos(\theta' - \theta)}$$

$$h_0 = \frac{1}{iz\lambda} \exp(ikz)$$

$$\alpha = \frac{\pi}{z\lambda}$$

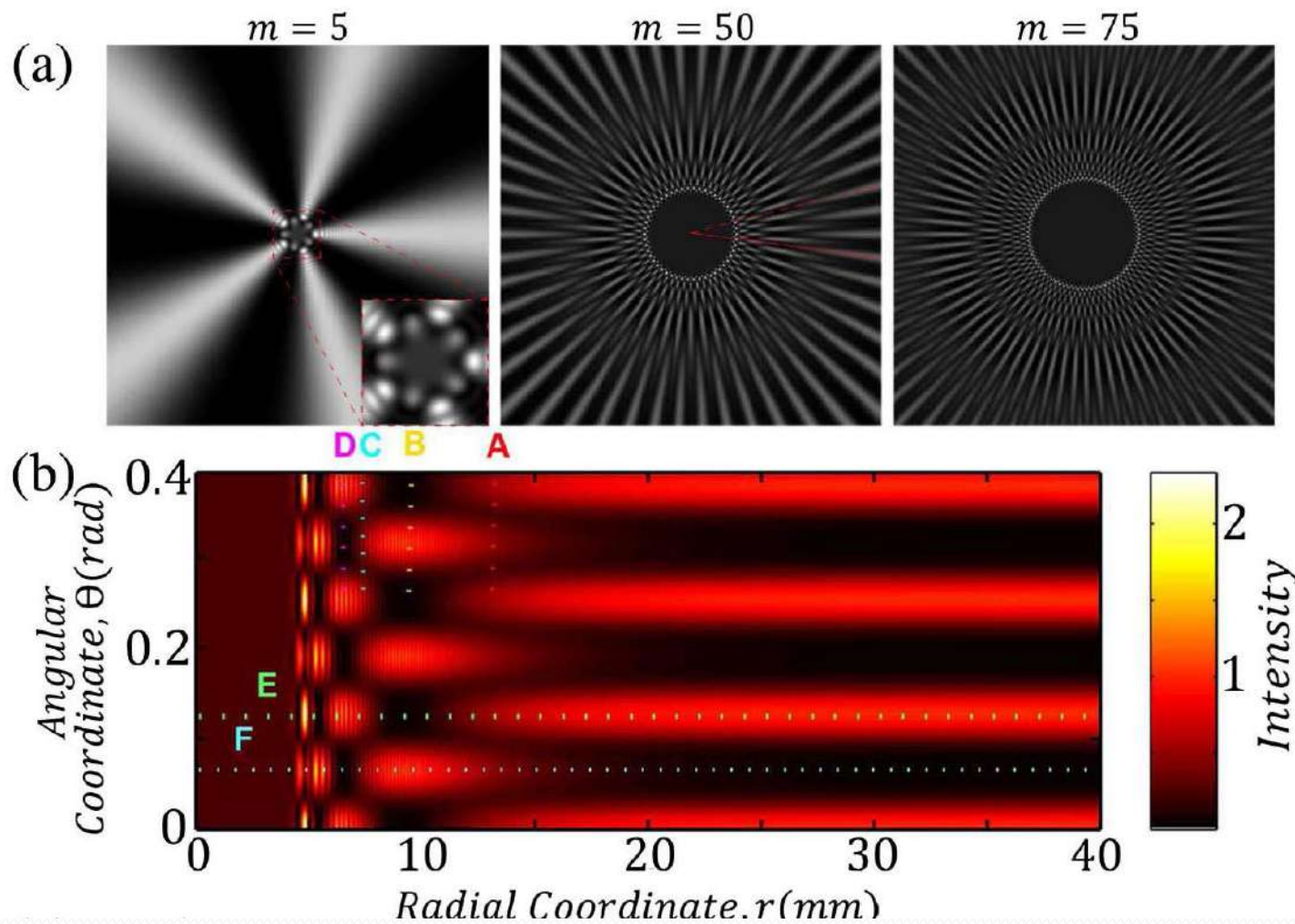
$$f(r', \theta') = f_R(r') f_\Theta(\theta')$$

$$f_\Theta(\theta') = \sum_{m=-\infty}^{+\infty} c_m e^{im\theta'}$$

$$g(r, \theta) = h_0 e^{i\alpha r^2} \sum_{n=-\infty}^{+\infty} c_n (-i)^n e^{in\theta} \mathcal{H}_n \{ f_R(r) e^{i\alpha r^2} \}$$

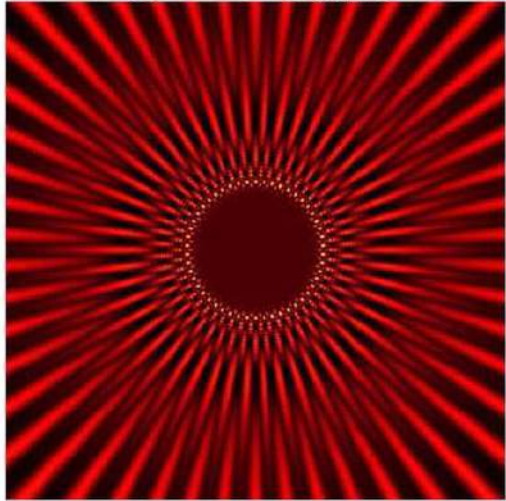
$$f_R(r) = 1 \quad t(\theta') = f_\Theta(\theta') = \frac{1}{2} [1 + \cos(m\theta')]$$

$$g(r, \theta) = \frac{e^{ikz}}{2} \times \left\{ 1 + \mathcal{R} e^{i\mathcal{R}^2} \sqrt{\frac{\pi}{2}} (-i)^{\frac{m}{2}+1} \times \left[J_{\frac{m+1}{2}}(\mathcal{R}^2) + i J_{\frac{m-1}{2}}(\mathcal{R}^2) \right] \cos(m\theta) \right\}.$$

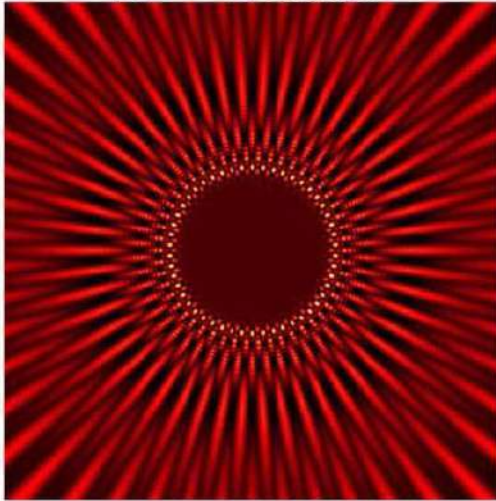


$$g(r, \theta) = \frac{e^{ikz}}{2} \times \left\{ 1 + \mathcal{R} e^{i\mathcal{R}^2} \sqrt{\frac{\pi}{2}} (-i)^{\frac{m}{2}+1} \times \left[J_{\frac{m+1}{2}}(\mathcal{R}^2) + i J_{\frac{m-1}{2}}(\mathcal{R}^2) \right] \cos(m\theta) \right\}.$$

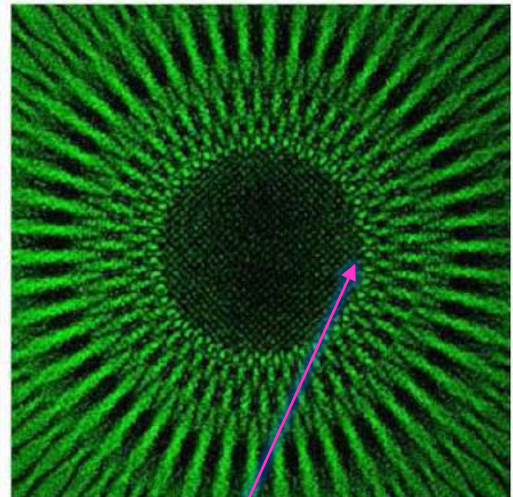
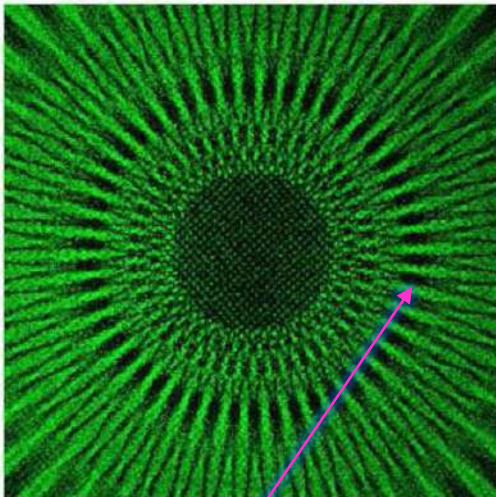
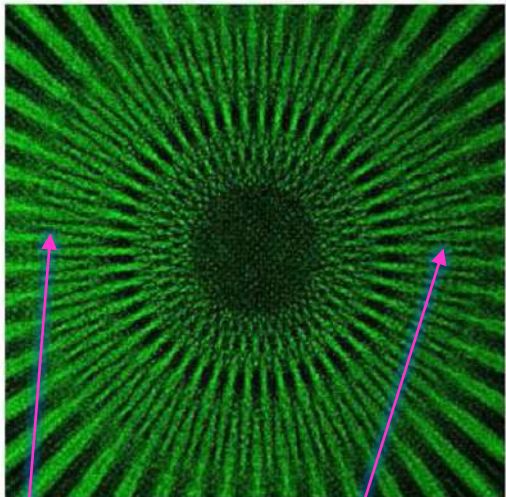
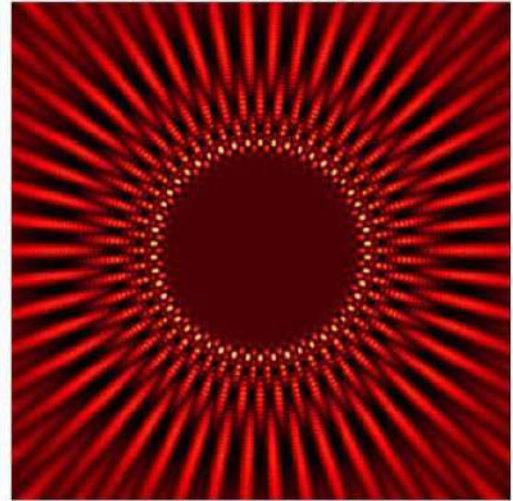
$z = 20\text{cm}$



$z = 30\text{cm}$



$z = 50\text{cm}$



First quarter-Talbot or subimage

$$r_{\text{out}} = \frac{m}{2\pi} \sqrt{2\lambda z}$$

$$r_{T1} = \frac{m}{2\pi} \sqrt{\lambda z / 2}$$

$$r_{\text{in}} = \sqrt{\frac{m\lambda z}{\pi}}$$

For a conventional grating with a period of p , its **first quarter-Talbot image** is formed at a propagation distance of

$$z = \frac{p^2}{2\lambda}$$

where λ is the wavelength of the illuminating plane wave.

For a radial grating, over an annular strip with a radius of r_{out} the spatial period in the azimuthal direction is

$$p_{\text{out}} = \frac{2\pi r_{\text{out}}}{m},$$

then, at a given propagation distance z , we have

$$r_{\text{out}} = \frac{m}{2\pi} \sqrt{2\lambda z}.$$

First Talbot image

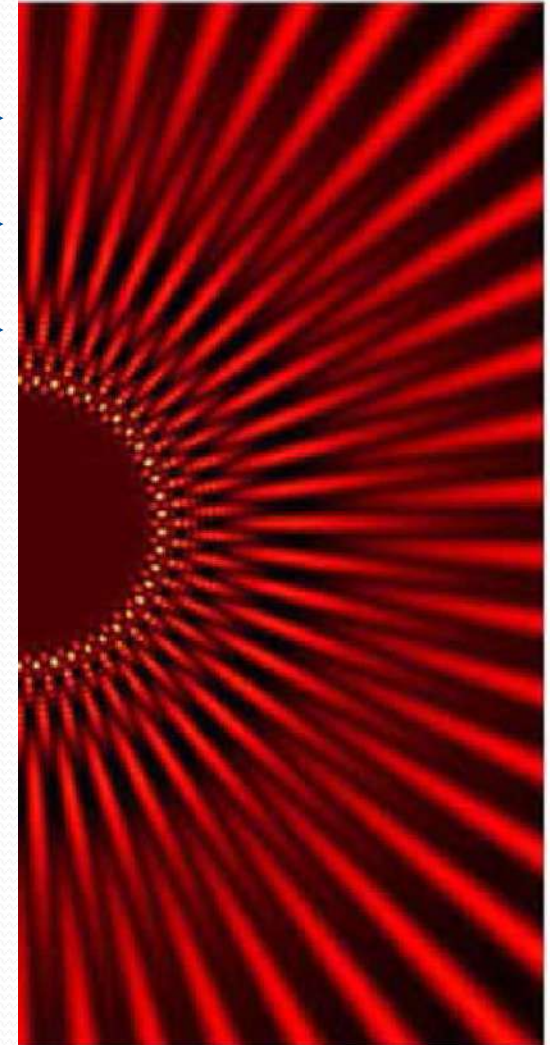
$$z_T = \frac{2p^2}{\lambda}$$

$$r_{T1} = \frac{m}{2\pi} \sqrt{\lambda z/2}.$$

First quarter-Talbot image r_{out} →

First half-Talbot image →

First Talbot image r_{T1} →



For large values of \mathbf{r} , the Bessel function can be written as

$$J_m(\mathcal{R}^2) \rightarrow \sqrt{\frac{2}{\pi\mathcal{R}^2}} \cos\left(\mathcal{R}^2 - \frac{m\pi}{2} - \frac{\pi}{4}\right)$$

$$g(r, \theta) = \frac{e^{ikz}}{2} \{1 + \cos(m\theta)\}$$

where it produces the desired geometric shadow.

For a conventional grating with a period \mathbf{p} and a lateral extension of \mathbf{d} , at propagation distances larger than

$$z = \frac{pd}{2\lambda}$$

different diffraction orders do not overlap, and there is not any interference between them (the farthest border of the near-field regime for the conventional gratings).

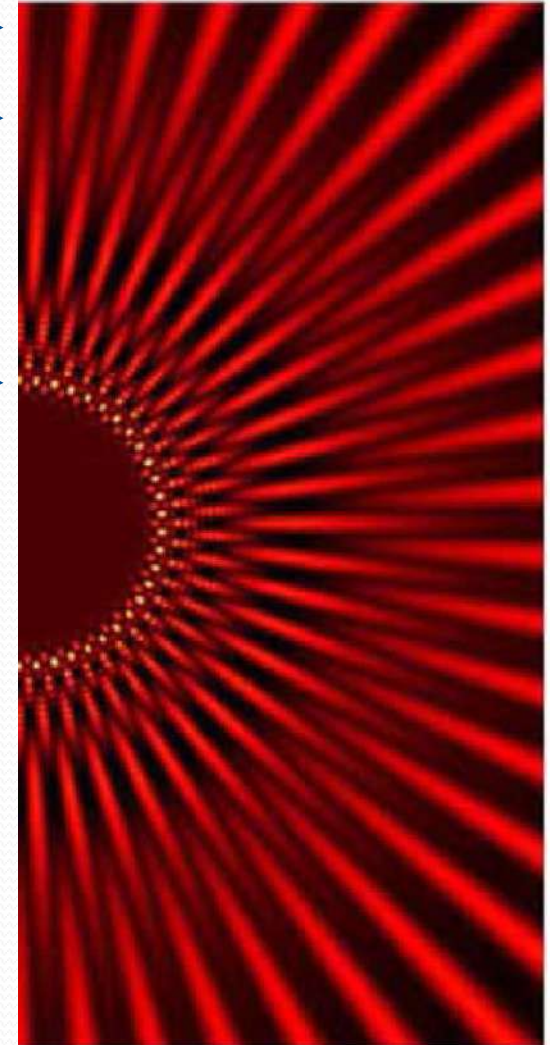
For a radial grating with a spoke number of \mathbf{m} , at a given radial of \mathbf{r} we set

$$\mathbf{d} \rightarrow \gamma \quad \text{and} \quad \mathbf{p} \rightarrow \frac{2\pi r}{m} \quad \Rightarrow \quad r_{\text{in}} = \sqrt{\frac{m\lambda z}{\pi}}$$

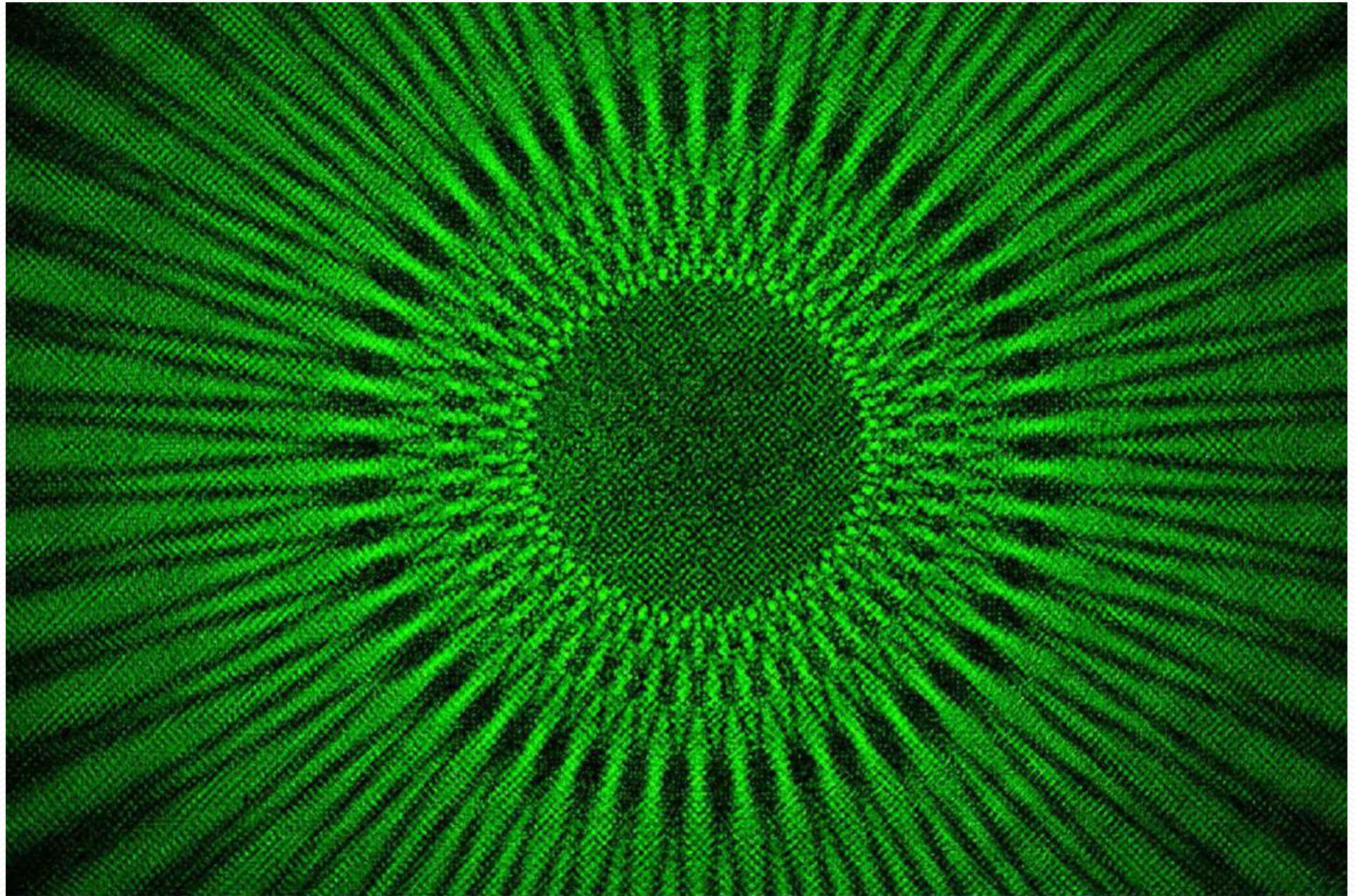
Geometric shadow \rightarrow

r_{out} \rightarrow

The inner boundary of the near-field regime r_{in} \rightarrow



Experimentally recorded Talbot carpet at the transverse plane
Diffraction from an amplitude radial grating with a sinusoidal profile



Diffraction from an Amplitude Radial Grating with a Binary Profile

$$\begin{aligned}
 t(\theta') &= \frac{1}{2} (1 + \text{sgn} \cos(m\theta')) \\
 &= \frac{1}{2} + \sum_{l=1}^{+\infty} (A_l e^{iml\theta'} + A_{-l} e^{-iml\theta'}),
 \end{aligned}$$

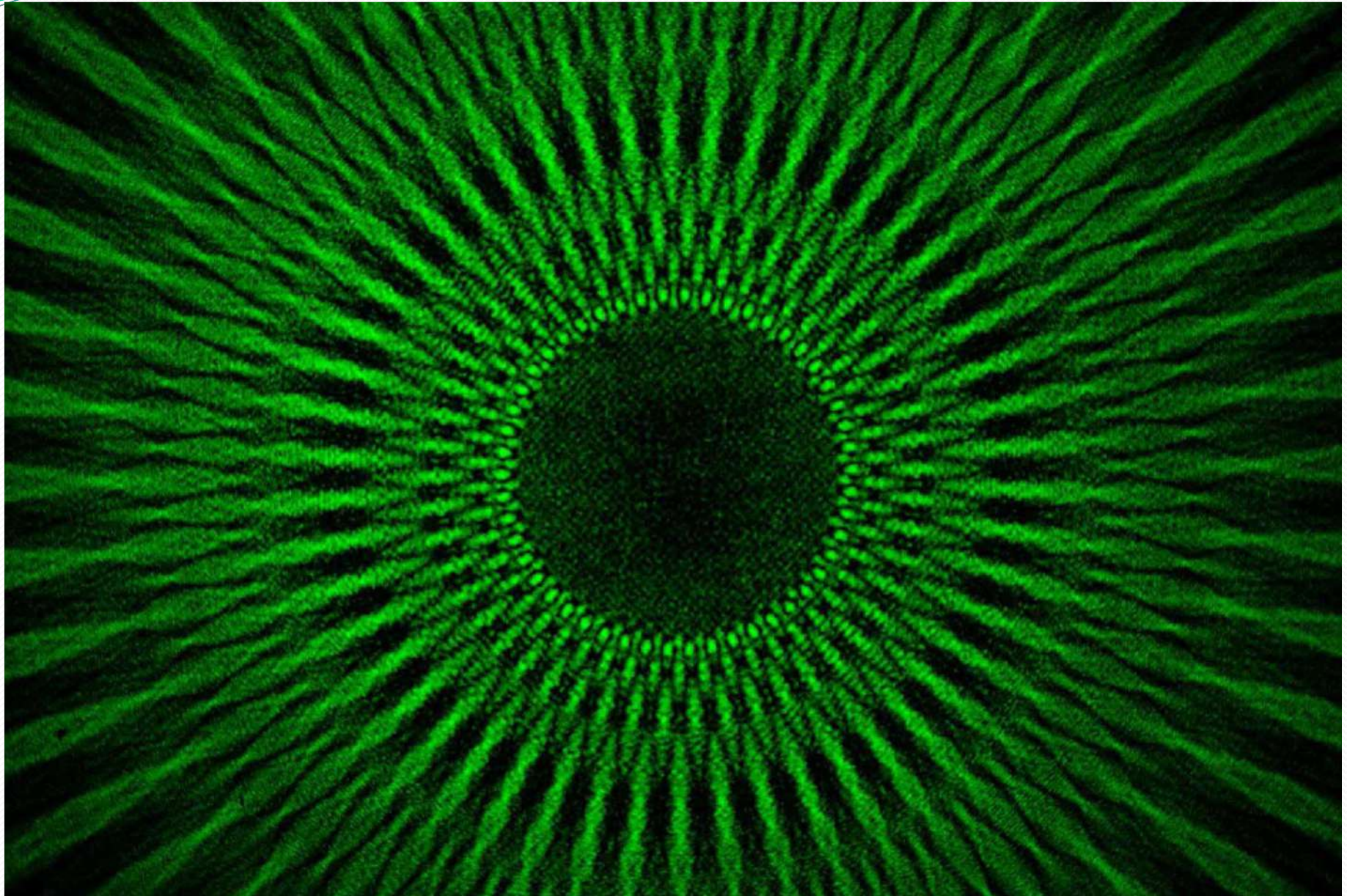
$$\bar{f}_R(r') = 1$$

$$f_{\Theta}(\theta') = \frac{1}{2} + \frac{1}{2} \sum_{l=1}^{+\infty} \text{sinc}\left(\frac{l\pi}{2}\right) (e^{iml\theta'} + e^{-iml\theta'}).$$

$$\begin{aligned}
 g(r, \theta) &= \frac{e^{ikz}}{2} \times \left\{ 1 + \mathcal{R} e^{i\mathcal{R}^2} \sum_{l=1}^{\infty} g_l \right. \\
 &\quad \left. \times \left[J_{\frac{ml+1}{2}}(\mathcal{R}^2) + i J_{\frac{ml-1}{2}}(\mathcal{R}^2) \right] \cos(ml\theta) \right\},
 \end{aligned}$$

$$g_l = \sqrt{2\pi} (-i)^{\frac{ml}{2}+1} \text{sinc}\left(\frac{l\pi}{2}\right).$$

**Experimentally recorded Talbot carpet at the transverse plane
Diffraction from an amplitude radial grating with a binary profile**



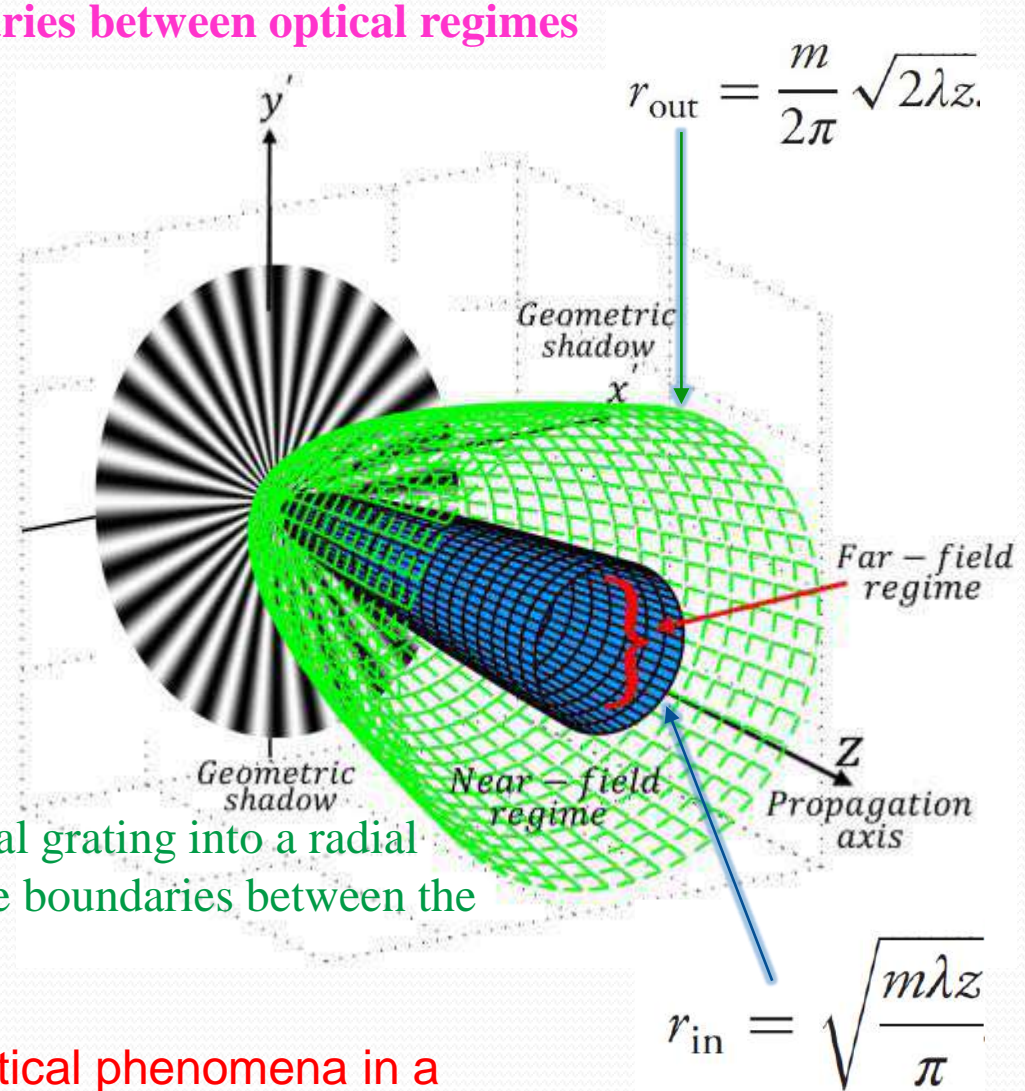
Curved boundaries between optical regimes

Splitting of the space into geometric shadow and far-field and near-field diffraction regimes for a typical amplitude radial grating:

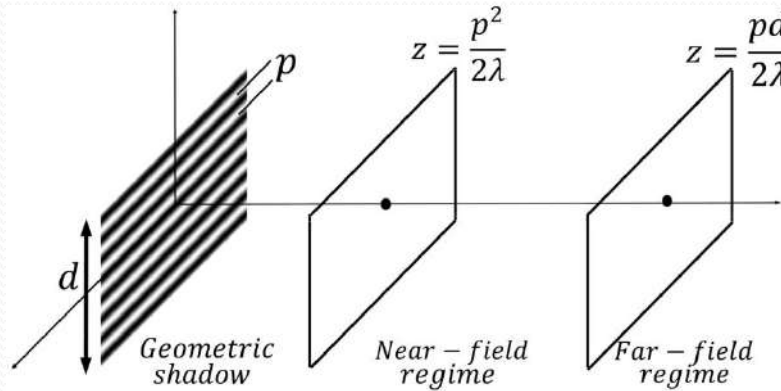
Green surface splits the geometric shadow from the near-field diffraction regime, and blue surface splits the near-field and far-field diffraction regimes from each other.

As a consequence of turning a conventional grating into a radial grating with a central singularity, the plane boundaries between the optical regimes have acquired curvature.

The possibility of a connection with optical phenomena in a gravitational field is under investigation.

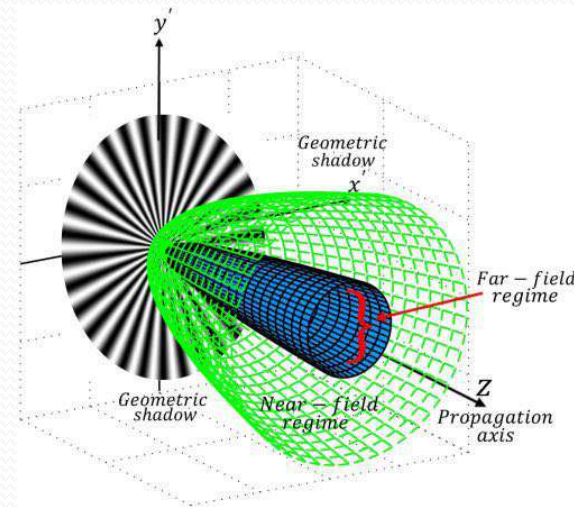


Diffraction from linear gratings:



By tuning from a conventional grating into a radial grating with a central singularity, the plane boundaries between the optical regimes now possess Gaussian curvature.

Diffraction from radial gratings:



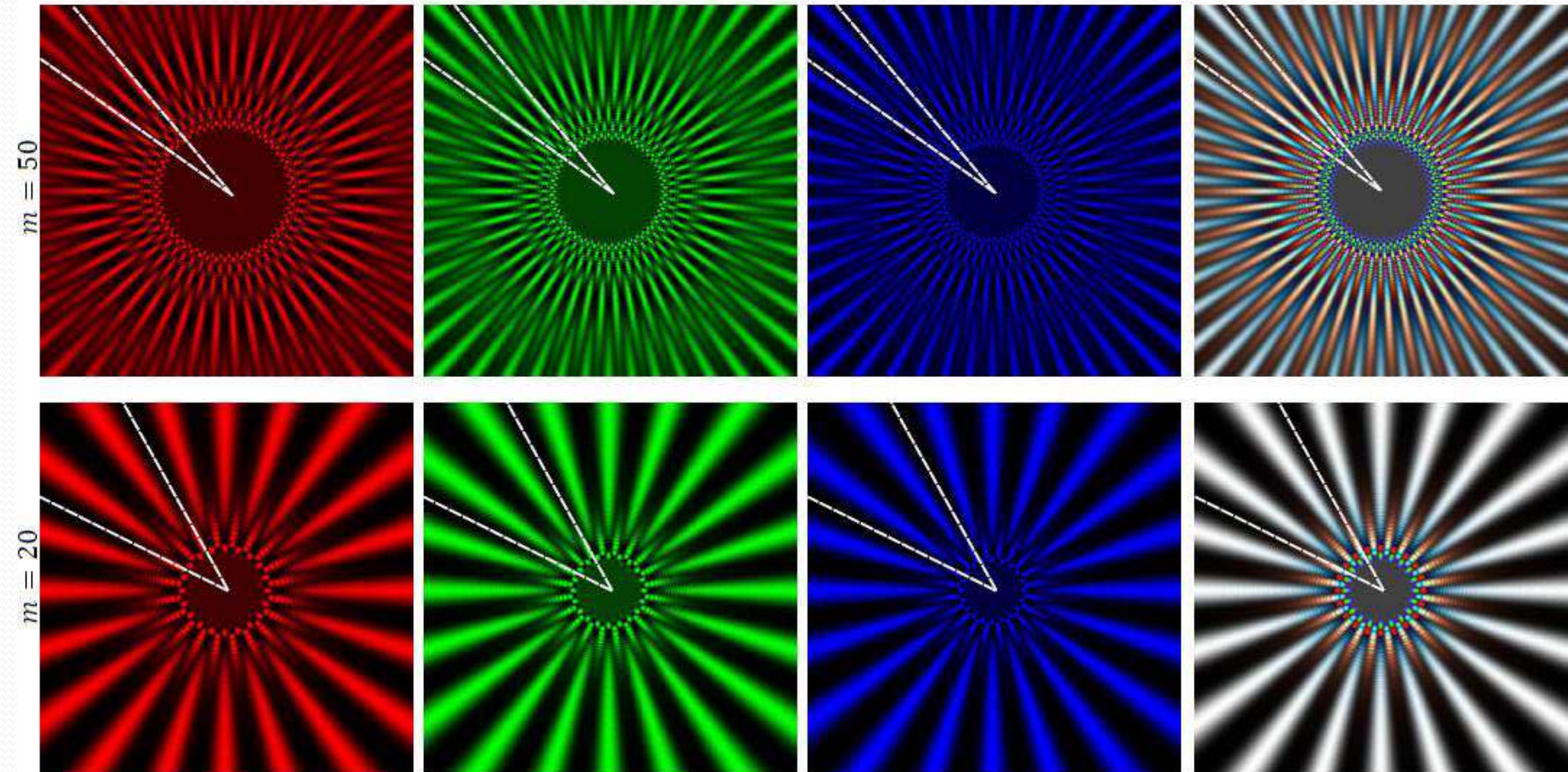
Conclusion:

As a consequence of turning a conventional grating into a radial grating with a central singularity, the plane boundaries between the optical regimes have acquired curvature.

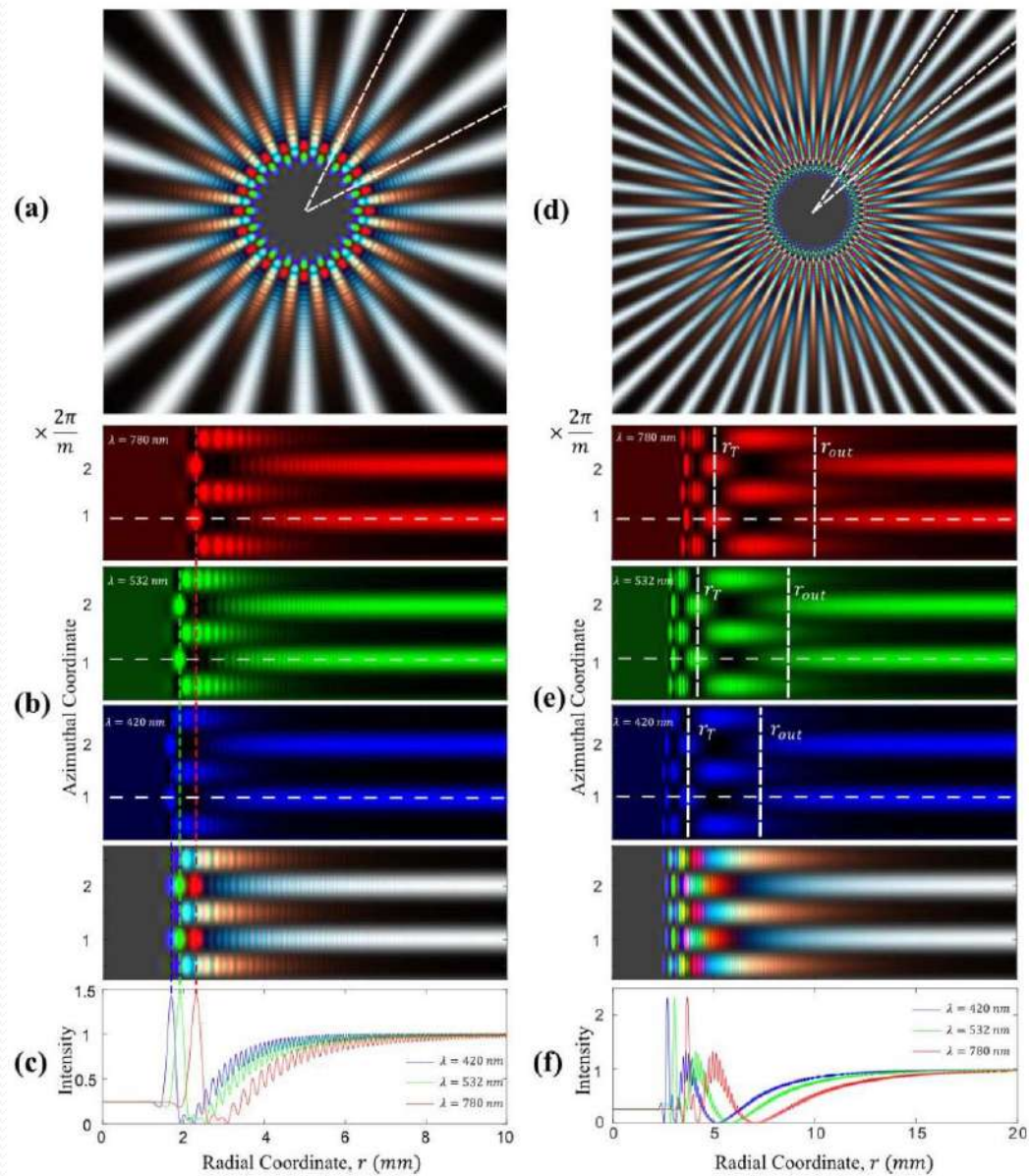
In this work, the possibility of a connection with optical phenomena in a gravitational field is investigated. We show that this turning serves as an analogue for the curved space-time of general relativity

Colorful radial Talbot carpet at the transverse plane

Diffraction-based rainbow and radial grating-based spectrometry

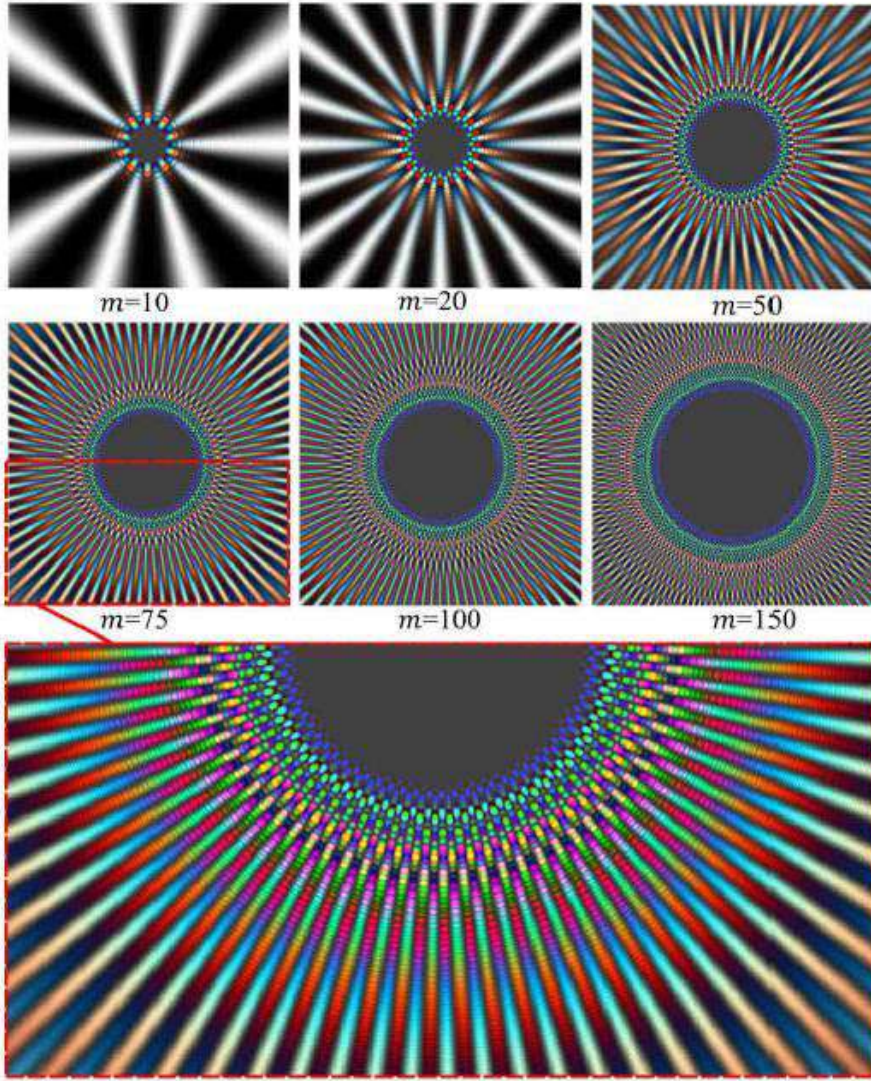


Colorful radial Talbot carpet at the transverse plane

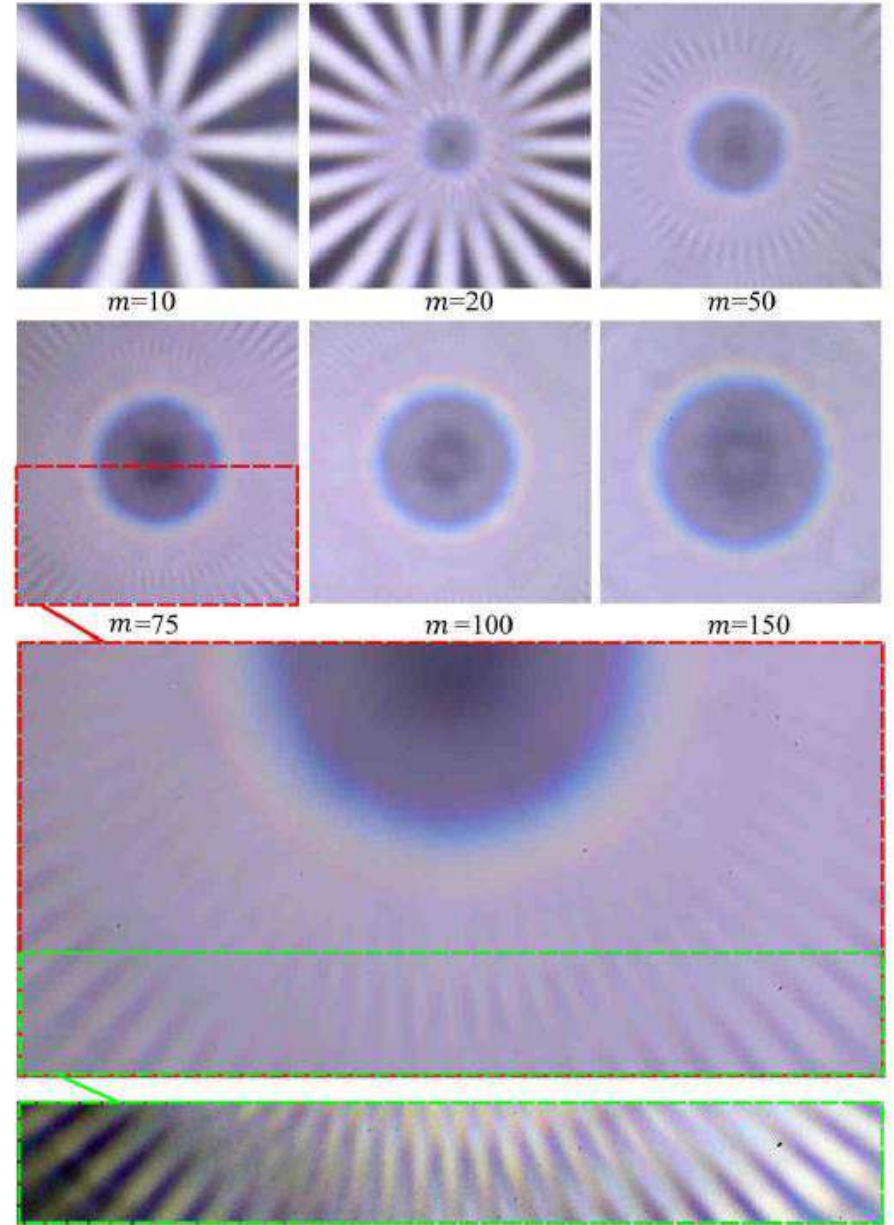


Colorful radial Talbot carpet at the transverse plane

(a)

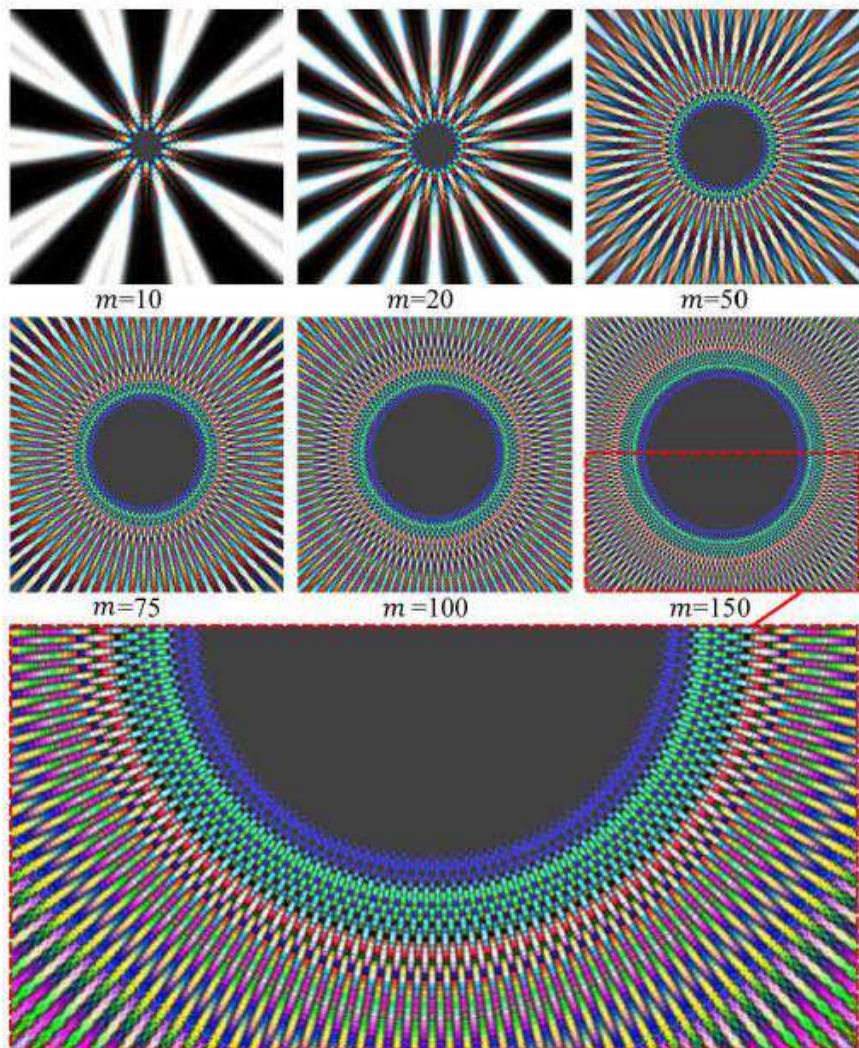


(b)

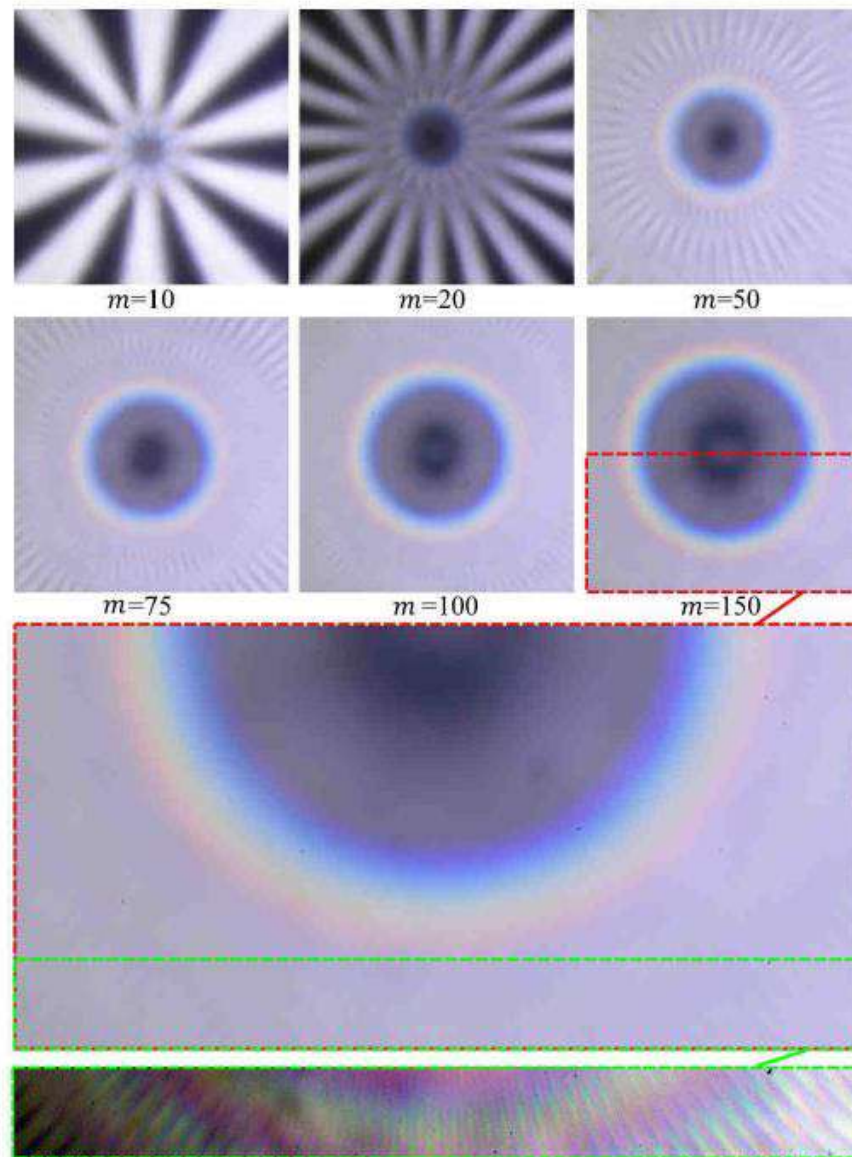


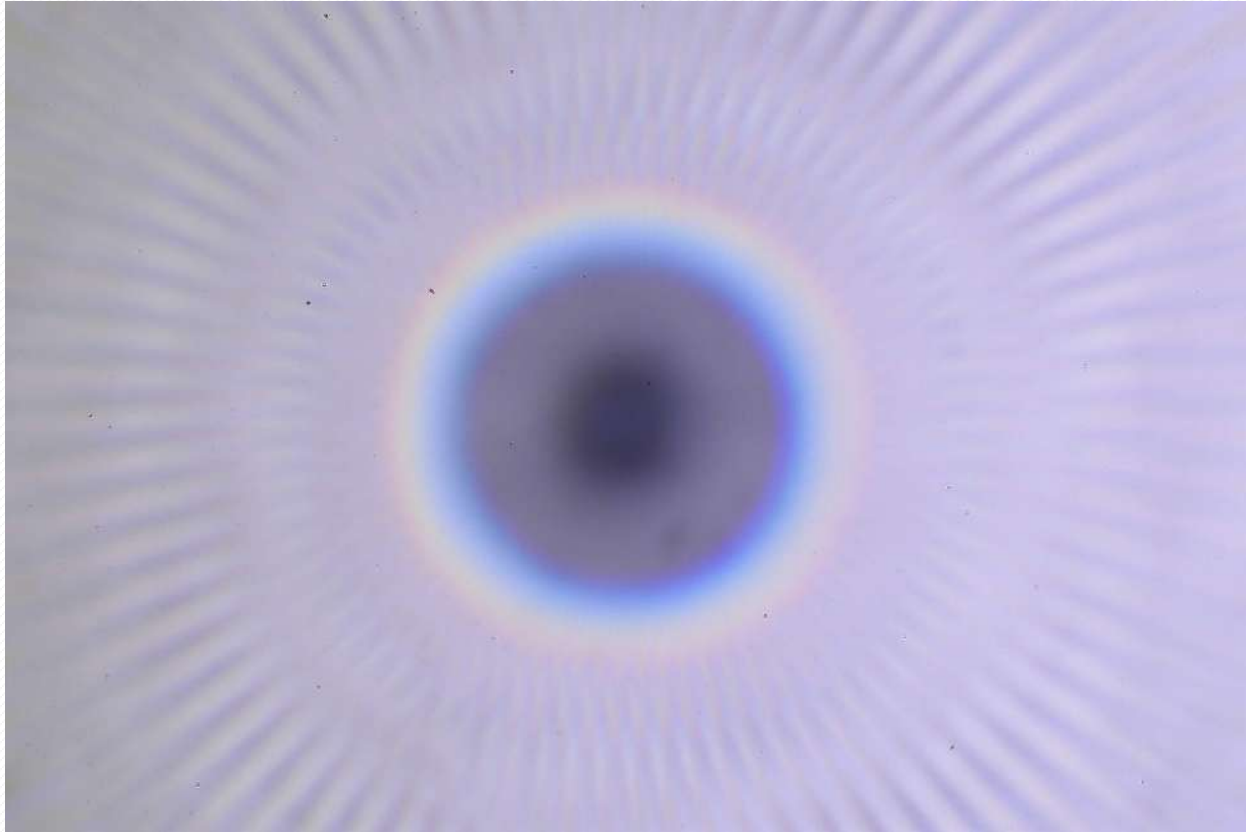
Colorful radial Talbot carpet at the transverse plane

(a)

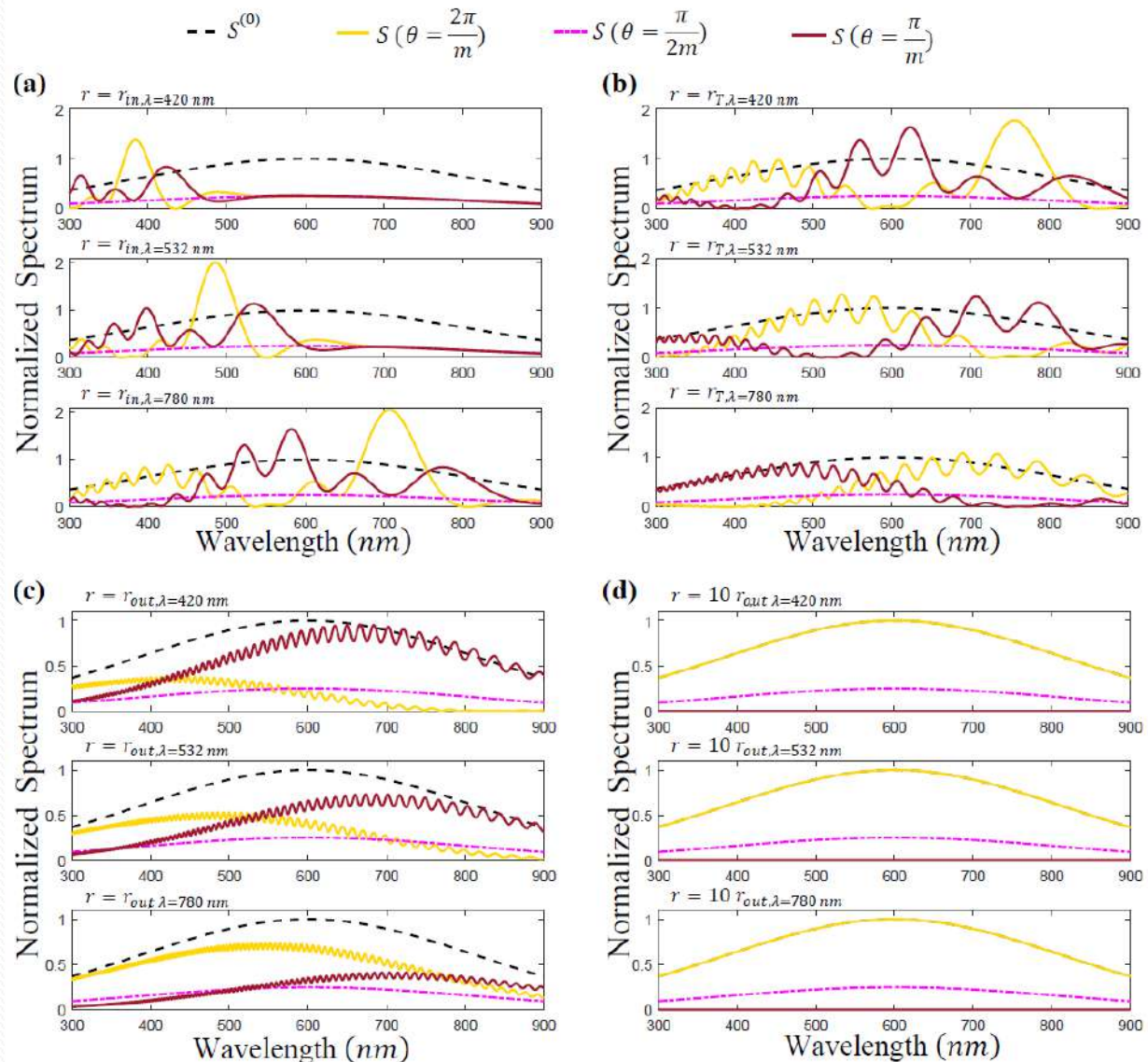


(b)





Diffraction-based rainbow and radial grating-based spectrometry



Rotatable annular multiple trapping with radial carpet beams

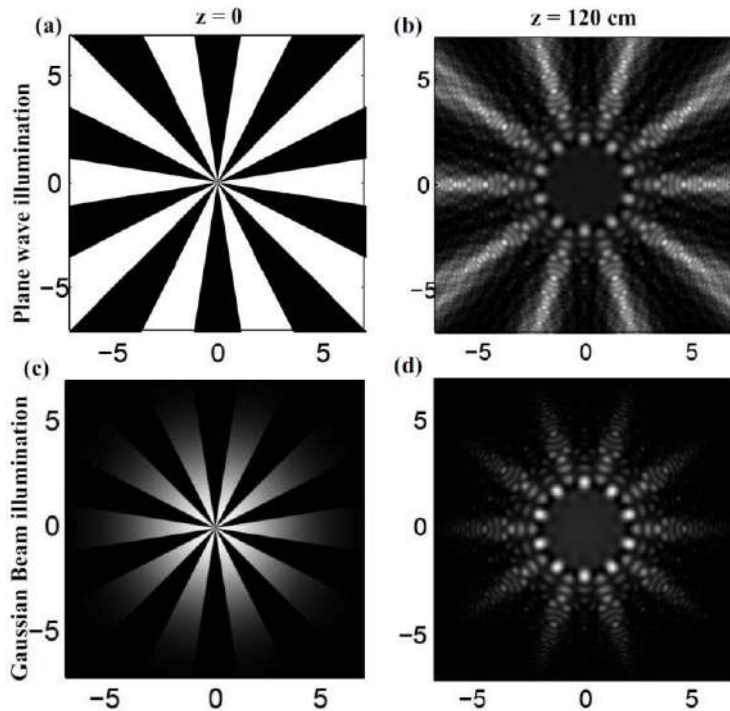


Fig. 1. (a) The intensity pattern immediately after an amplitude radial grating having binary profile with 10 spokes illuminated by a plane wave and (b) the calculated intensity of the resulted radial carpet beam at propagation distance 120 cm. (c) and (d) The same patterns when a Gaussian beam having a radius of 2 mm illuminates the same radial grating. All lengths are in millimeters.

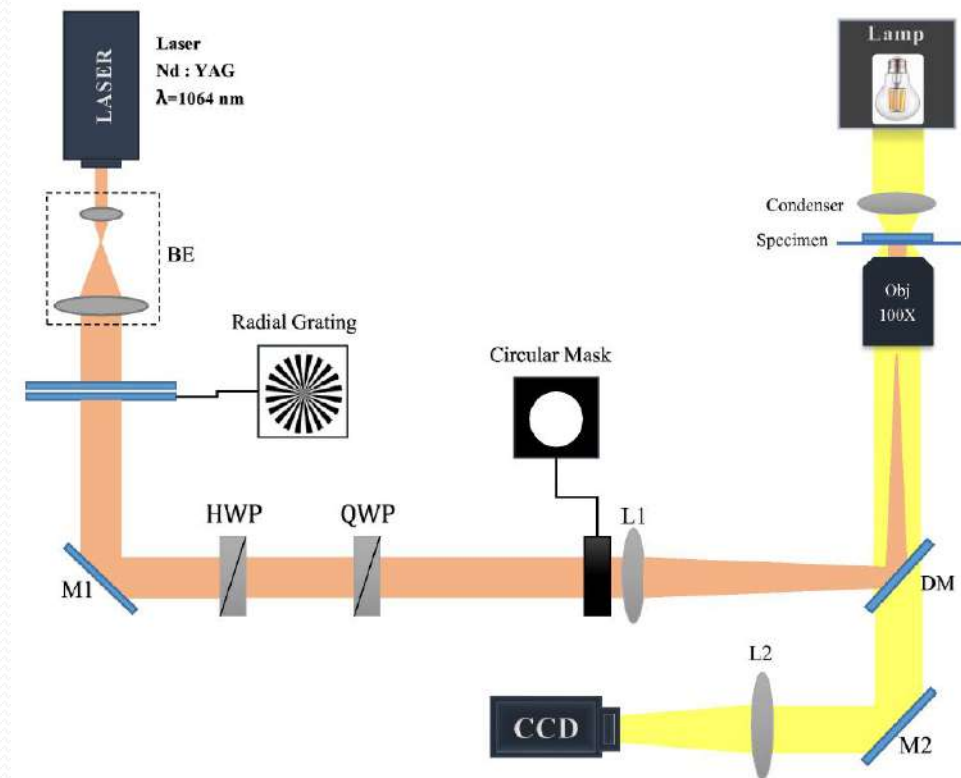


Fig. 2. Experimental setup; BE, M, HWP, QWP, L, DM, and QPD are the beam splitter, mirror, half and quarter wave plates, lens, dichroic mirror, and quadrant photo diode, respectively.

Rotatable annular multiple trapping with radial carpet beams

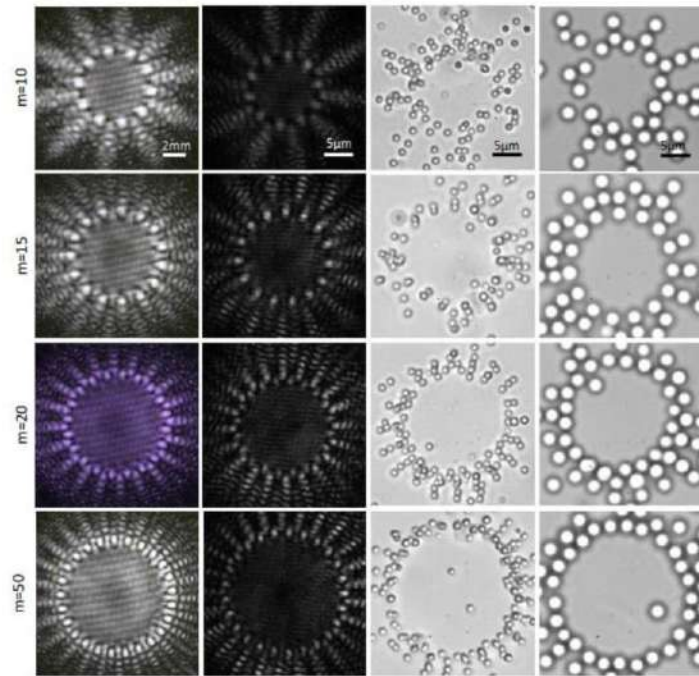


Fig. 3. Generated radial carpet patterns by the diffraction of a Gaussian beam from different radial amplitude gratings having binary profile and different spoke numbers at a distance 120 cm from the grating (first column) and inside the objective lens (second column). Different images of the trapped polystyrene particles with a diameter of $1.09 \mu\text{m}$ (third column) and $2.54 \mu\text{m}$ silica particles (forth column).

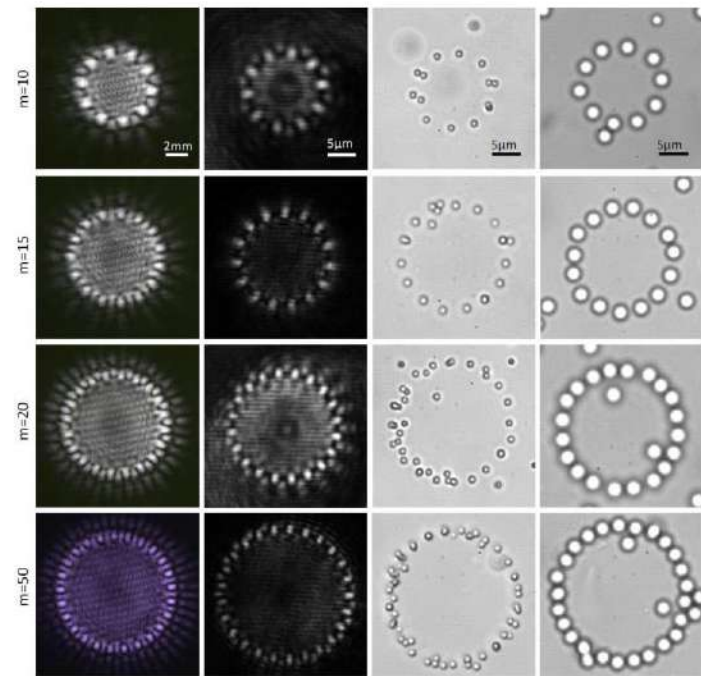


Fig. 4. The same patterns and trap images of Fig. 3 when a stop circular aperture was used before the L1 lens shown in Fig. 2 (see also Visualizations 1 and 2 that they show tapping and annular rotation of the trapped particles. Visualization 3 also shows axially rotation of the trapped vaterite particles in their own locations when the radial carpet light field is circularly polarized.).

Rotatable annular multiple trapping with radial carpet beams

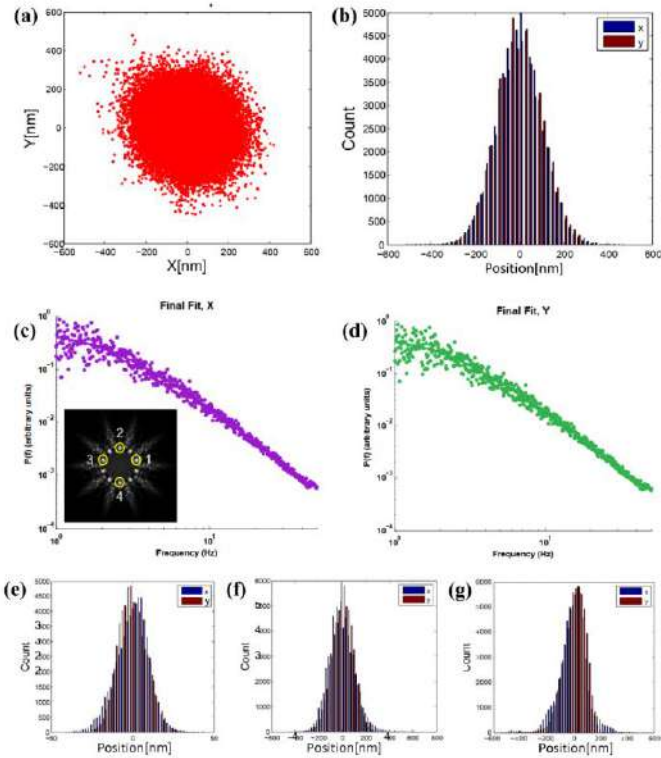


Fig. 6. (a) Distribution of the center of mass of a trapped 2.54 microns silica particle in two dimensions during a time interval 10 minutes. (b) The frequency histogram of the center of mass of the particle in two directions. (c) and (d) show the corresponding power spectra in x and y directions, respectively. The inset shows locations of four traps used for stiffness estimation. (e)-(g) Represent the frequency graphs of the particles at positions 2, 3, and 4, respectively.

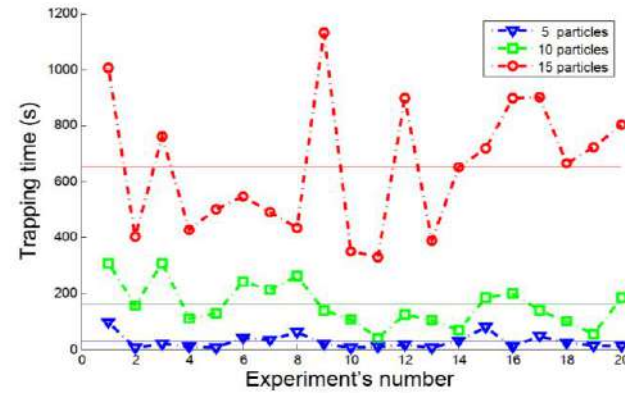


Fig. 5. The measured times to trap given number of particles.

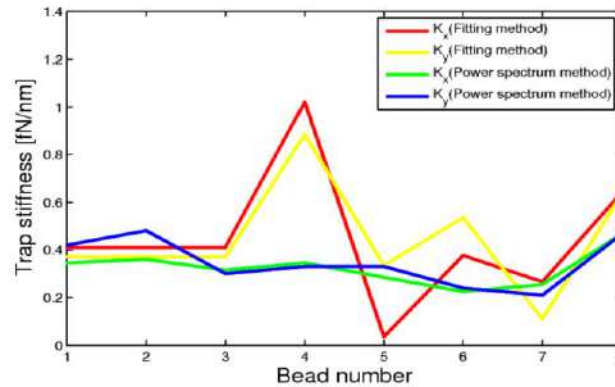
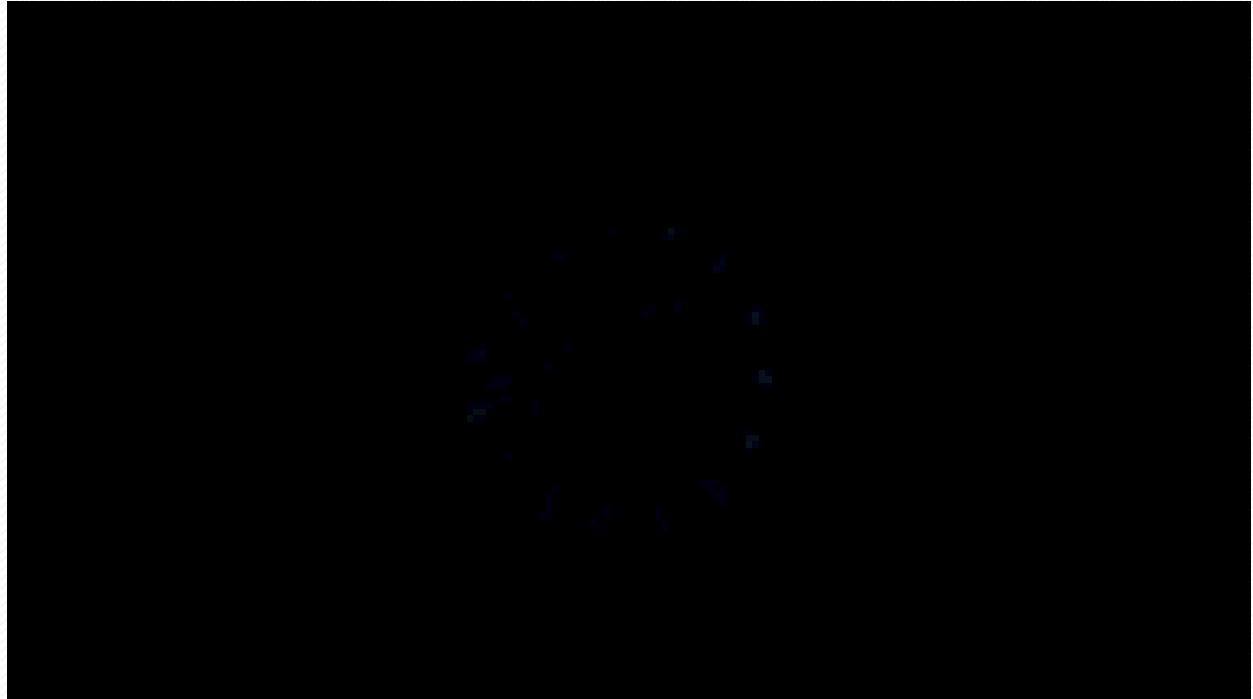


Fig. 7. Estimated trap stiffness for silica particles trapped at four different main intensity spots.

Rotatable annular multiple trapping with radial carpet beams

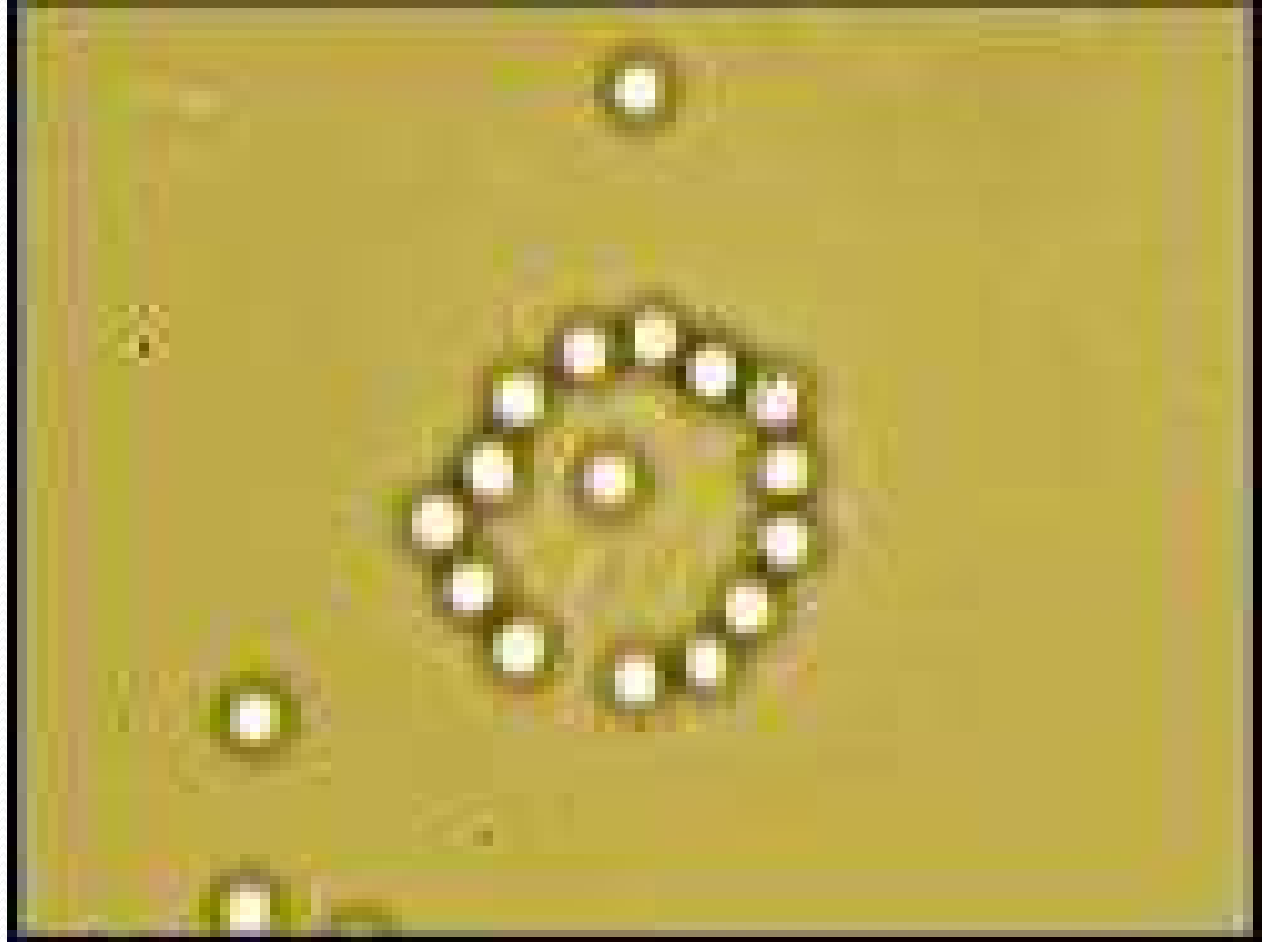
Visualizations 1 (2) shows annular rotation of the trapped 2.54 microns silica particles in water solution.

The total power of the trapping radial carpet light field was 86 mW at the L1 plane and it had 15 main intensity spots. Particles were trapped at the floor of the chamber. Annular rotation was implemented to the trapped particles by manually rotation of the grating. Movie is played 3 times faster than the recording time.



Visualizations 1 (2) shows annular rotation of the trapped 2.54 microns silica particles in water solution.

The total power of the trapping radial carpet light field was 86 mW at the L1 plane and it had 15 main intensity spots. Particles were trapped at the floor of the chamber. Annular rotation was implemented to the trapped particles by manually rotation of the grating. Movie is played 3 times faster than the recording time.



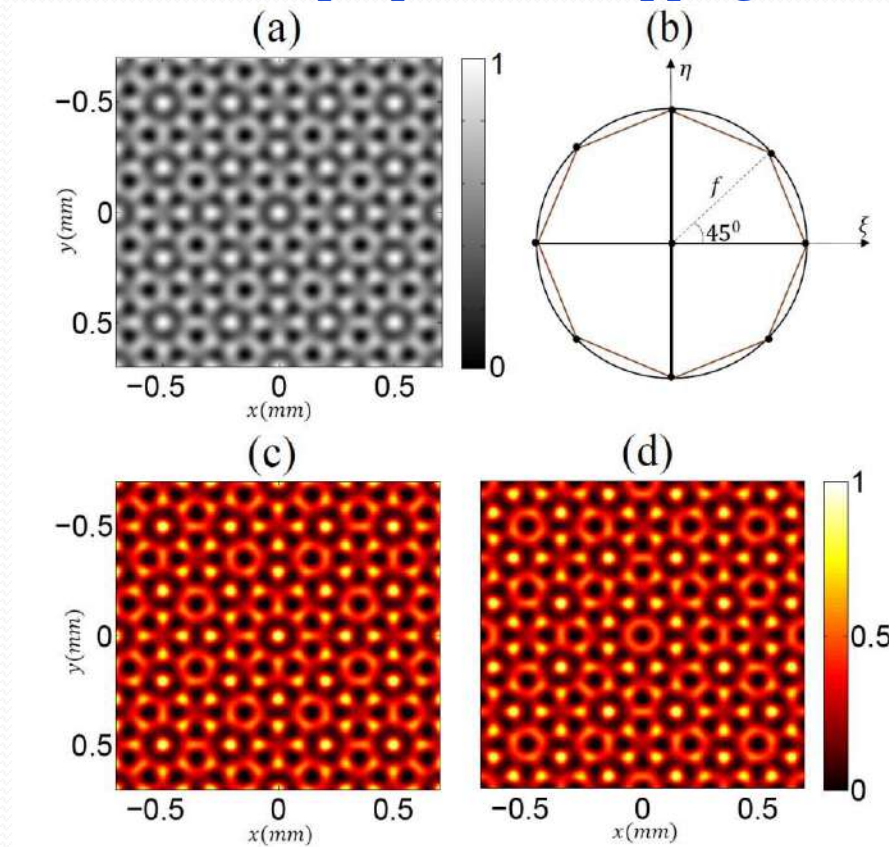
Axial rotation of multiple trapped particles with a circularly polarized radial carpet beam

Visualizations 3 shows axial rotation of, in laboratory made, up to 6 microns vaterite particles in water solution with circularly polarized radial carpet light field. The larger particle is rotating at a frequency of 0.4 Hz. Based on the shape and size of the trapped particles, the rotation frequency of the particles varies.

As can be seen, the cubic particle rotates at a higher frequency than other particles. The movie is played at a rate of 2.2 times real-time. The laser power after the grating was 140 mW and the beam itself had 10 main spots. Given that the lens of the object passes 30% of this power, the total beam power within the sample is 42 mW. Assuming the power is distributed over the main spots, the power of the beam per spot was approximately 4.2 mW.



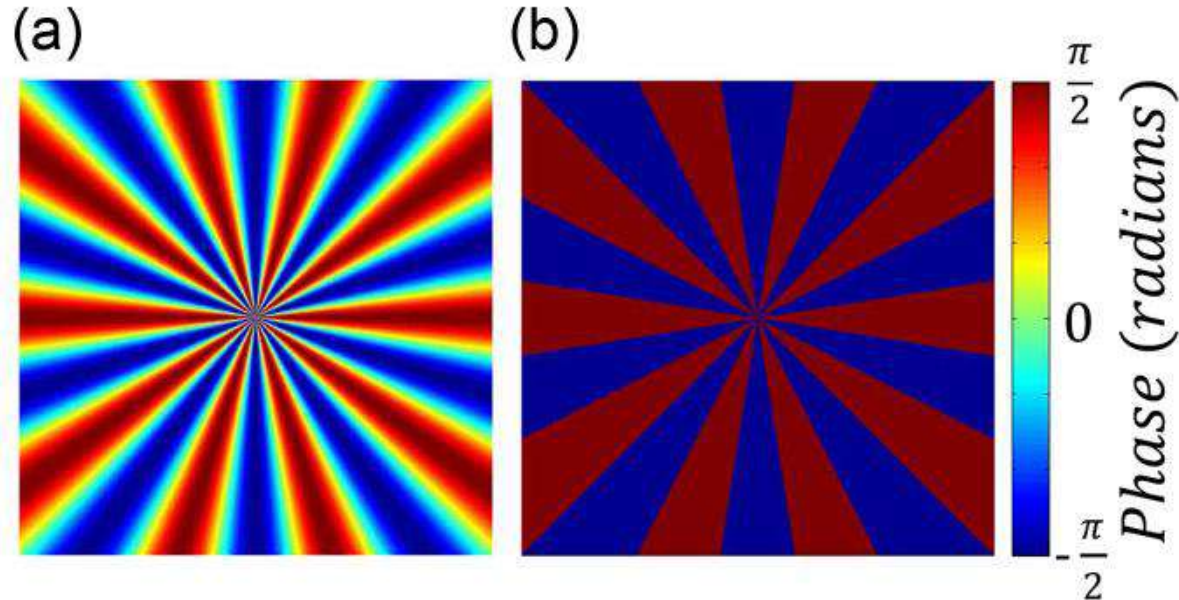
Talbot effect of 2D almost-periodic structures, 3D multiple particles trapping



A pure amplitude octagonal sinusoidal structure, (a) the transmission function, (b) its impulse-comb in the spectral domain, (c) the intensity patterns immediately after the structure and at the Talbot distances, and (d) the intensity patterns at the half-Talbot distances.

Diffraction of plane wave from radial phase gratings

Radial carpet beams: A class of nondiffracting, accelerating, and self-healing beams



Radial phase gratings with sinusoidal (a) and binary (b) transmission functions

$$t(\theta) = \sum_{n=-\infty}^{+\infty} t_n e^{in\theta} = t_0 + \sum_{n=1}^{+\infty} (t_n e^{in\theta} + t_{-n} e^{-in\theta}),$$

$$\psi(r, \theta; z) = e^{ikz} \left\{ t_0 + \mathcal{R} e^{i\mathcal{R}^2} \sum_{n=1}^{+\infty} \sqrt{\frac{\pi}{2}} (-i)^{\frac{n}{2}+1} (t_n e^{in\theta} + t_{-n} e^{-in\theta}) [J_{\frac{n+1}{2}}(\mathcal{R}^2) + i J_{\frac{n-1}{2}}(\mathcal{R}^2)] \right\},$$

$$\mathcal{R} = \sqrt{\frac{\pi}{2\lambda z}} r.$$

**Diffraction of plane wave
from radial phase grating
having sinusoidal profile**

$$t(\theta) = e^{i\gamma \cos(m\theta)} = \sum_{q=-\infty}^{+\infty} (i)^q J_q(\gamma) e^{iqm\theta},$$

$$\psi(r, \theta; z) = e^{ikz} \left\{ J_0(\gamma) + \mathcal{R}e^{i\mathcal{R}^2} \times \sum_{q=1}^{+\infty} \psi_q \left[J_{\frac{qm+1}{2}}(\mathcal{R}^2) \right. \right. \\ \left. \left. + i J_{\frac{qm-1}{2}}(\mathcal{R}^2) \right] \cos(qm\theta) \right\},$$

$$\psi_q = \sqrt{2\pi} (-i)^{\left(\frac{m}{2}-1\right)q+1} J_q(\gamma).$$

**Diffraction of plane wave
from radial phase grating
having binary profile**

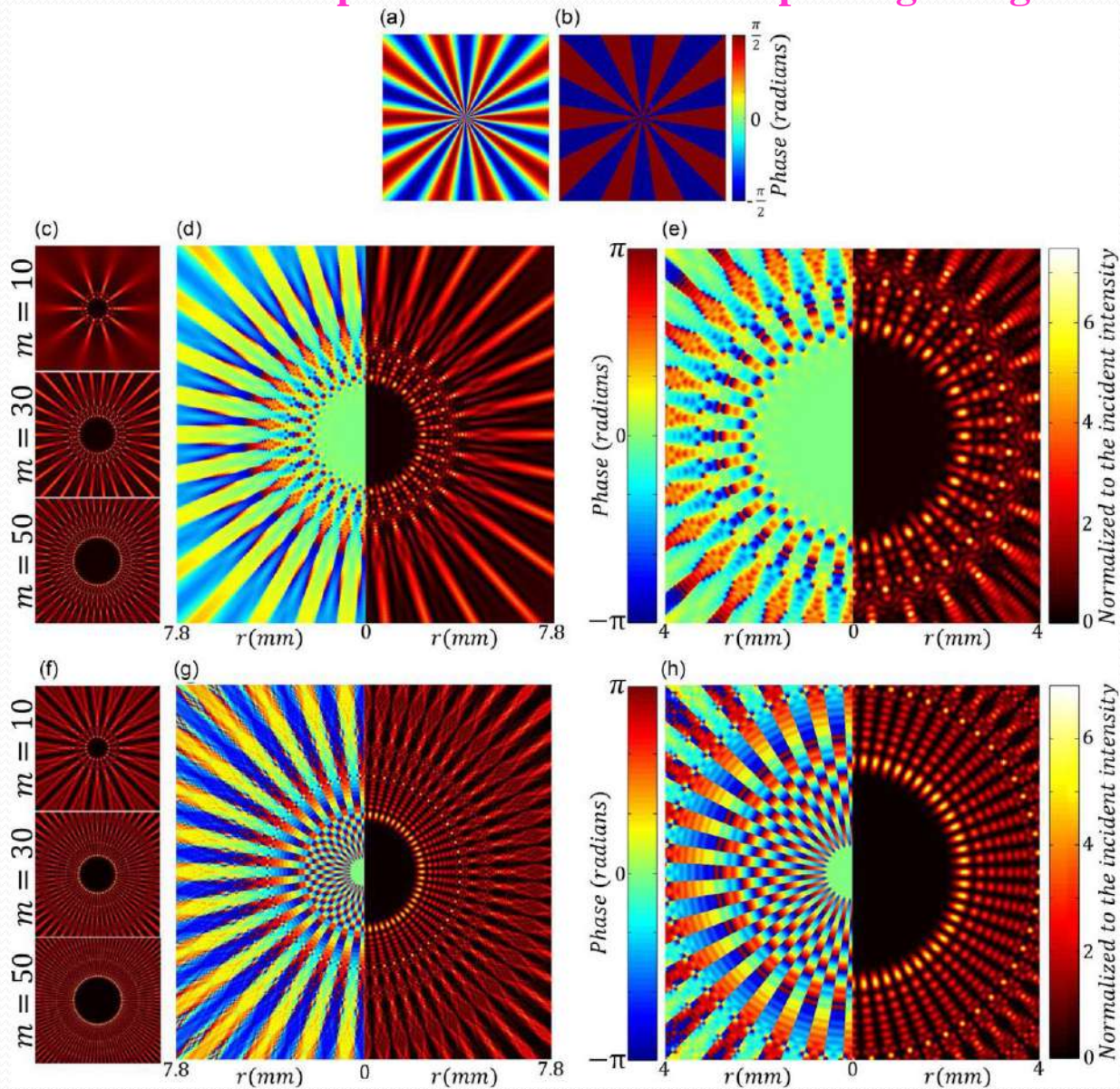
$$t(\theta) = e^{i\gamma \operatorname{sgn}[\cos(m\theta)]},$$

$$\psi(r, \theta; z) = e^{ikz} \left\{ \cos(\gamma) + \mathcal{R}e^{i\mathcal{R}^2} \sum_{\substack{l=1 \\ \text{odd}}}^{\infty} \psi_l \left[J_{\frac{lm+1}{2}}(\mathcal{R}^2) \right. \right. \\ \left. \left. + i J_{\frac{lm-1}{2}}(\mathcal{R}^2) \right] \cos(lm\theta) \right\},$$

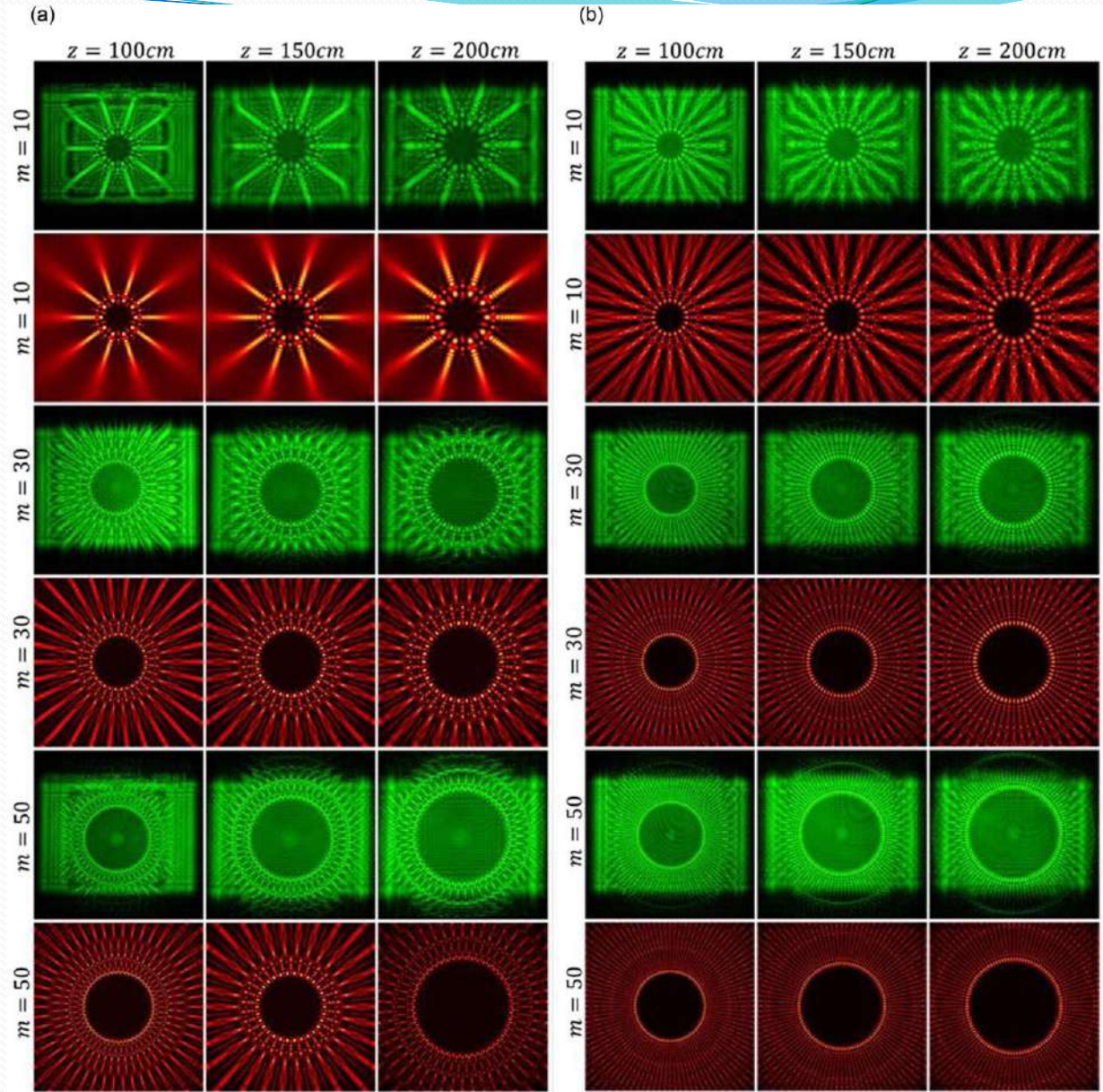
$$\psi_l = \frac{2}{l} \sqrt{\frac{2}{\pi}} \sin(\gamma) (-i)^{\left(\frac{m}{2}-1\right)l+1}.$$

Radial carpet beams: A class of nondiffracting, accelerating, and self-healing beams

Diffraction of plane wave from radial phase gratings

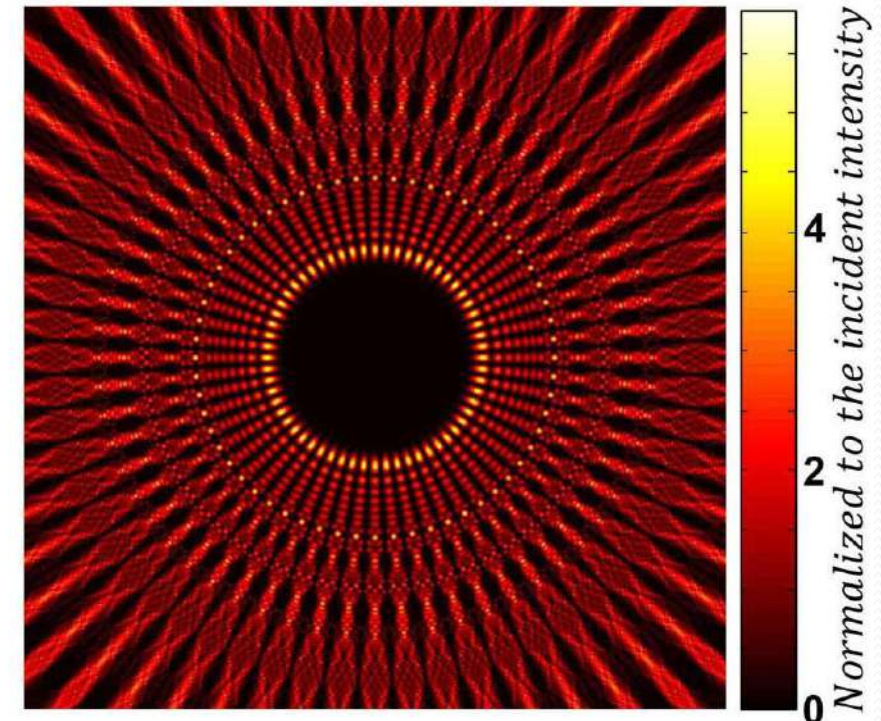
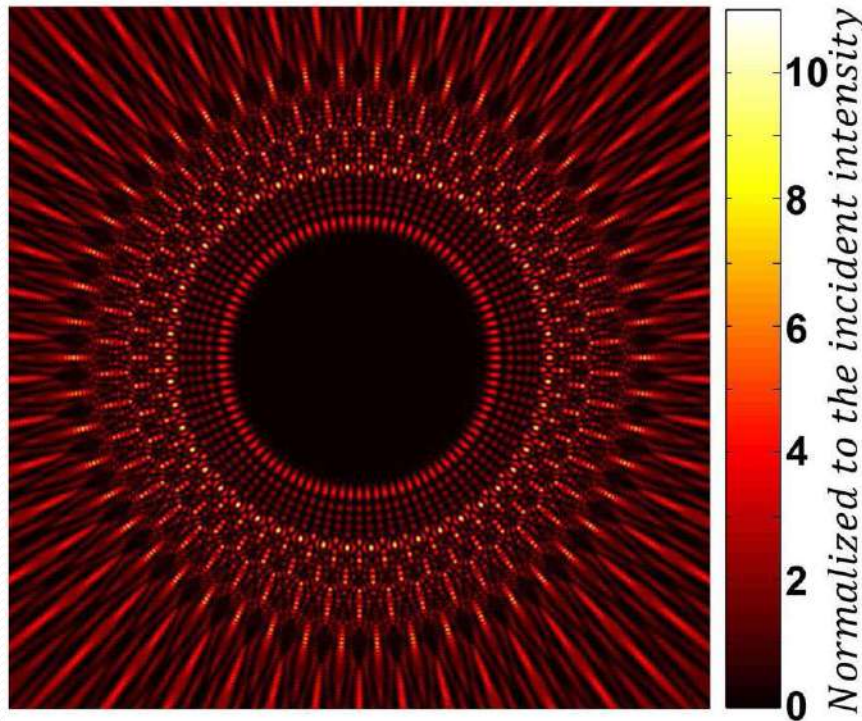


Radial carpet beams: A class of nondiffracting, accelerating, and self-healing beams
 Diffraction of plane wave from radial phase gratings



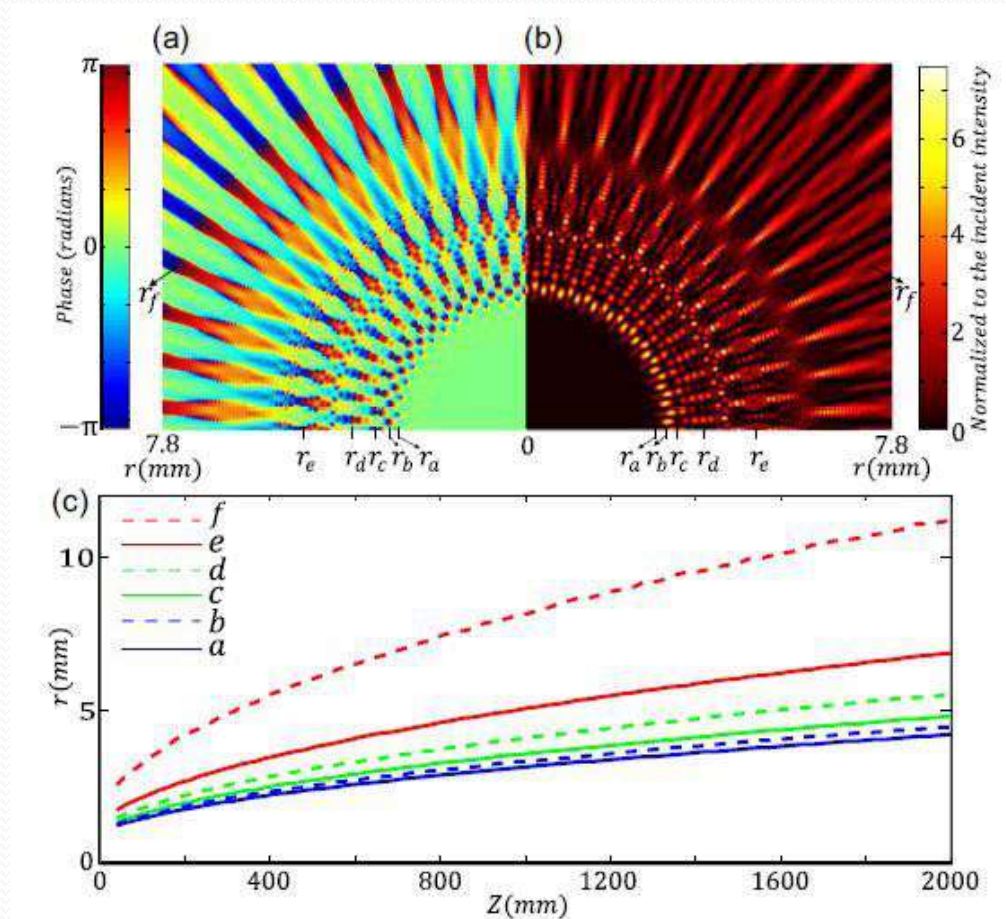
Calculated intensity profiles for two carpet beams having zero value of intensity in the central area.

- (a) Calculated intensity of the diffraction pattern from a sinusoidal phase grating with $m = 50$ and $\gamma = 2.4048$ rad at $z = 100$ cm. Here, the intensity of the central area is zero. The real size of the pattern is $15.6 \text{ mm} \times 15.6 \text{ mm}$. (b) The same pattern for a binary phase grating with $\gamma = \pi/2$ and $m = 30$.



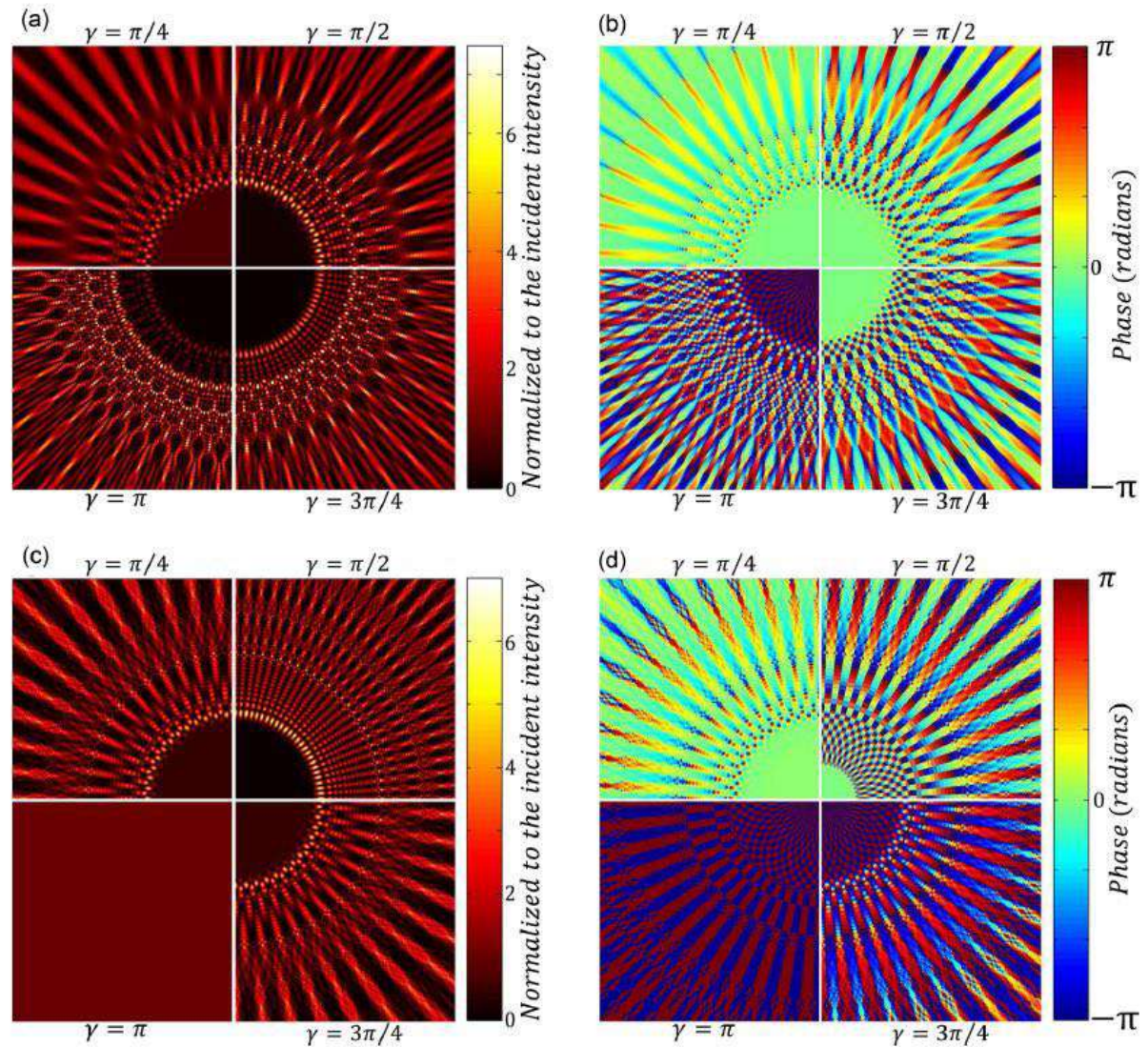
Self-accelerating property of radial carpet beams.

(a, b) Calculated phase and intensity profiles for the diffracted complex light field passing through a sinusoidal phase grating with $m = 50$ and $\gamma = \pi/2$ at $z = 100$ cm. (c) Calculated propagation paths for six given intensity rings. Radii of the selected rings at $z = 100$ cm are shown over the first row's profiles.



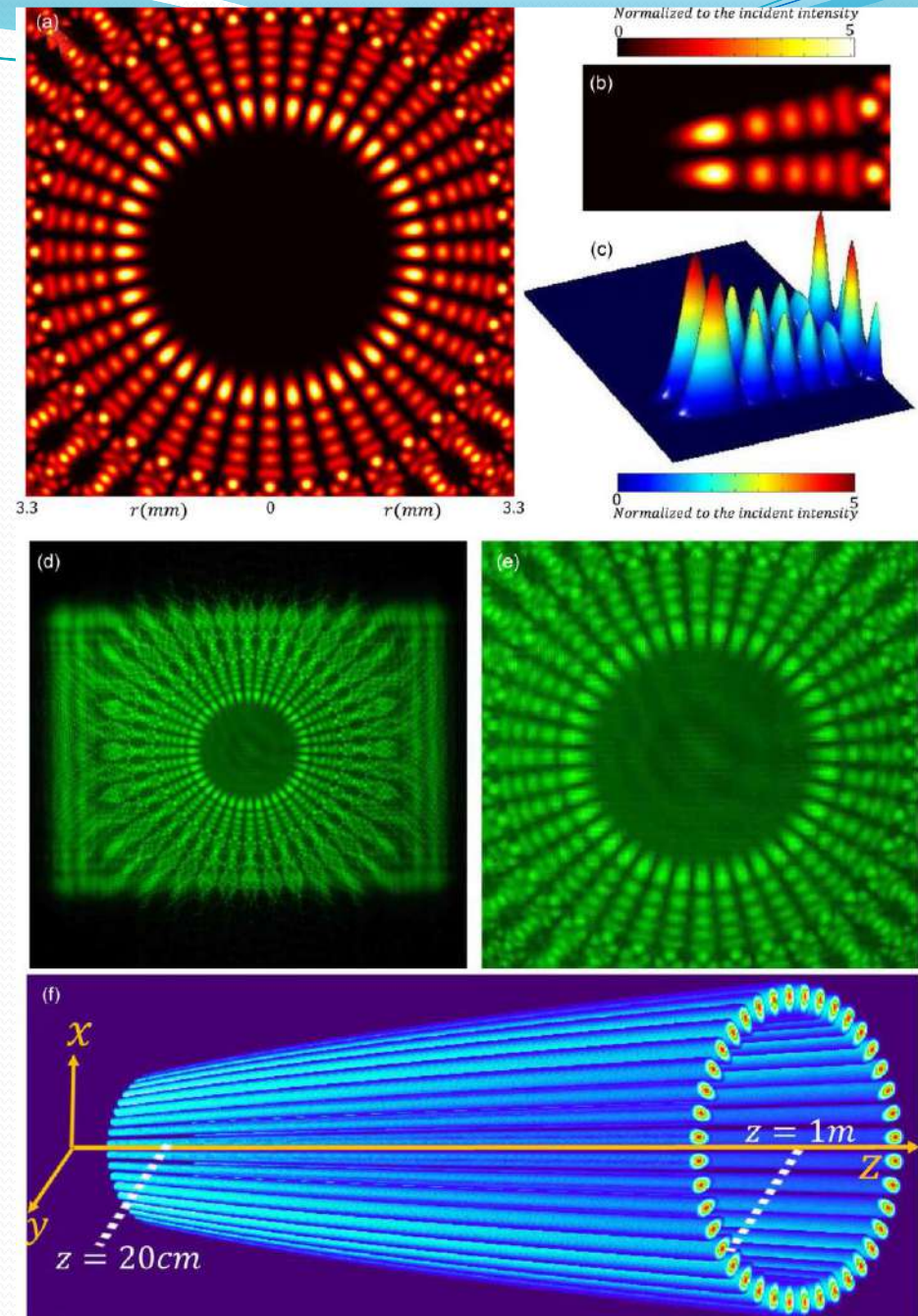
Architecture of radial carpet beams by tuning the amplitude of phase variation of the grating.

(a, b) Calculated intensity and phase distributions of the diffracted field for a sinusoidal phase grating with $m = 50$ and different value of γ at $z = 100$ cm, respectively. (c, d) Show corresponding patterns for a binary phase grating, see also Movies 3a–3d [23].

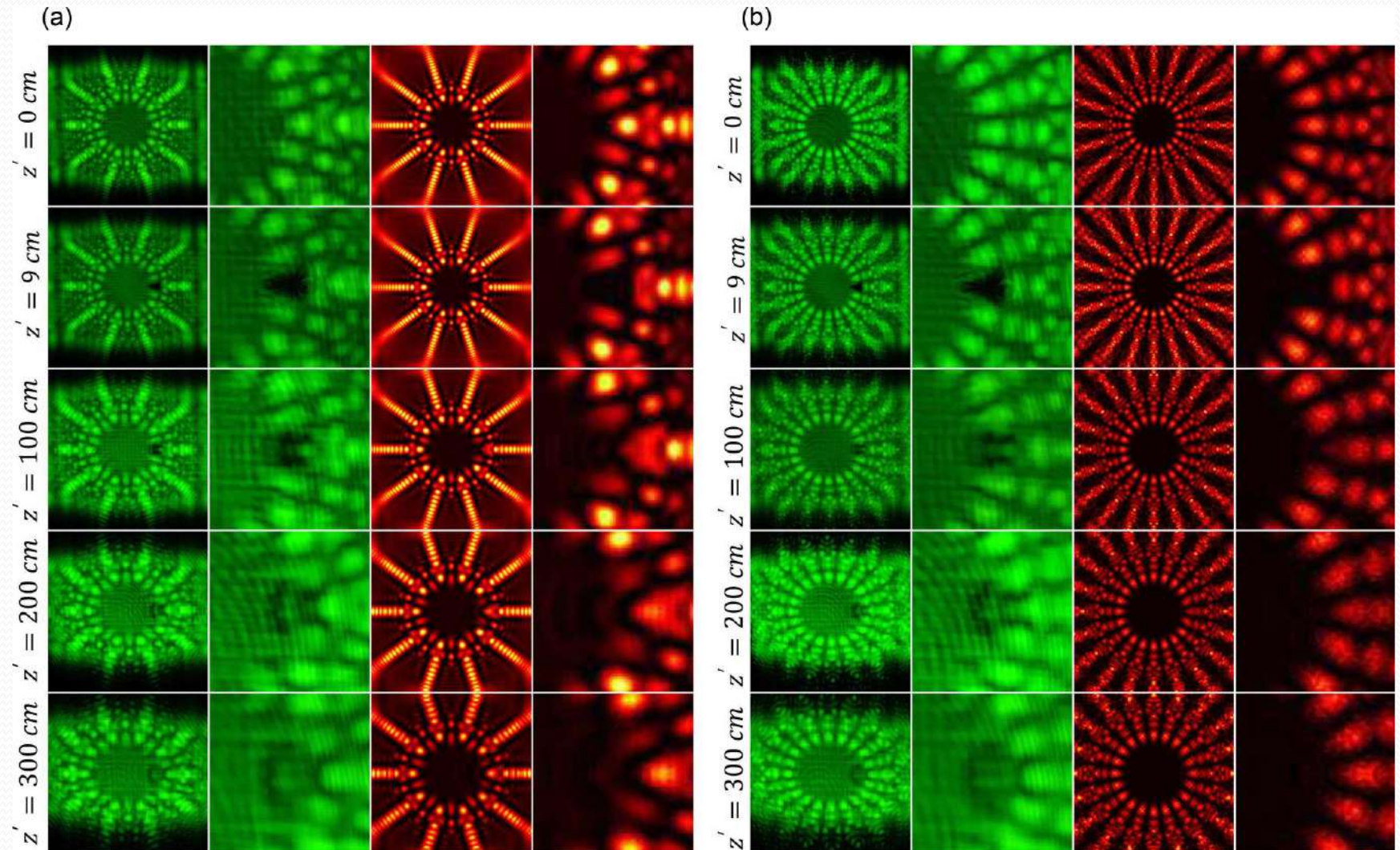


Radial carpet beams as a 2D optical lattice with a polar symmetry.

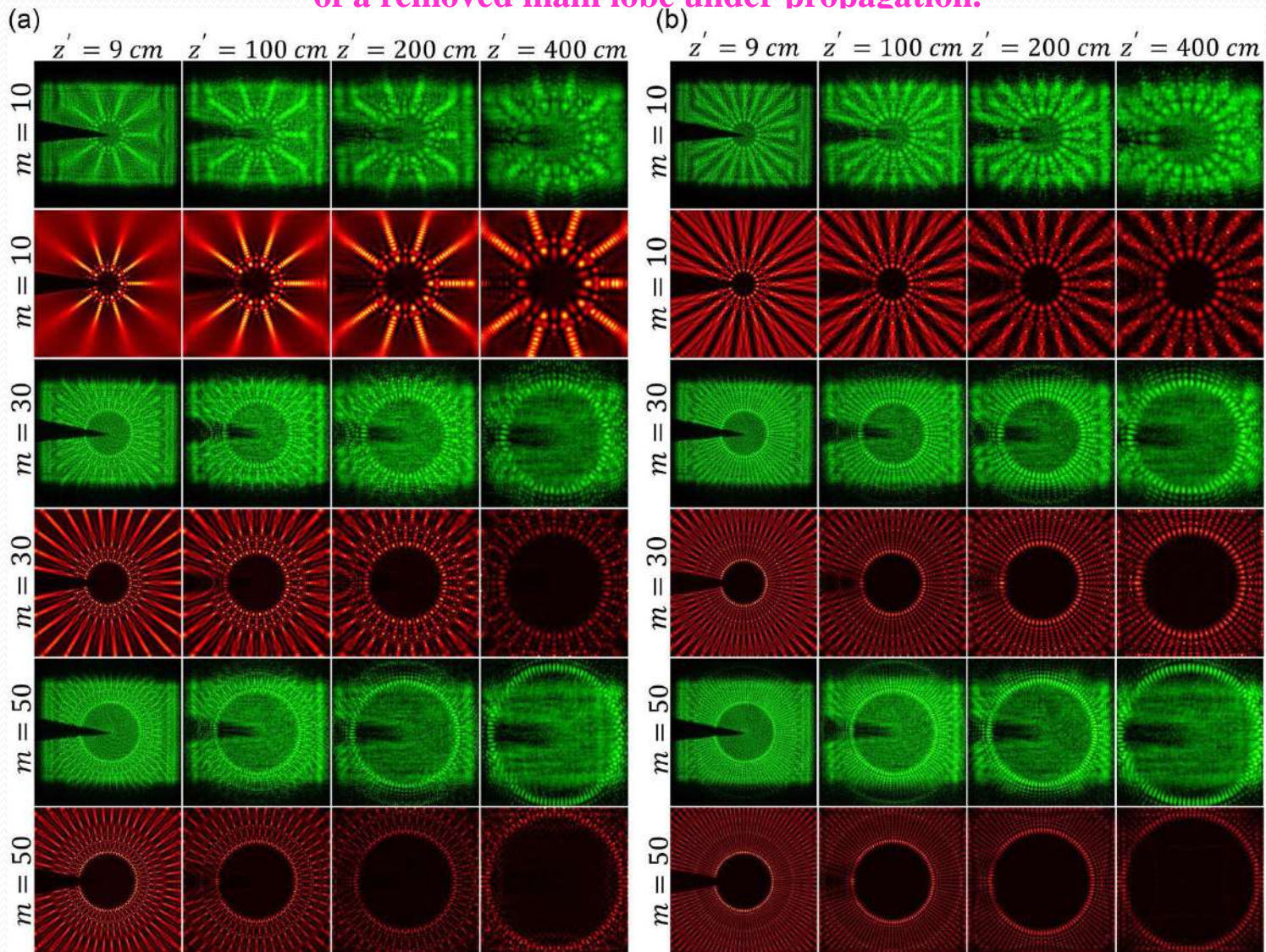
2D optical lattice formation by laser beam self-channeling after propagating a plane wave through a radial phase grating with a binary amplitude. (a) Calculated diffraction pattern for a radial phase grating having a binary profile with $m = 20$ spokes at a distance of 100 cm from the grating with a value of $\gamma = \pi/2$. (b, c) Two different illustrations of the intensity profile of a sector of the introduced pattern in (a). (d) An experimentally recorded 2D optical lattice produced by a binary phase grating with the same parameters and at the same distance from the grating of (a). (e) An inset of (d). (f) 3D illustration of the main lobes of (a) under propagation (see also Movie 4 in the Supplemental Material [23]).



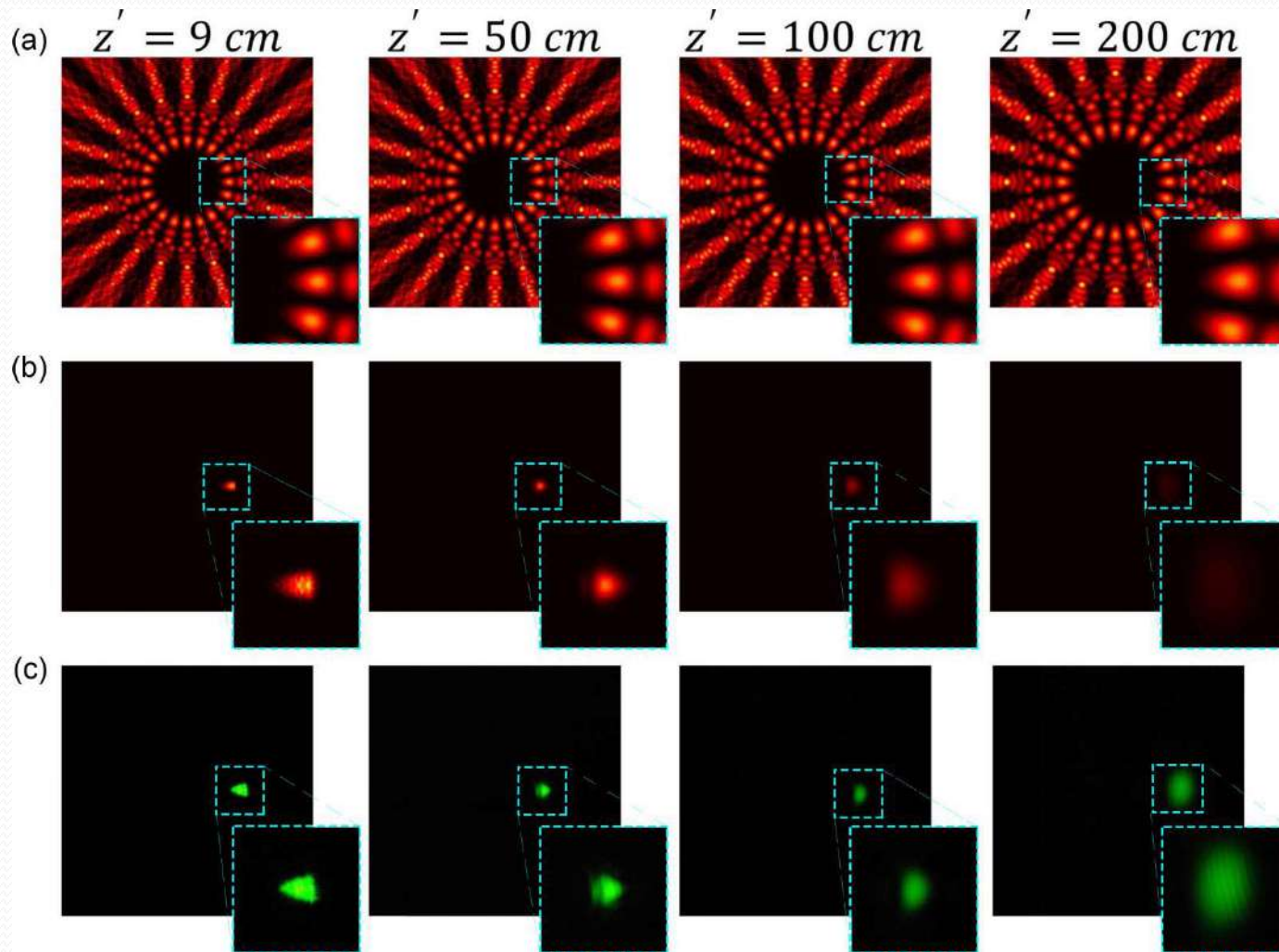
Self-healing of carpet beams, self-reconstruction of a removed main lobe under propagation.



Self-healing of carpet beams, self-reconstruction of a removed main lobe under propagation.



Effect of an exaggerated cancellation on the self-healing and nondiffracting properties of the carpet beams



Combined half-integer Bessel-like beams: A set of solutions of the wave equation

Helmholtz equation

$$\nabla^2 U + k^2 U = 0,$$

A paraxial wave traveling along the z direction

$$U(x, y, z) = A(x, y, z) \exp(ikz),$$

Paraxial Helmholtz equation

$$\nabla_T^2 A + 2ik \frac{\partial A}{\partial z} = 0,$$

$$\frac{1}{r} \frac{\partial}{\partial r} \left(r \frac{\partial A}{\partial r} \right) + \frac{1}{r^2} \frac{\partial^2 A}{\partial \theta^2} + 2ik \frac{\partial A}{\partial z} = 0,$$

$$A(r, \theta, z) = g(\rho) \exp(in\theta), \quad \rho = \rho(r, z) = \frac{kr^2}{4z}$$

Partial differential equation (PDE)

$$r \frac{\partial}{\partial r} \left(r \frac{\partial g}{\partial r} \right) + 2ikr^2 \frac{\partial g}{\partial z} - n^2 g = 0.$$

$$\frac{\partial \rho}{\partial r} = \frac{k}{2z} r = \frac{2\rho}{r}$$

$$\frac{\partial \rho}{\partial z} = -\frac{kr^2}{4z^2} = -\frac{\rho}{z}$$

$$r \frac{\partial \rho}{\partial r} = 2\rho$$

Ordinary differential equation (ODE)

$$\frac{1}{\rho} \frac{d}{d\rho} \left(\rho \frac{dg}{d\rho} \right) - 2i \frac{dg}{d\rho} - \frac{(n/2)^2}{\rho^2} g = 0,$$

Combined half-integer Bessel-like beams: A set of solutions of the wave equation

Ordinary differential equation (ODE)

$$\frac{1}{\rho} \frac{d}{d\rho} \left(\rho \frac{dg}{d\rho} \right) - 2i \frac{dg}{d\rho} - \frac{(n/2)^2}{\rho^2} g = 0,$$



$$A(\rho, \theta) = \sqrt{\rho} e^{i\rho} \sum_{n=-\infty}^{\infty} (a_n e^{in\theta} + b_n e^{-in\theta}) \quad A(r, \theta, z) = g(\rho) \exp(in\theta),$$

$$\times \left[J_{\frac{n+1}{2}}(\rho) + i J_{\frac{n-1}{2}}(\rho) \right], \quad U(x, y, z) = A(x, y, z) \exp(ikz),$$

Combined half-integer Bessel-like beams



$$U(r, \theta, z) = e^{ikz} \left\{ t_0 + \sqrt{\rho} e^{i\rho} \sum_{n=1}^{+\infty} (a_n e^{in\theta} + b_n e^{-in\theta}) \right.$$

$$\left. \times \left[J_{\frac{n+1}{2}}(\rho) + i J_{\frac{n-1}{2}}(\rho) \right] \right\},$$

Radial Carpet beams of binary grating

Radial Carpet beams of sinusoidal grating

$$g(r, \theta) = \frac{e^{ikz}}{2} \times \left\{ 1 + \mathcal{R} e^{i\mathcal{R}^2} \sqrt{\frac{\pi}{2}} (-i)^{\frac{m}{2}+1} \right.$$

$$\left. \times \left[J_{\frac{m+1}{2}}(\mathcal{R}^2) + i J_{\frac{m-1}{2}}(\mathcal{R}^2) \right] \cos(m\theta) \right\}.$$

$$g(r, \theta) = \frac{e^{ikz}}{2} \times \left\{ 1 + \mathcal{R} e^{i\mathcal{R}^2} \sum_{l=1}^{\infty} g_l \right.$$

$$\left. \times \left[J_{\frac{ml+1}{2}}(\mathcal{R}^2) + i J_{\frac{ml-1}{2}}(\mathcal{R}^2) \right] \cos(ml\theta) \right\},$$

Comparison of the theoretical predictions of the Fresnel integral and solution of the wave equation

Combined half-integer Bessel-like beams

$$U(r, \theta, z) = e^{ikz} \left\{ t_0 + \sqrt{\rho} e^{i\rho} \sum_{n=1}^{+\infty} (a_n e^{in\theta} + b_n e^{-in\theta}) \times \left[J_{\frac{n+1}{2}}(\rho) + i J_{\frac{n-1}{2}}(\rho) \right] \right\},$$

Radial Carpet beams of amplitude sinusoidal grating

$$g(r, \theta) = \frac{e^{ikz}}{2} \times \left\{ 1 + \mathcal{R} e^{i\mathcal{R}^2} \sqrt{\frac{\pi}{2}} (-i)^{\frac{m}{2}+1} \times \left[J_{\frac{m+1}{2}}(\mathcal{R}^2) + i J_{\frac{m-1}{2}}(\mathcal{R}^2) \right] \cos(m\theta) \right\}.$$

Radial Carpet beams of amplitude binary grating

$$g(r, \theta) = \frac{e^{ikz}}{2} \times \left\{ 1 + \mathcal{R} e^{i\mathcal{R}^2} \sum_{l=1}^{\infty} g_l \times \left[J_{\frac{m+1}{2}}(\mathcal{R}^2) + i J_{\frac{m-1}{2}}(\mathcal{R}^2) \right] \cos(ml\theta) \right\},$$

Radial Carpet beams of sinusoidal phase grating

$$\psi(r, \theta; z) = e^{ikz} \left\{ J_0(\gamma) + \mathcal{R} e^{i\mathcal{R}^2} \times \sum_{q=1}^{+\infty} \psi_q \left[J_{\frac{qm+1}{2}}(\mathcal{R}^2) + i J_{\frac{qm-1}{2}}(\mathcal{R}^2) \right] \cos(qm\theta) \right\},$$

Radial Carpet beams of binary phase grating

$$\psi(r, \theta; z) = e^{ikz} \left\{ \cos(\gamma) + \mathcal{R} e^{i\mathcal{R}^2} \sum_{\substack{l=1 \\ \text{odd}}}^{\infty} \psi_l \left[J_{\frac{lm+1}{2}}(\mathcal{R}^2) + i J_{\frac{lm-1}{2}}(\mathcal{R}^2) \right] \cos(lm\theta) \right\},$$

Passible application

Diffraction from designed radial structures: A way for generating desired radial carpet beams

Combined half-integer Bessel-like beams

$$U(r, \theta, z) = e^{ikz} \left\{ t_0 + \sqrt{\rho} e^{i\rho} \sum_{n=1}^{+\infty} (a_n e^{in\theta} + b_n e^{-in\theta}) \times \left[J_{\frac{n+1}{2}}(\rho) + i J_{\frac{n-1}{2}}(\rho) \right] \right\},$$

Boundary condition at $z=0$ plane:

$$U(x, y, z = 0)$$

$$\rho \propto \frac{1}{z}, \text{ for } z \rightarrow 0$$

ρ goes to infinity

$$J_\nu(\rho) \rightarrow \sqrt{\frac{2}{\pi\rho}} \cos\left(\rho - \frac{\nu\pi}{2} - \frac{\pi}{4}\right)$$

$$\left[J_{\frac{n+1}{2}}(\rho) + i J_{\frac{n-1}{2}}(\rho) \right] \rightarrow i^{\frac{n}{2}+1} \sqrt{\frac{2}{\pi\rho}} \exp(-i\rho)$$

$$U(r, \theta, z = 0) = t(\theta) = t_0 + \sum_{n=1}^{+\infty} (t_n e^{in\theta} + t_{-n} e^{-in\theta}),$$

$$\text{where } t_n = i^{\frac{n}{2}+1} \sqrt{\frac{2}{\pi}} a_n \text{ and } t_{-n} = i^{\frac{n}{2}+1} \sqrt{\frac{2}{\pi}} b_n.$$

The main feature of this result is that it has no radial dependency and can be considered as the transmitted amplitude of a plane wave immediately after a radial structure.

Using Fresnel-Kirchhoff integral, such light beam under propagation

$$U(r, \theta, z) = e^{ikz} \left\{ t_0 + \sqrt{\rho} e^{i\rho} \sum_{n=1}^{+\infty} \sqrt{\frac{\pi}{2}} (-i)^{\frac{n}{2}+1} \times (t_n e^{in\theta} + t_{-n} e^{-in\theta}) \left[J_{\frac{n+1}{2}}(\rho) + i J_{\frac{n-1}{2}}(\rho) \right] \right\}$$

$$t_n = i^{\frac{n}{2}+1} \sqrt{\frac{2}{\pi}} a_n \text{ and } t_{-n} = i^{\frac{n}{2}+1} \sqrt{\frac{2}{\pi}} b_n$$

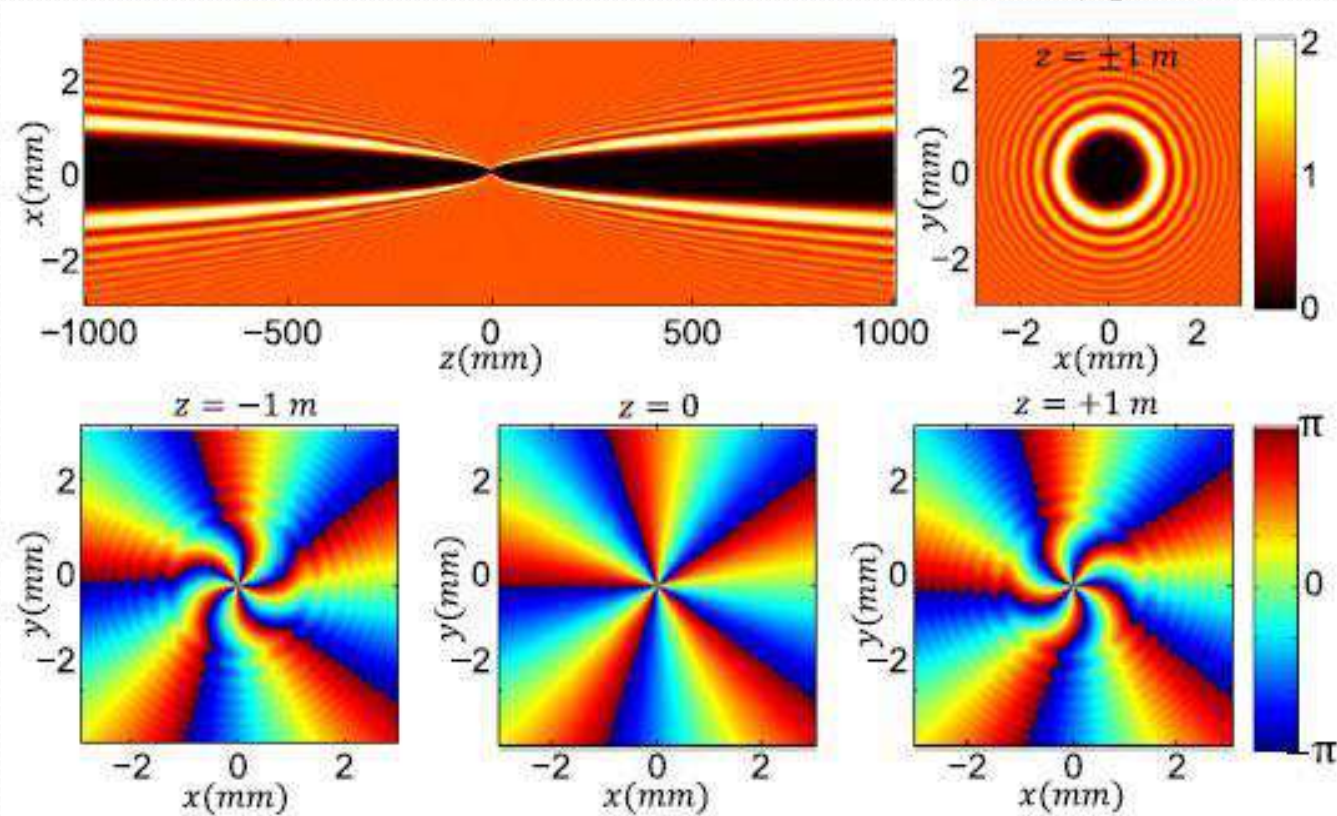
Diffraction from designed radial structures

$$U(r, \theta, z = 0) = t(\theta) = t_0 + \sum_{n=1}^{+\infty} (t_n e^{in\theta} + t_{-n} e^{-in\theta}),$$

$$t(\theta) = \exp(im\theta), \quad t_m = 1.$$

It describes a spiral phase plate (SPP).

$$U = u_m e^{i(kz + \rho + m\theta)} \sqrt{\rho} \left[J_{\frac{m+1}{2}}(\rho) + i J_{\frac{m-1}{2}}(\rho) \right], \quad u_m = \sqrt{\frac{\pi}{2}} (-i)^{\frac{m}{2} + 1}.$$



Diffraction from designed radial structures: Petalike beams

$$t(\theta) = \cos(m\theta) = \frac{1}{2}(e^{im\theta} + e^{-im\theta})$$

It does not indicate a pure amplitude structure.

$$t(\theta) = |\cos(m\theta)|e^{i\delta(\theta)}$$

It does not indicate a pure amplitude structure.

The phase $\delta(\theta)$ is a binary periodic function alternating between 0 and π with a period of $2\pi/m$, and $|\cos(m\theta)|$ being the absolute value of the transmittance having a period of π/m .

$$t_m = t_{-m} = \frac{1}{2}$$

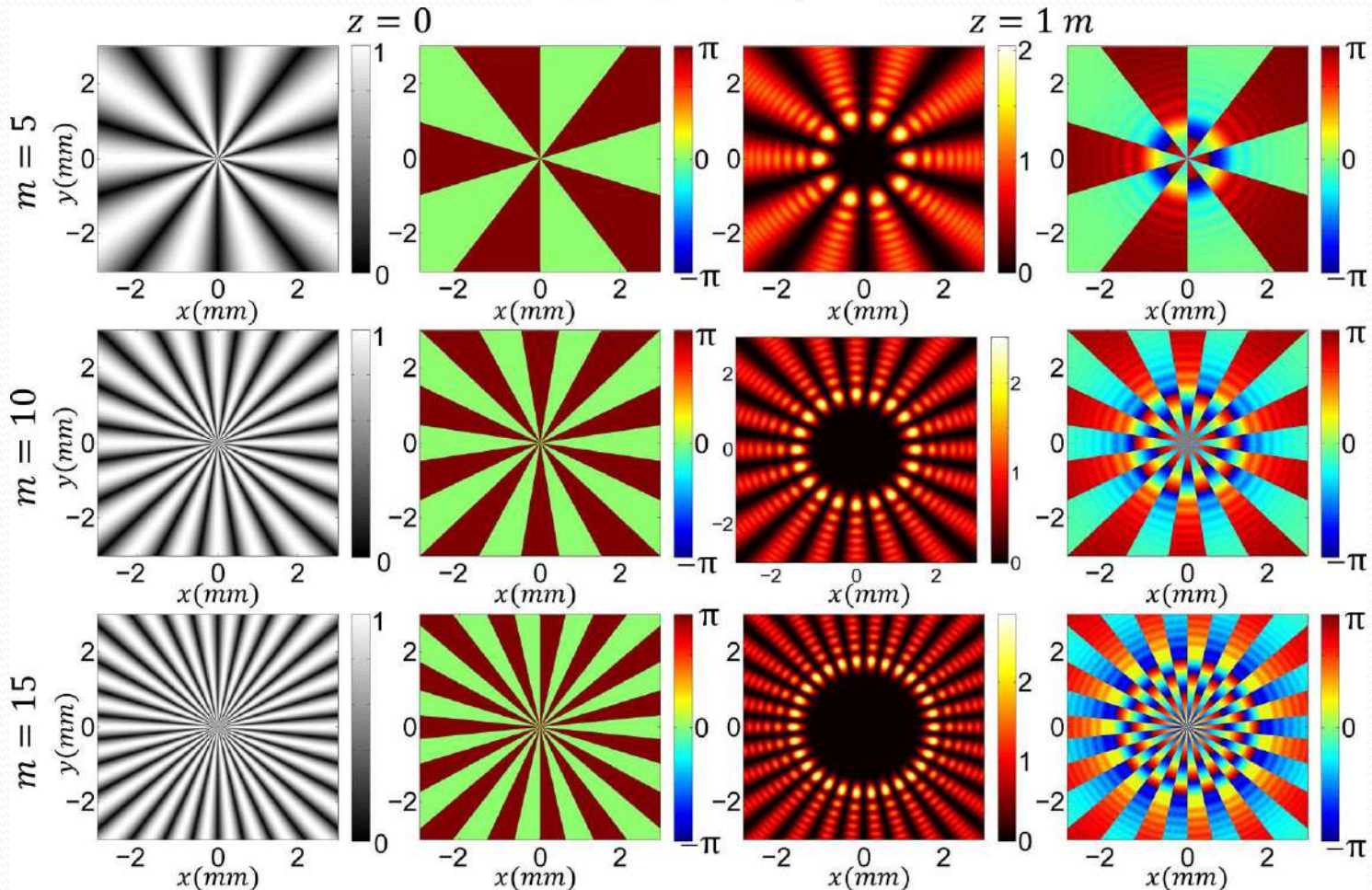
$$U(r, \theta, z) = u_m e^{i(kz + \rho)} \sqrt{\rho} [J_{\frac{m+1}{2}}(\rho) + i J_{\frac{m-1}{2}}(\rho)] \cos(m\theta),$$

$$u_m = \sqrt{\frac{\pi}{2}} (-i)^{\frac{m}{2} + 1}.$$

Diffraction from designed radial structures: Petalike beams

$$t(\theta) = \cos(m\theta) = \frac{1}{2}(e^{im\theta} + e^{-im\theta})$$

$$t(\theta) = |\cos(m\theta)|e^{i\delta(\theta)}$$



$$U(r, \theta, z) = u_m e^{i(kz + \rho)} \sqrt{\rho} [J_{\frac{m+1}{2}}(\rho) + i J_{\frac{m-1}{2}}(\rho)] \cos(m\theta),$$

Diffraction from designed radial structures: Spatially asymmetric beams

$$t(\theta) = \frac{1}{2}(e^{im\theta} + e^{in\theta})$$

$$t(\theta) = \cos\left(\frac{m-n}{2}\theta\right) \exp\left(i\frac{m+n}{2}\theta\right)$$

$$t(\theta) = \left| \cos\left(\frac{m-n}{2}\theta\right) \right| \exp[i\phi(\theta)].$$

$$\phi(\theta) = \delta(\theta) + \frac{m+n}{2}\theta,$$

where $\delta(\theta)$ is a binary periodic function alternating between 0 and π with a period of $4\pi/(m-n)$.

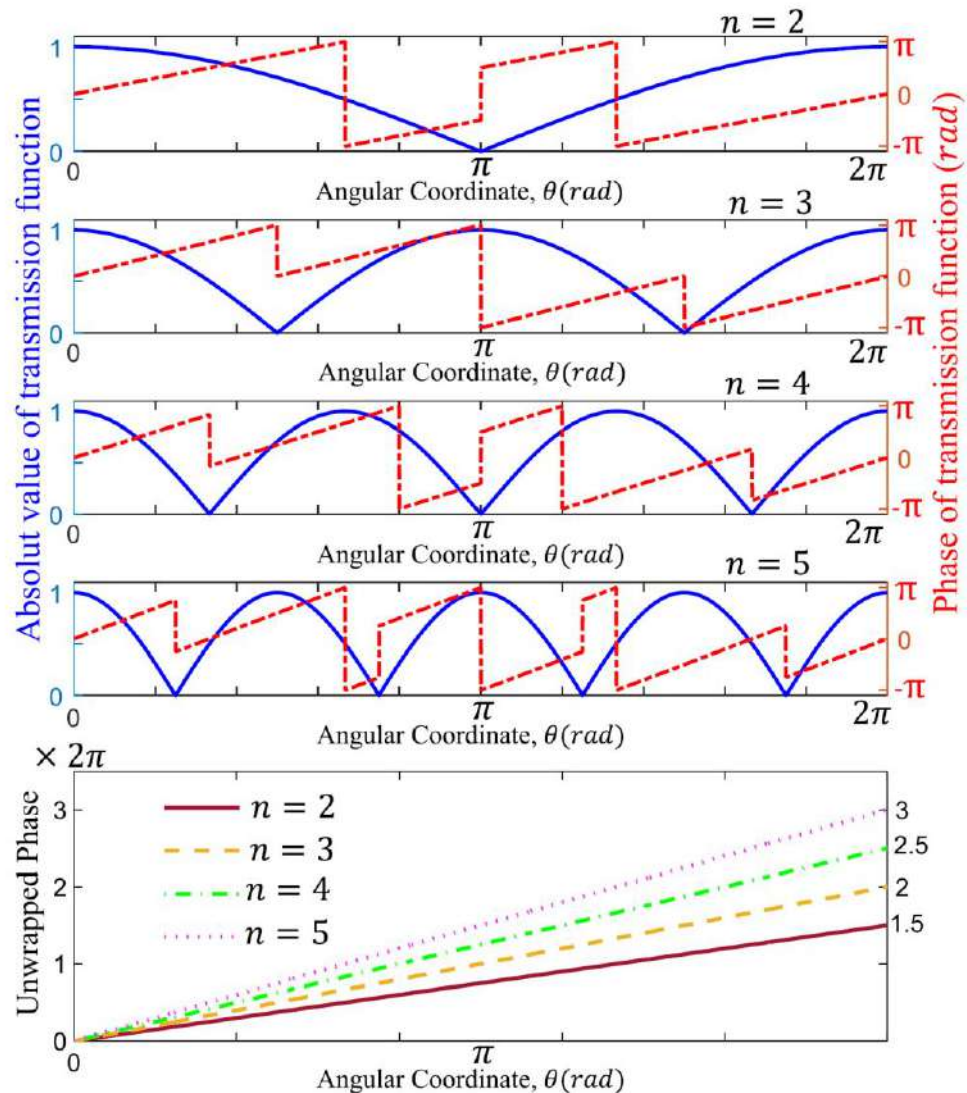
The light beam topological charge can be calculated using

$$\frac{1}{2\pi} \oint_C \nabla\phi \cdot d\mathbf{r}$$

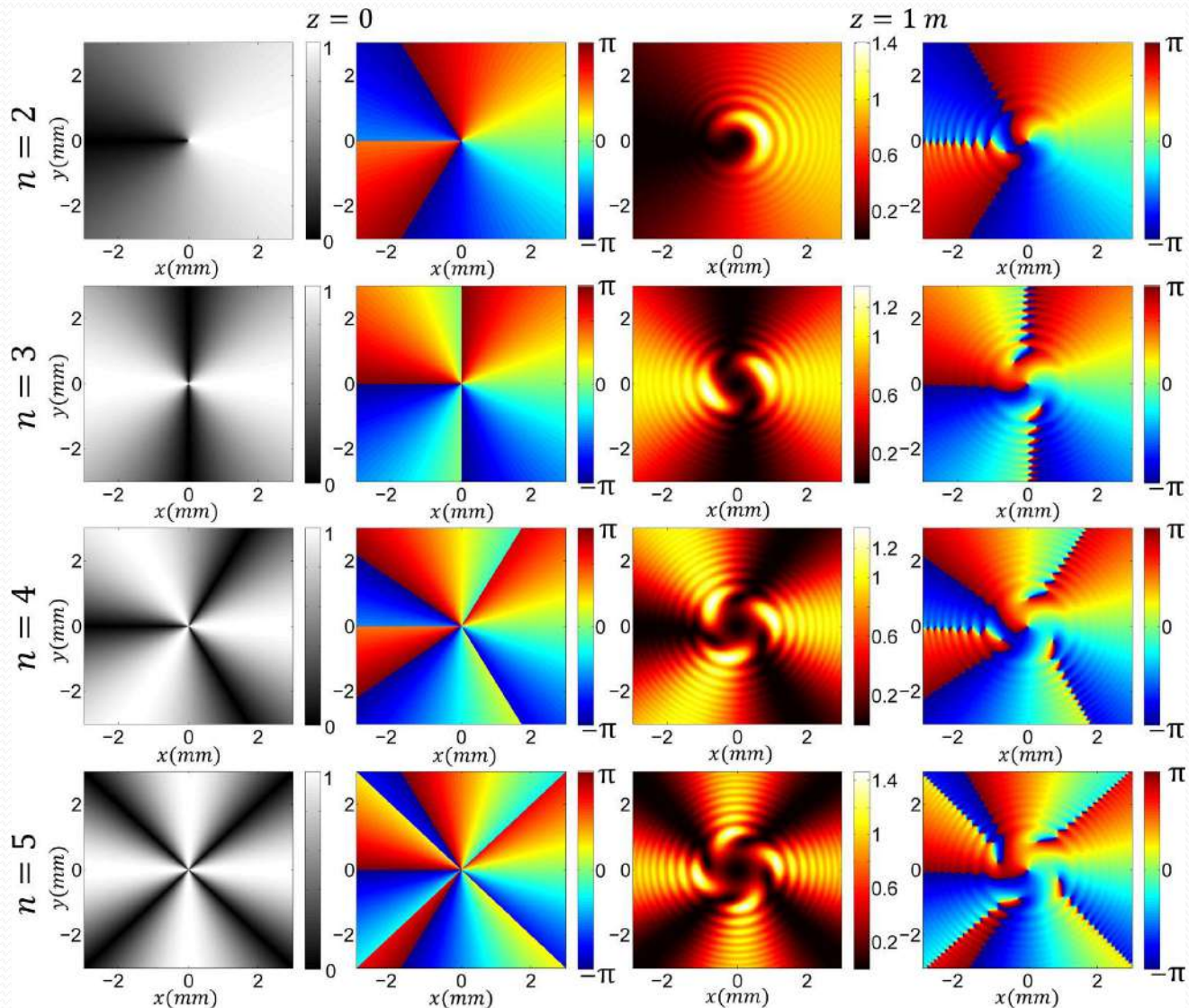
with loop C enclosing the singularity.

First to fourth rows: Absolute value (blue solid line) and phase (red dash line) profiles of $t(\theta)$ for $n = 2, 3, 4, 5$ and $m = 1$, respectively. Fifth row: The corresponding unwrapped phase profiles.

This transmittance imposes an OAM on an incident plane wave with a topological charge of order $(m+n)/2$.



Spatially asymmetric beams



$$t(\theta) = \frac{1}{2}(e^{im\theta} + e^{in\theta})$$

at $z = 1\text{ m}$ for $n = 2, 3, 4, 5$ and $m = 1$

Categorization of the solutions

$$U(r, \theta, z = 0) = t(\theta) = t_0 + \sum_{n=1}^{+\infty} (t_n e^{in\theta} + t_{-n} e^{-in\theta}),$$

Radial Carpet Beams

We consider $t_n = t_{-n} \longrightarrow t(\theta) = t_0 + \sum_{n=1}^{+\infty} t_n \cos(n\theta), \longrightarrow$

$$U(r, \theta, z) = e^{ikz} \left\{ t_0 + \sqrt{\rho} e^{i\rho} \sum_{n=1}^{+\infty} u_n \cos(n\theta) \right. \\ \left. \times \left[J_{\frac{n+1}{2}}(\rho) + i J_{\frac{n-1}{2}}(\rho) \right] \right\},$$

If we set $t_0 = 0$, the radial carpet beams take **petallike forms**.

$$u_n = \sqrt{\frac{\pi}{2}} (-i)^{\frac{n}{2}+1} t_n.$$

By eliminating t_0 and all of the terms with t_n or t_{-n} in the summation:

$$t_{\pm}(\theta) = \sum_{n=1}^{+\infty} t_n \exp(\pm in\theta)$$

Ringlike Vortex Beams

or

Twisted-intensity Ringlike Vortex Beams

$$U_{\pm}(r, \theta, z) = e^{ikz} \left\{ \sqrt{\rho} e^{i\rho} \sum_{n=1}^{+\infty} u_n \exp(\pm in\theta) \right. \\ \left. \times \left[J_{\frac{n+1}{2}}(\rho) + i J_{\frac{n-1}{2}}(\rho) \right] \right\},$$

$$u_n = \sqrt{\frac{\pi}{2}} (-i)^{\frac{n}{2}+1} t_n.$$

Fourier expansions of the **parabolic** and **triangular** transmission functions are given by

$$t^{\text{Pa}}(\theta) = \frac{1}{3} + \sum_{q=1}^{+\infty} \frac{4}{(\pi q)^2} \cos(qm\theta)$$

$$t^{\text{Tr}}(\theta) = \frac{1}{2} + \sum_{\substack{q=1 \\ \text{odd}}}^{+\infty} \frac{4}{(\pi q)^2} \cos(qm\theta)$$

By eliminating the dc terms

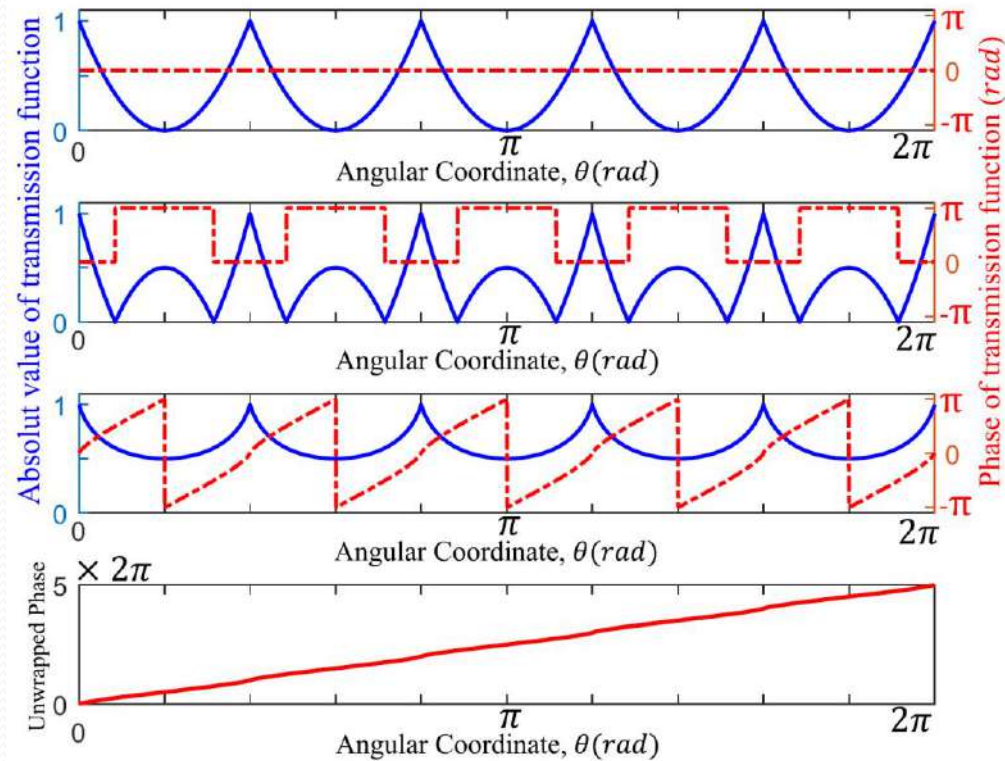
$$t_{t_0=0}^{\text{Pa}}(\theta) = \frac{3}{2} \sum_{q=1}^{+\infty} \frac{4}{(\pi q)^2} \cos(qm\theta)$$

$$t_{t_0=0}^{\text{Tr}}(\theta) = 2 \sum_{\substack{q=1 \\ \text{odd}}}^{+\infty} \frac{4}{(\pi q)^2} \cos(qm\theta)$$

By replacing $\cos(qm\theta)$ by $\exp(iqm\theta)$

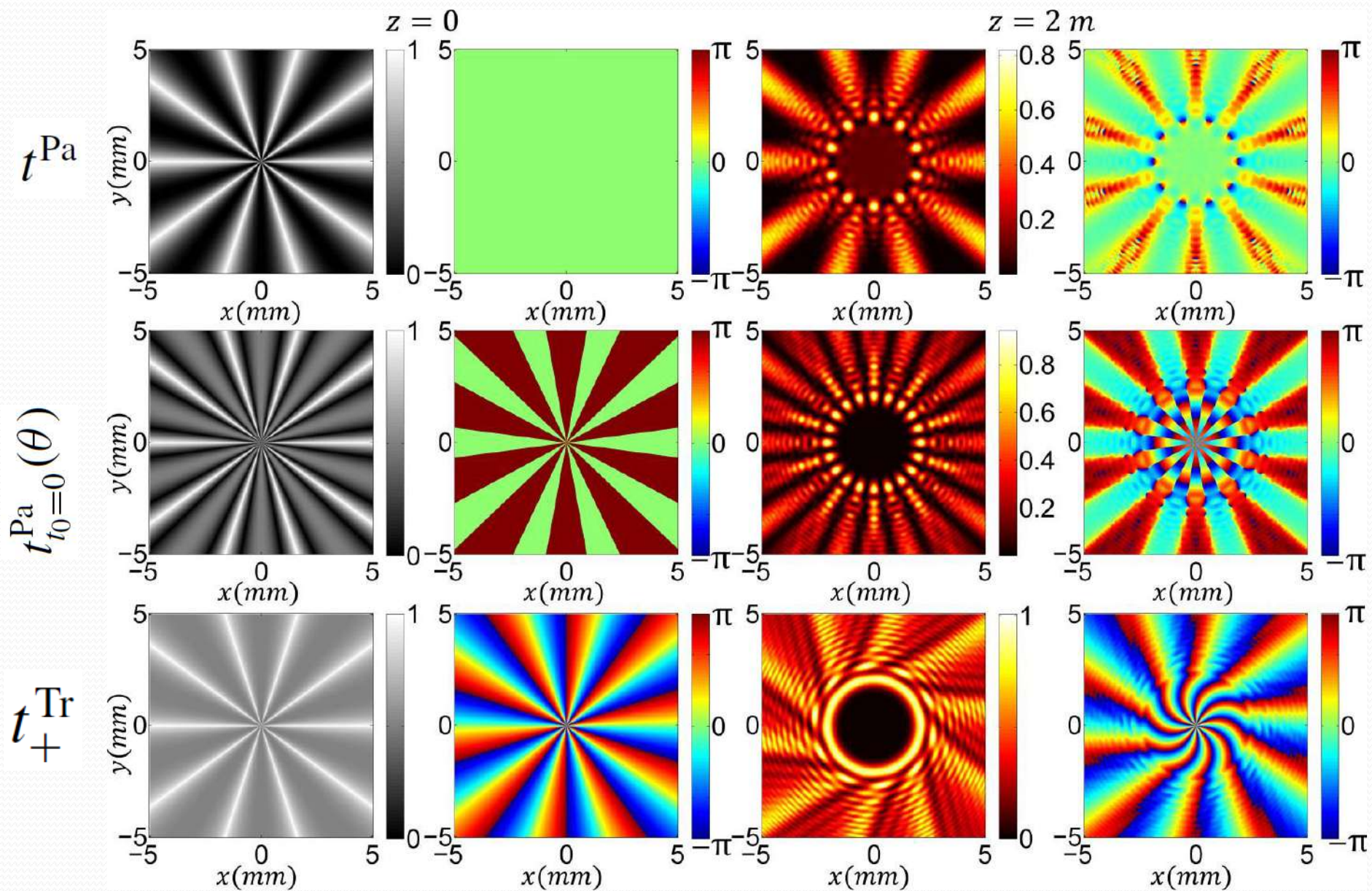
$$t_{\pm}^{\text{Pa}}(\theta) = \frac{3}{2} \sum_{q=1}^{+\infty} \frac{4}{(\pi q)^2} \exp(\pm iqm\theta)$$

$$t_{\pm}^{\text{Tr}}(\theta) = 2 \sum_{\substack{q=1 \\ \text{odd}}}^{+\infty} \frac{4}{(\pi q)^2} \exp(\pm iqm\theta).$$



$t^{\text{Pa}}(\theta)$, $t_{t_0=0}^{\text{Pa}}(\theta)$, and t_+^{Pa} for $m = 5$
Unwrapped phase profile of t_+^{Pa} .

Parabolic for $m=5$



Fourier expansions of the parabolic and triangular transmission functions are given by

$$t^{\text{Pa}}(\theta) = \frac{1}{3} + \sum_{q=1}^{+\infty} \frac{4}{(\pi q)^2} \cos(qm\theta)$$

$$t^{\text{Tr}}(\theta) = \frac{1}{2} + \sum_{\substack{q=1 \\ \text{odd}}}^{+\infty} \frac{4}{(\pi q)^2} \cos(qm\theta)$$

By eliminating the dc terms

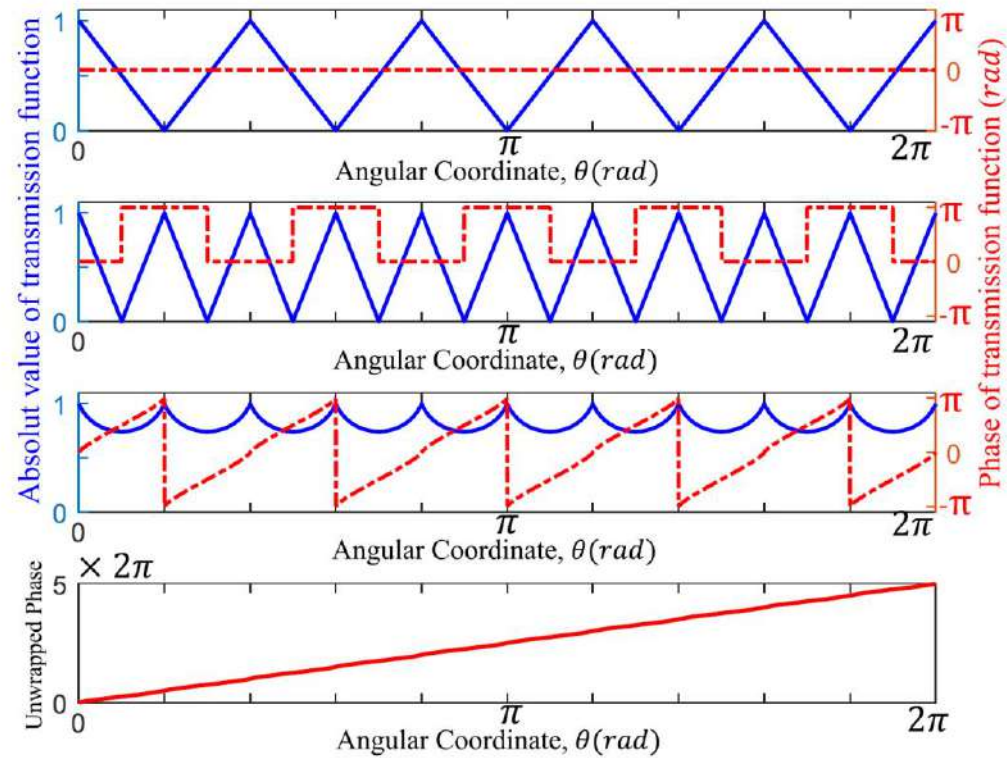
$$t_{t_0=0}^{\text{Pa}}(\theta) = \frac{3}{2} \sum_{q=1}^{+\infty} \frac{4}{(\pi q)^2} \cos(qm\theta)$$

$$t_{t_0=0}^{\text{Tr}}(\theta) = 2 \sum_{\substack{q=1 \\ \text{odd}}}^{+\infty} \frac{4}{(\pi q)^2} \cos(qm\theta)$$

By replacing $\cos(qm\theta)$ by $\exp(iqm\theta)$

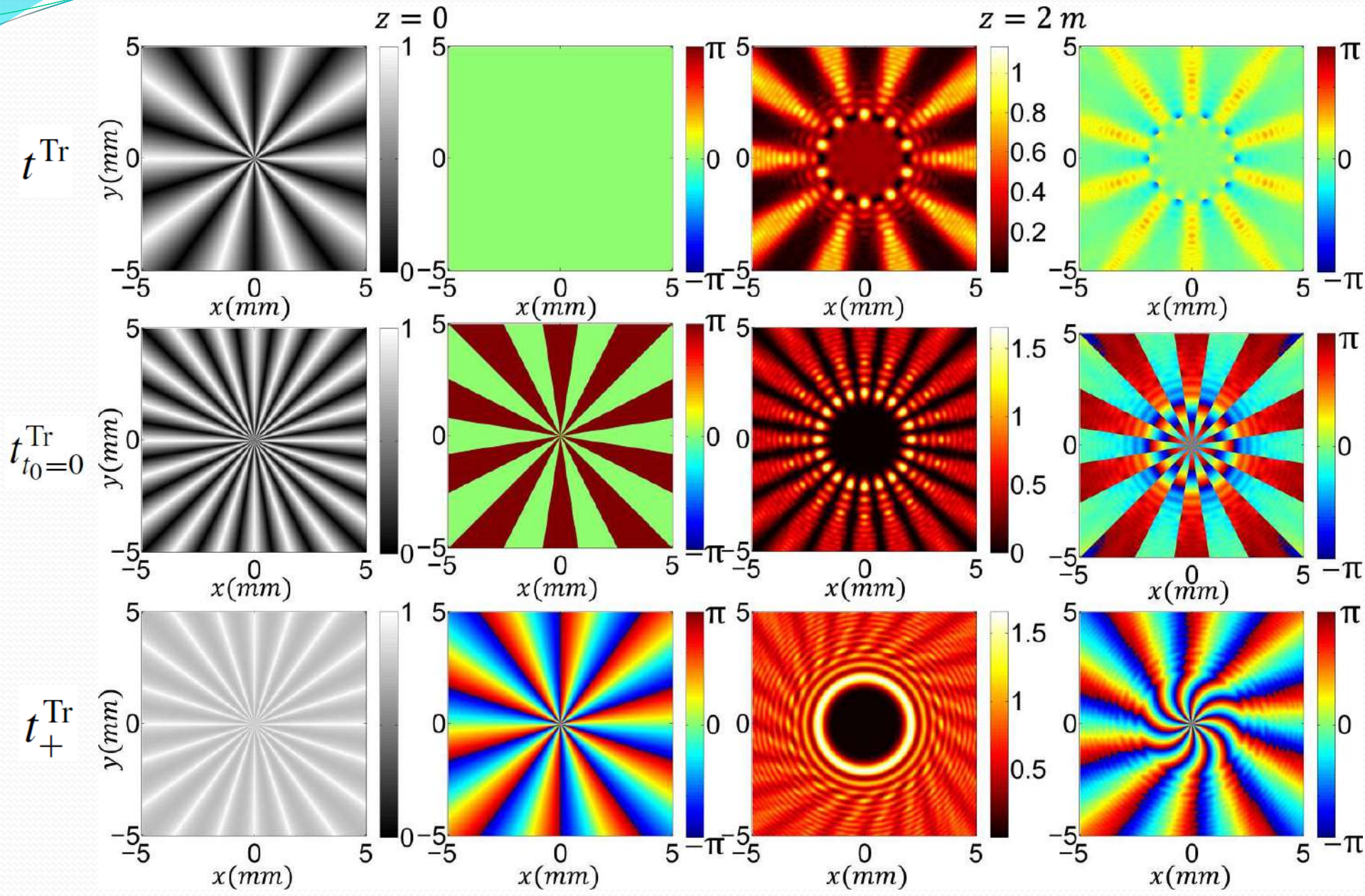
$$t_{\pm}^{\text{Pa}}(\theta) = \frac{3}{2} \sum_{q=1}^{+\infty} \frac{4}{(\pi q)^2} \exp(\pm iqm\theta)$$

$$t_{\pm}^{\text{Tr}}(\theta) = 2 \sum_{\substack{q=1 \\ \text{odd}}}^{+\infty} \frac{4}{(\pi q)^2} \exp(\pm iqm\theta).$$



$t^{\text{Tr}}(\theta)$, $t_{t_0=0}^{\text{Tr}}(\theta)$, and t_{+}^{Tr} for $m = 5$.
Unwrapped phase profile of t_{+}^{Tr} .

Triangular for $m=5$

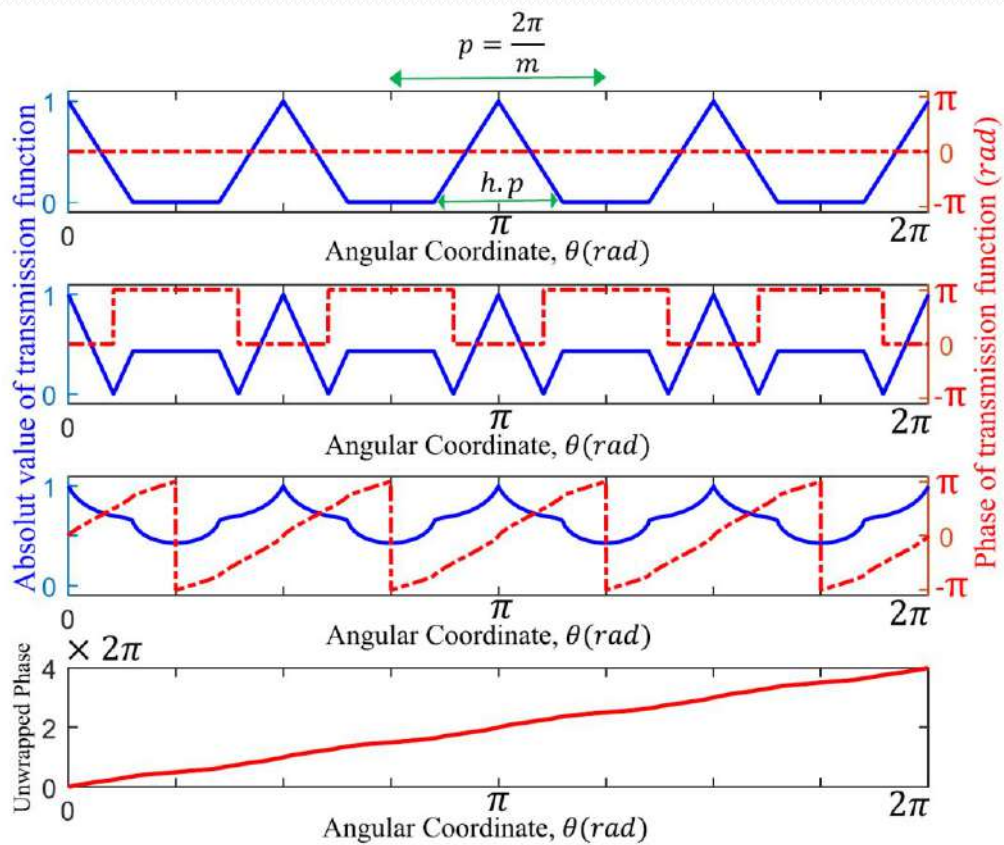


Fourier expansion of a modified form of the triangle transmission function.

$$t^{MTr}(\theta) = t_0 + \sum_{q=1}^{+\infty} t_q \cos(qm\theta)$$

$$t_0 = \frac{h}{2}, \quad t_q = \frac{2}{h(q\pi)^2} [1 - \cos(q\pi h)]$$

h is the aperture ratio



$t^{MTr}(\theta)$, $t_{t_0=0}^{MTr}(\theta)$, and t_+^{MTr} for $m = 4$ and $h = 0.6$

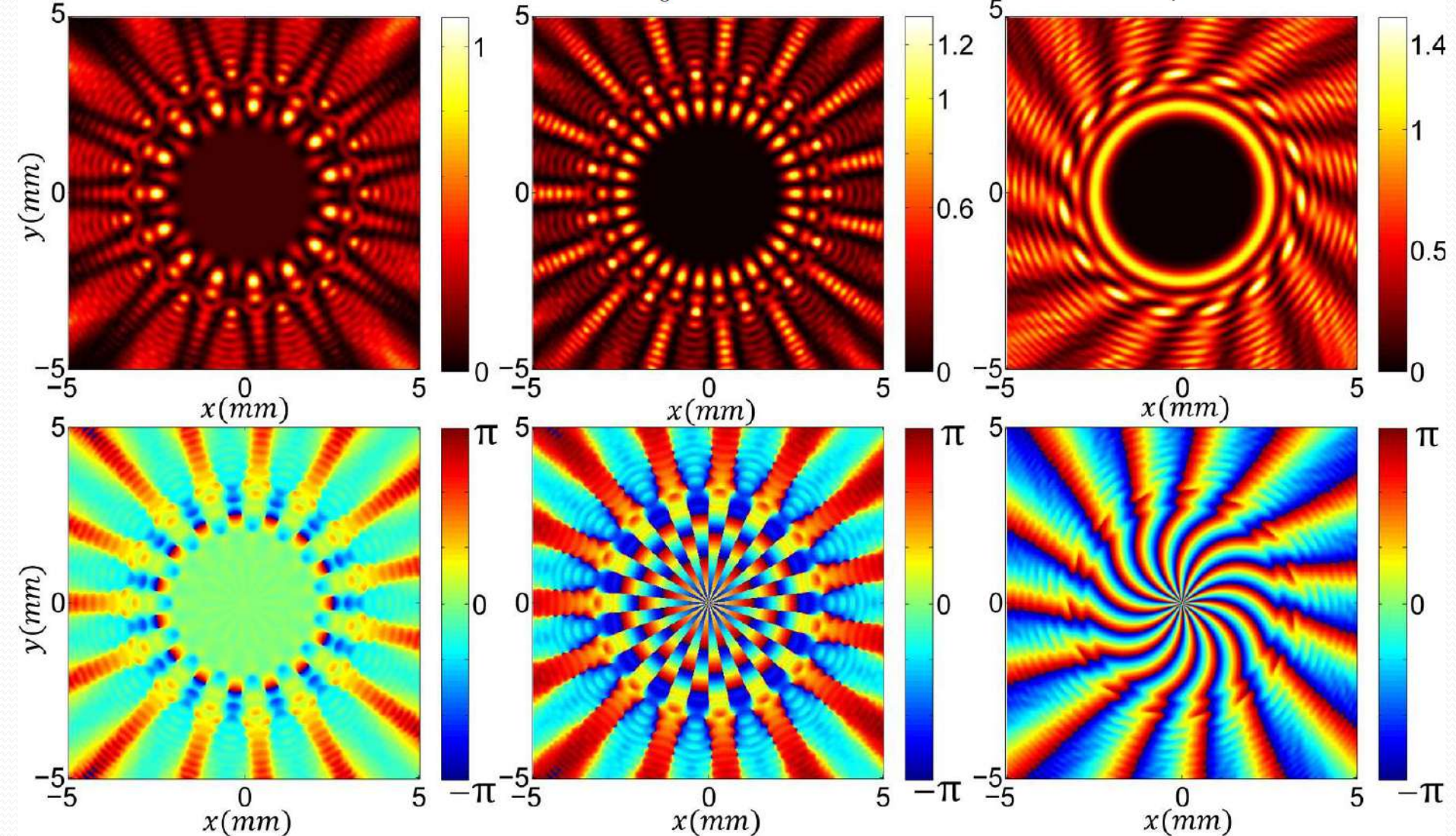
Unwrapped phase profile of t_+^{MTr} .

Intensity and phase patterns of the beams generated by **modified triangular transmission functions** at $z = 2$ m with $m = 15$ and $h = 0.6$, respectively.

t^{MTr}

$t_{t_0=0}^{MTr}(\theta)$

t_+^{MTr}



An azimuthally-modified linear phase grating: Generation of varied radial carpet beams over different diffraction orders with controlled intensity sharing among the generated beams

$$T(\rho, \theta) = \exp\left[i\gamma \cos\left(\frac{2\pi}{\mathcal{A}} \rho \cos \theta + \cos l\theta\right)\right]$$

We integrate features of linear and radial gratings to introduce a new grating that, in addition to the properties of linear and radial gratings, has additional properties.

We construct this type of grating by adding an azimuthal periodic dependency to the argument of the transmission function of a linear phase grating that has a sinusoidal profile and we call them **azimuthally-modified linear phase gratings (AMLPGs)**.

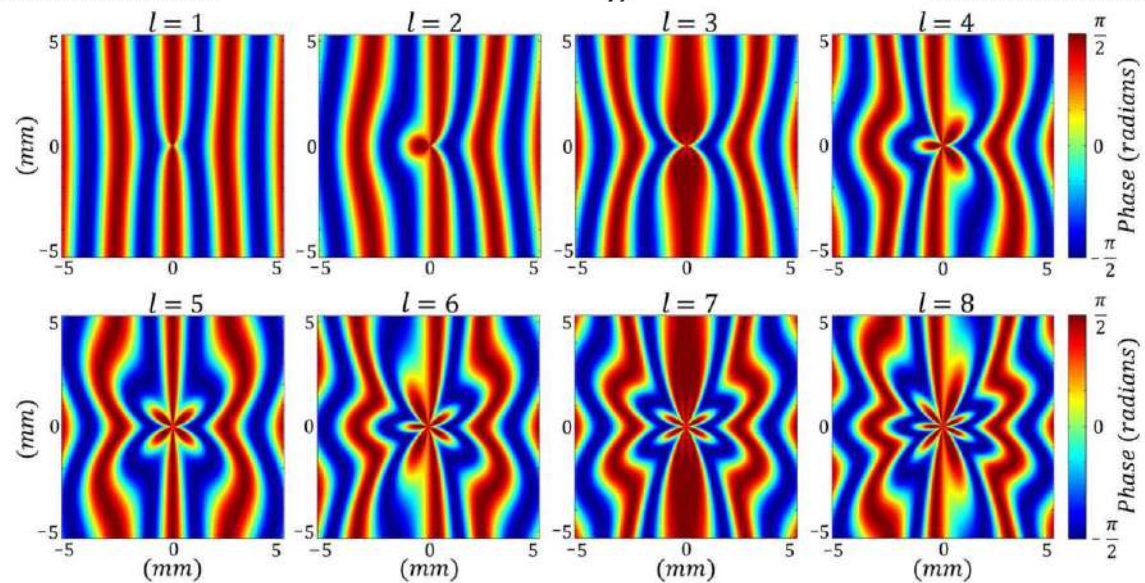


Figure 1. Illustration of eight typical AMLPGs with $d = 3$ mm, $\gamma = \pi/2$, and different values of l .

$$U_s(r_s, \varphi_s, z) = e^{ikz} e^{i\alpha r_s^2} \left\{ (i)^s J_s(\gamma) J_0(s) e^{-i\alpha r_s^2} + \sum_{q=1}^{+\infty} (i)^s (i)^{-q(\frac{l}{2}-1)-1} J_s(\gamma) J_q(s) r_s \left(\frac{\pi}{\sqrt{\lambda z}}\right) e^{-\frac{i\alpha r_s^2}{2}} \right. \\ \left. \times \left[J_{\frac{ql+1}{2}}\left(\frac{\alpha r_s^2}{2}\right) + i J_{\frac{ql-1}{2}}\left(\frac{\alpha r_s^2}{2}\right) \right] \cos(ql\varphi_s) \right\}, \quad s = 0, \pm 1, \pm 2, \dots$$

Controlled intensity sharing among different diffraction orders: Effect of γ on the resulting patterns

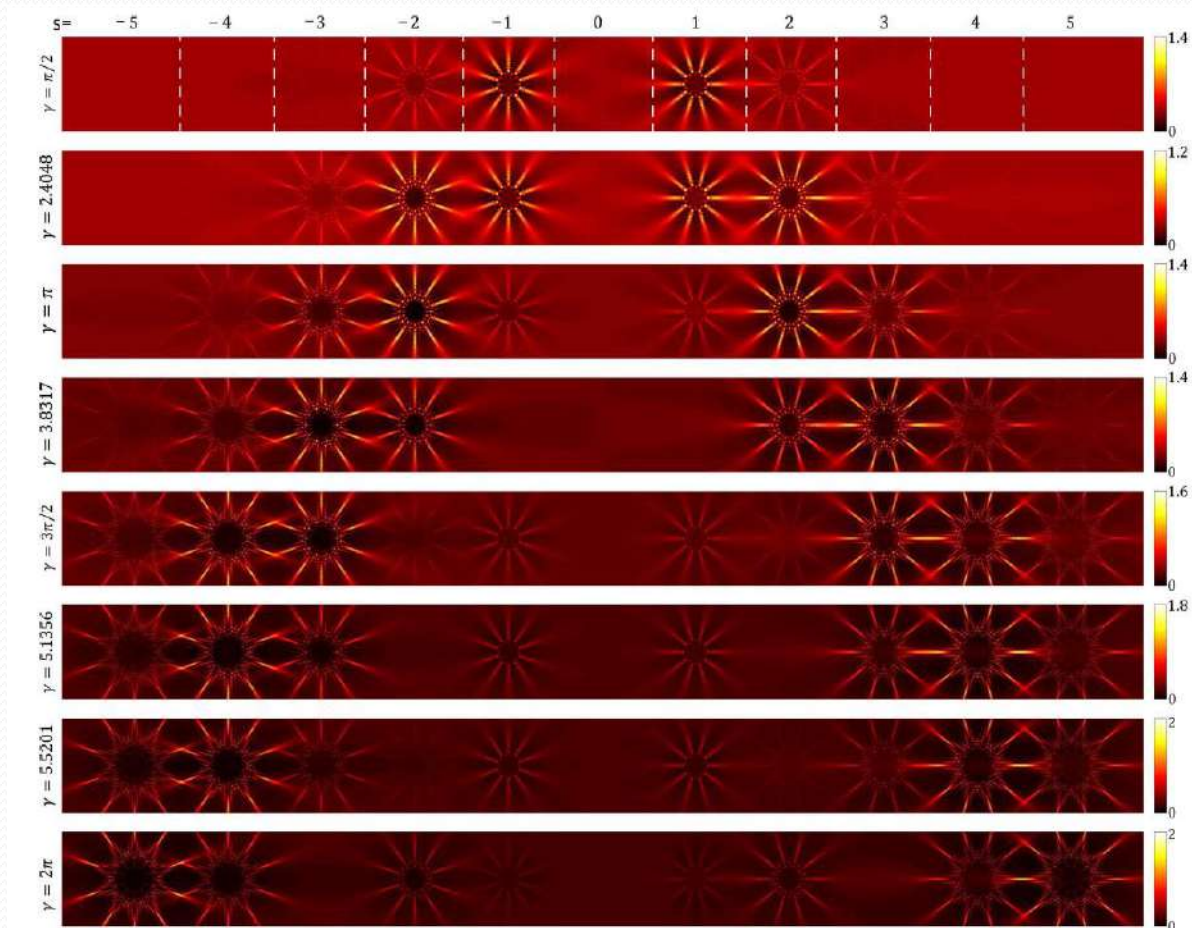


Figure 2. Controlled intensity sharing among the different diffraction orders of an AMLPG by adjusting the value of the phase amplitude, γ . Calculated intensity patterns of different diffracted beams in the diffraction of a plane wave from an AMLPG having $l = 10$ and different values of γ : $\pi/2$, 2.4048, π , 3.8317, $3\pi/2$, 5.1356, 5.5201, and 2π at $z = 555$ cm. The intensity over the patterns is normalized to the intensity of the incident beam (for details see the color bars). The dashed white lines in the first row show the boundaries of the different diffraction orders.

Comparison of the diffraction patterns of an AMLPG and a radial phase grating

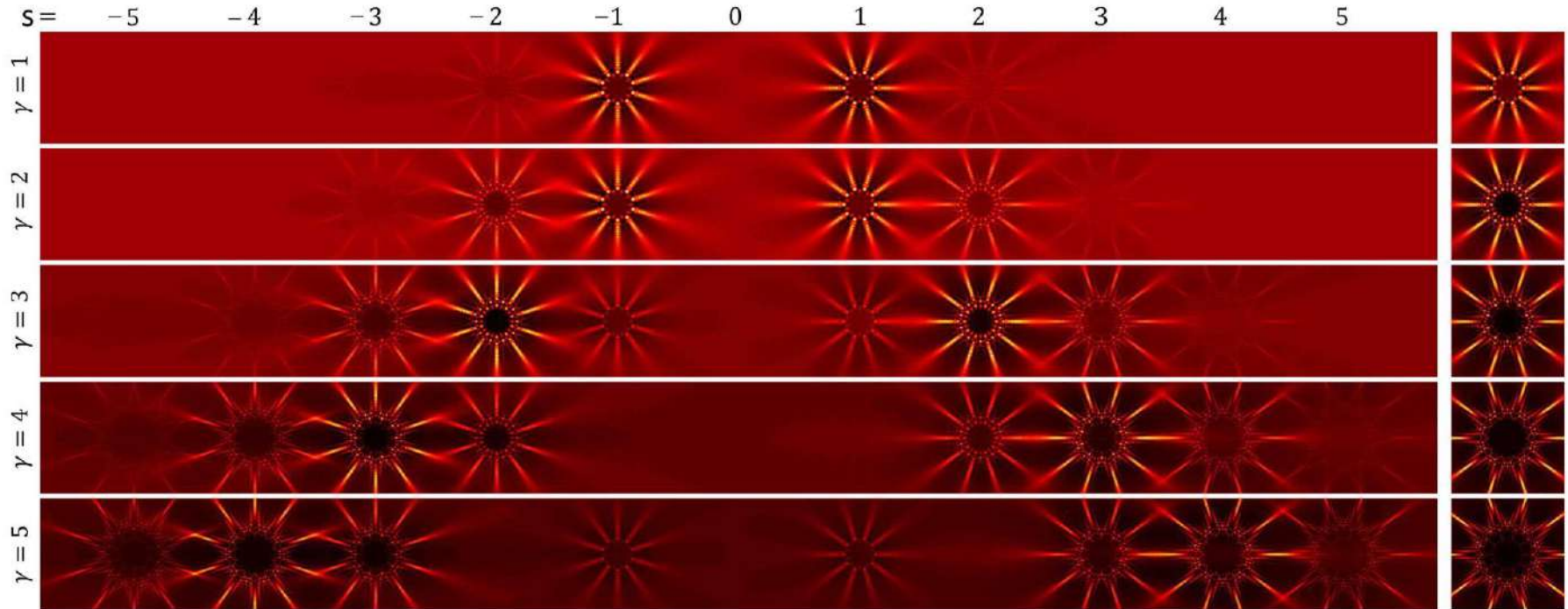


Figure 3. Comparing the diffraction patterns of an AMLPG and a radial phase grating having the same number of spokes. Left column, calculated diffracted intensity patterns obtained in the diffraction of a plane wave from an AMLPG with $l = 10$ at $z = 555$ cm for γ equal to 1, 2, 3, 4, and 5. Right column, calculated diffracted intensity patterns obtained in the diffraction of a plane wave from a radial grating with $l = 10$ at $z = 555$ cm for γ equal to 1, 2, 3, 4, and 5³¹. In each row, for $s = \gamma$, the s -th diffraction order of the AMLPG has the maximum value of intensity between all the diffraction orders and its diffraction pattern and the illustrated radial carpet pattern at the right column has the same form. The intensity over the patterns is normalized to the intensity of the incident beam.

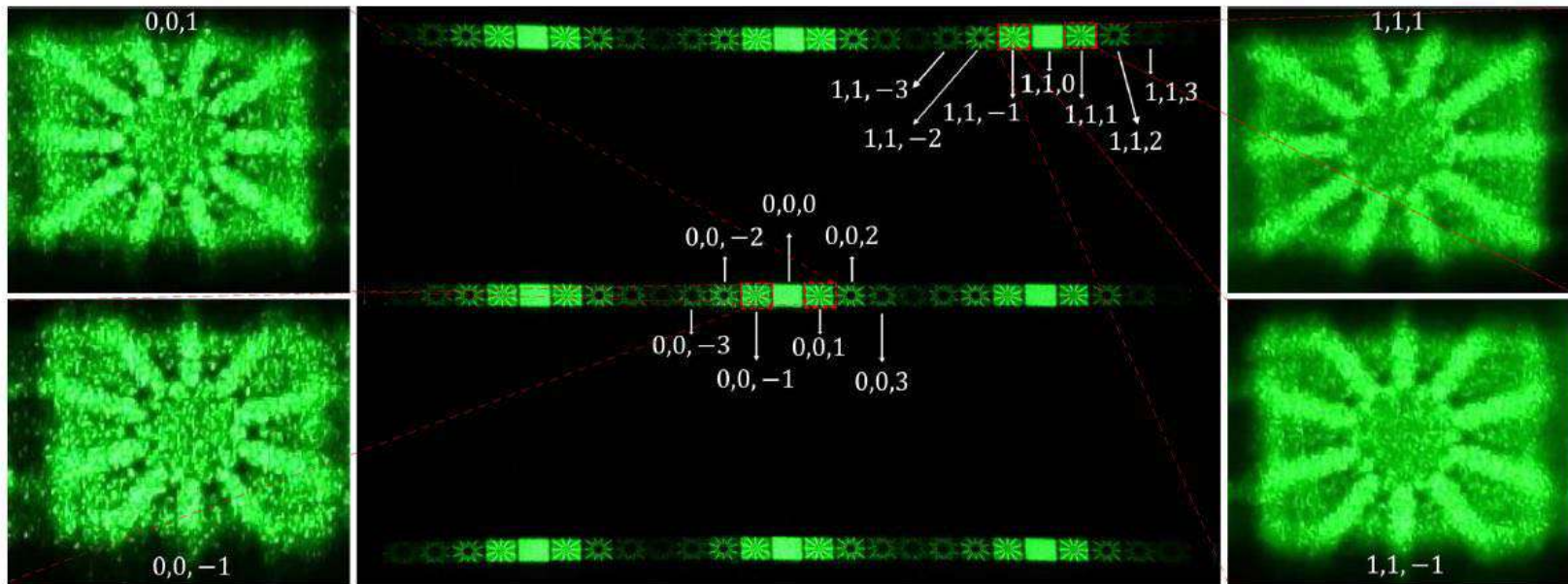


Figure 6. Central pattern: The diffraction pattern of a plane wave from an SLM with $\gamma = \pi/2$ when an AMLPG is imposed on the SLM. Here a diffuser is placed at $z = 350$ cm and the diffraction pattern is imaged by camera. For the radial phase structure $l = 10$ and for the linear phase grating $d = 0.11$ mm. The diffraction patterns of four typical diffraction orders are enlarged in the first and third columns.

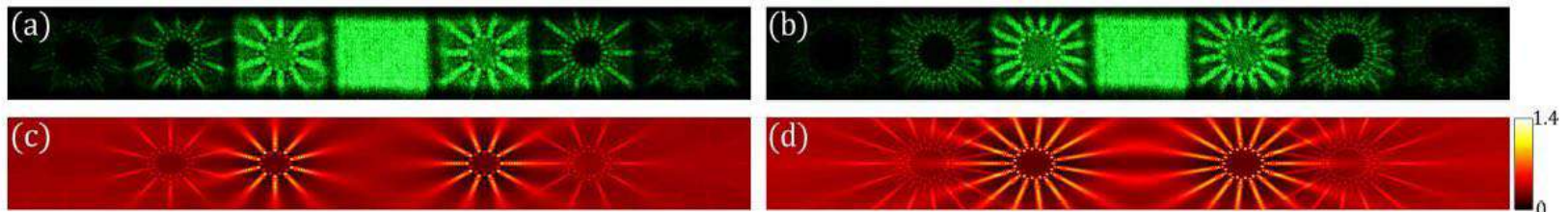


Figure 7. (a) and (b) are experimental diffraction patterns of two AMLPGs with $l = 10$ and $l = 15$ at $z = 350$ cm, respectively. These patterns are generated over the (0,0) diffraction order of the SLM. Here $\gamma = \pi/2$. (c) and (d) are the corresponding theoretical patterns. The intensity over the simulated patterns is normalized to the intensity of the incident beam, and for this reason a color bar is used for (c) and (d).

Relative rotation of the resulting patterns over +s and -s diffraction orders

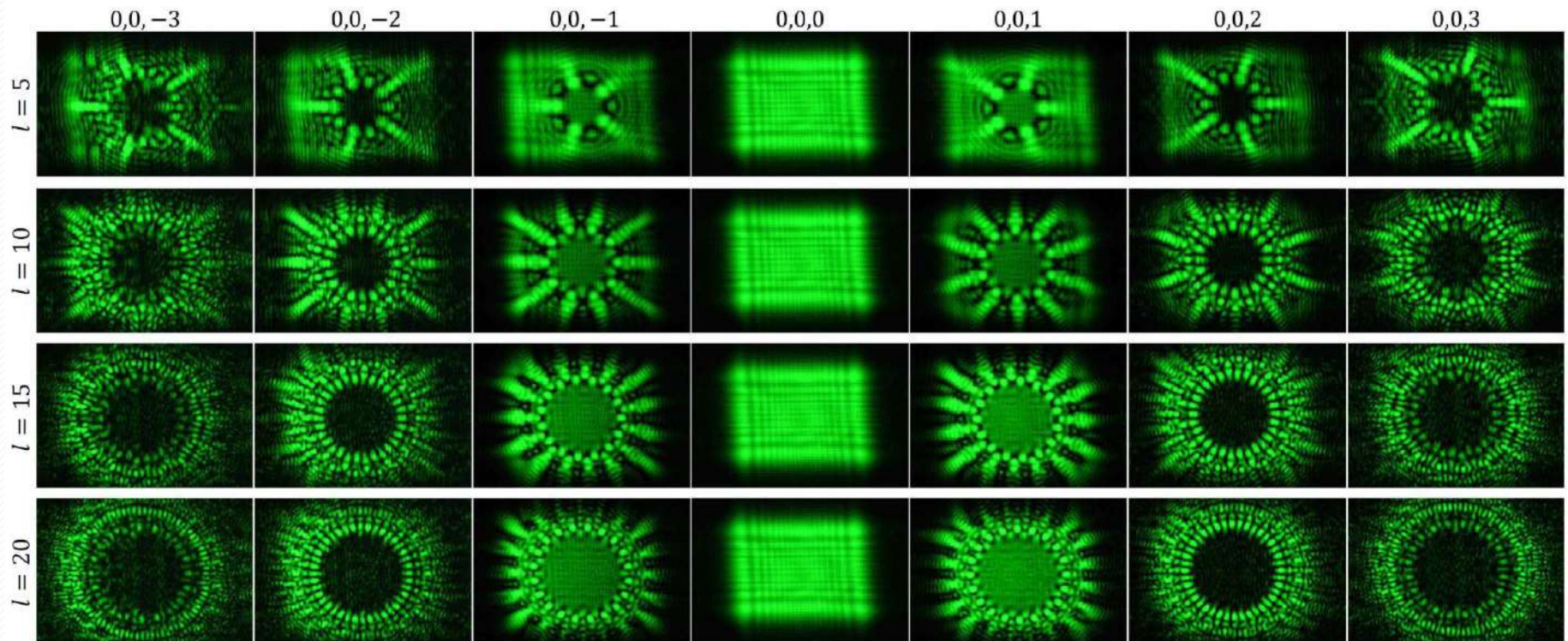


Figure 8. Experimentally generated diffraction patterns of four AMLPGs with $l = 5$, $l = 10$, $l = 15$, $l = 20$, and $\gamma = \pi/2$. Each of the individual patterns was formed directly on the active area of the camera at a distance of $z = 555$ cm. A set of low contrast crossed linear fringes appear over the central patterns $(0,0,0)$. These fringes are the edge diffraction patterns of the SLM window.

Talbot effect of azimuthally periodic Bessel-based structures

Azimuthally periodic Bessel-based structures (APBBSs), sinusoidal and binary-like single- and multi-frequency APBBSs

Transmission function of a single-frequency

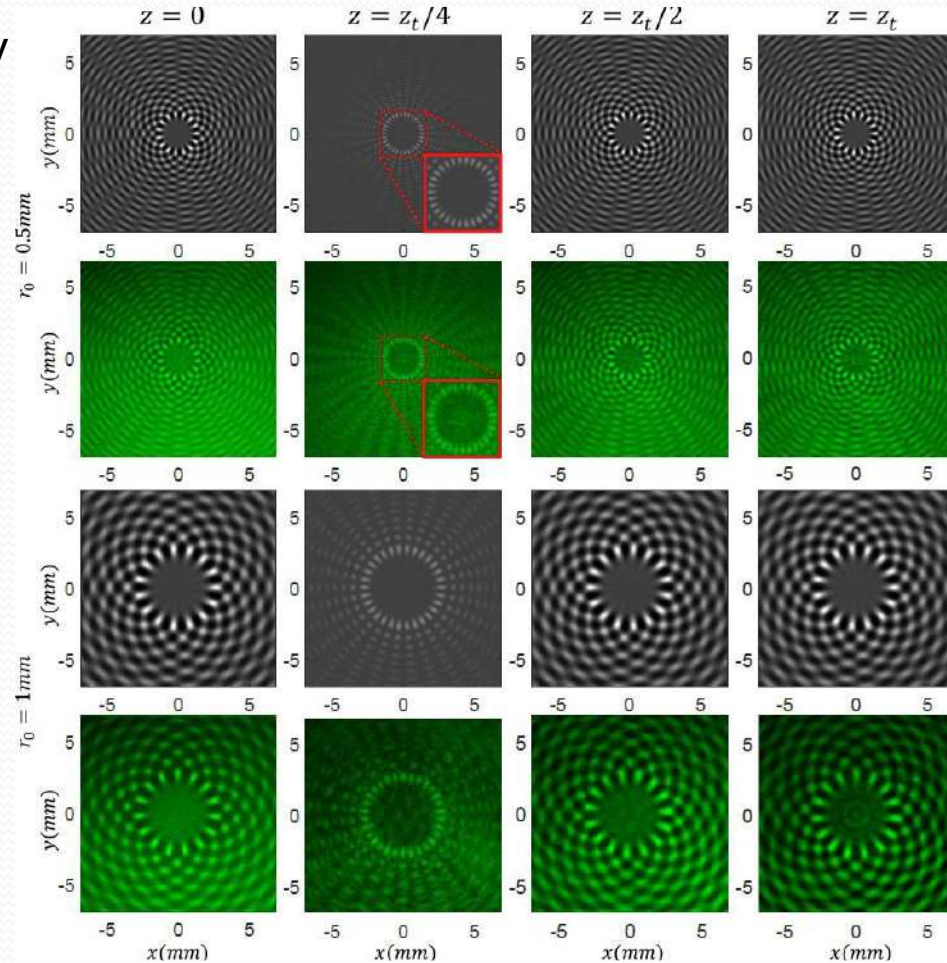
$$t(r, \theta) = c + \sum_{n=0}^{\infty} t_n J_n \left(\frac{2\pi r}{r_0} \right) \cos(n\theta)$$

$$\psi_0(r, \theta) = c + \sum_{n=0}^{\infty} t_n J_n(2\pi\rho_0 r) \cos(n\theta)$$

$$\psi_z(r, \theta) = c + e^{-2i\pi\left(\frac{z}{z_t}\right)} \sum_{n=0}^{\infty} t_n J_n(2\pi\rho_0 r) \cos(n\theta)$$

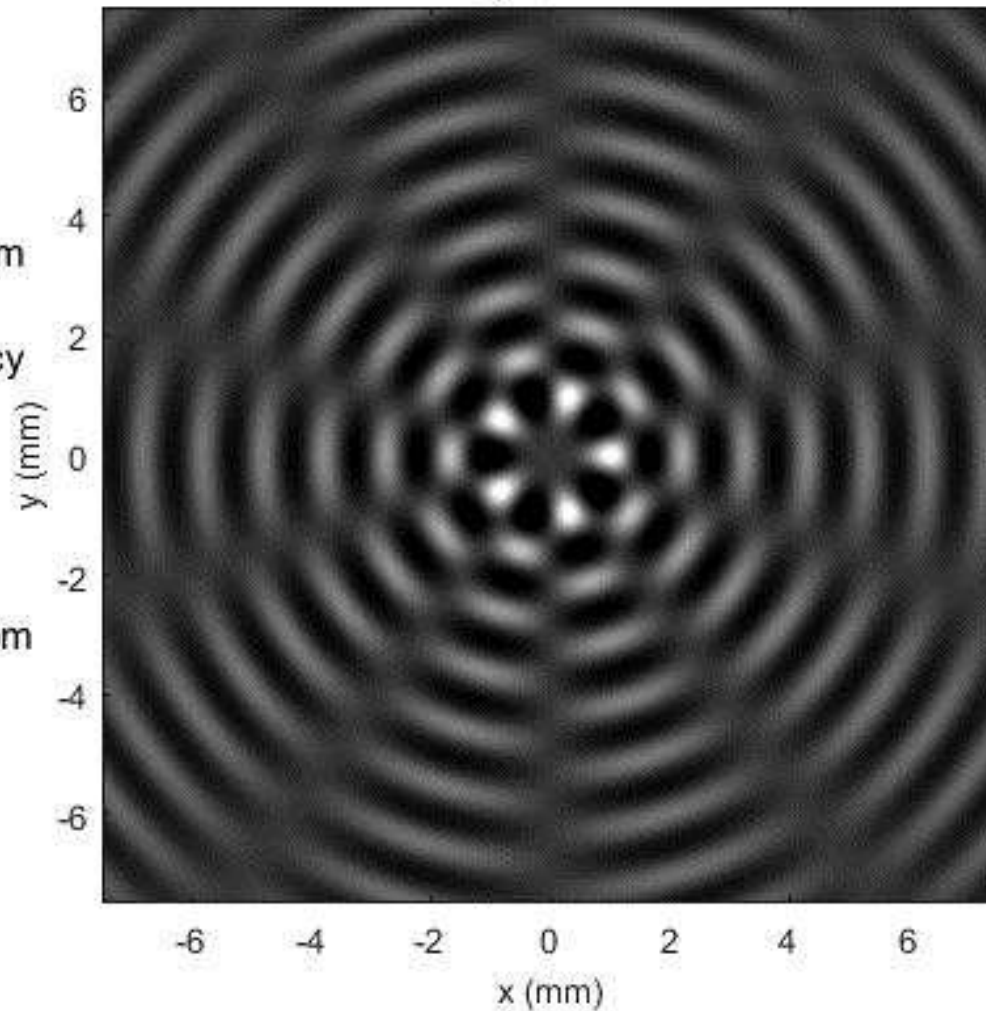
For a sinusoidal single-frequency APBBS

$$t(r, \theta) = \frac{1}{2} \left[1 + a_m J_m \left(\frac{2\pi r}{r_0} \right) \cos(m\theta) \right]$$



$$z = 0(z_t/4)$$

Calculated near-field diffraction patterns of a plane wave from a sinusoidal single-frequency APBBS with $m=5$ and $r_0=1$ mm under propagation from $z=0$ to $z=z_t$.

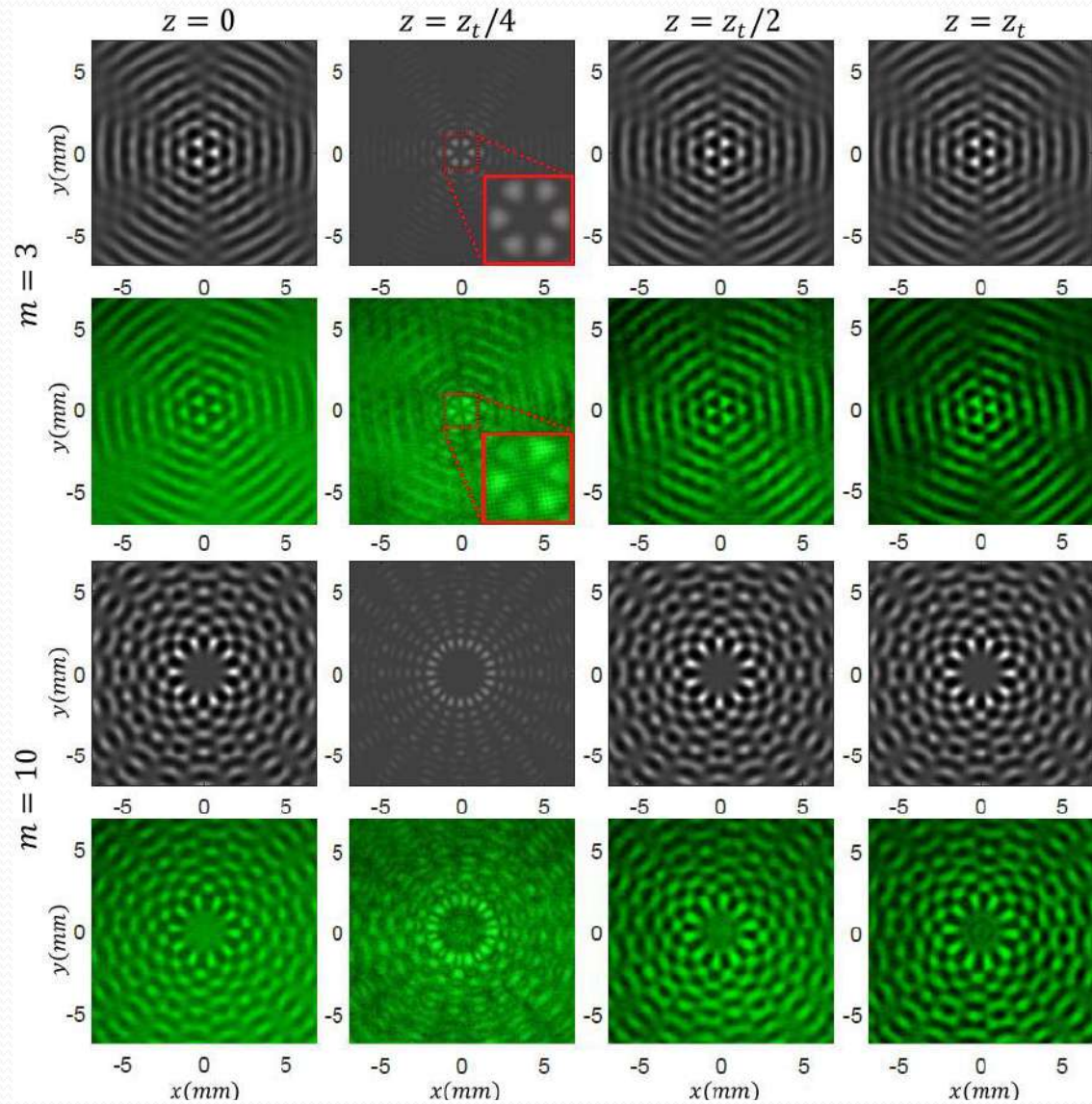


Transmission function of a binary-like single-frequency APBBS

$$t(r, \theta) = \frac{1}{2} \left[1 + a_m \sum_{q=1}^{\infty} s_q J_{qm} \left(\frac{2\pi r}{r_0} \right) \cos(qm\theta) \right]$$

$$s_q = \frac{4}{q\pi} \sin\left(\frac{q\pi}{2}\right)$$

$$a_m = 1 / \max\left\{ \sum_{q=1}^{\infty} s_q J_{qm} \left(\frac{2\pi r}{r_0} \right) \cos(qm\theta) \right\}$$



Transmission function of a multi-frequency APBBS

$$t(r, \theta) = t_{00} + \sum_{l=1}^{\infty} \sum_{n=0}^{\infty} t_{ln} J_n \left(2\pi\sqrt{l} \frac{r}{r_0} \right) \cos(n\theta)$$

$$\psi_z(r, \theta) = t_{00} + \sum_{l=1}^{\infty} \sum_{n=0}^{\infty} e^{-2i\pi l \left(\frac{z}{z_t} \right)} t_{ln} J_n(2\pi\rho_l r) \cos(n\theta)$$

$$z_t = \frac{2}{\lambda\rho_0^2} = \frac{2r_0^2}{\lambda}$$

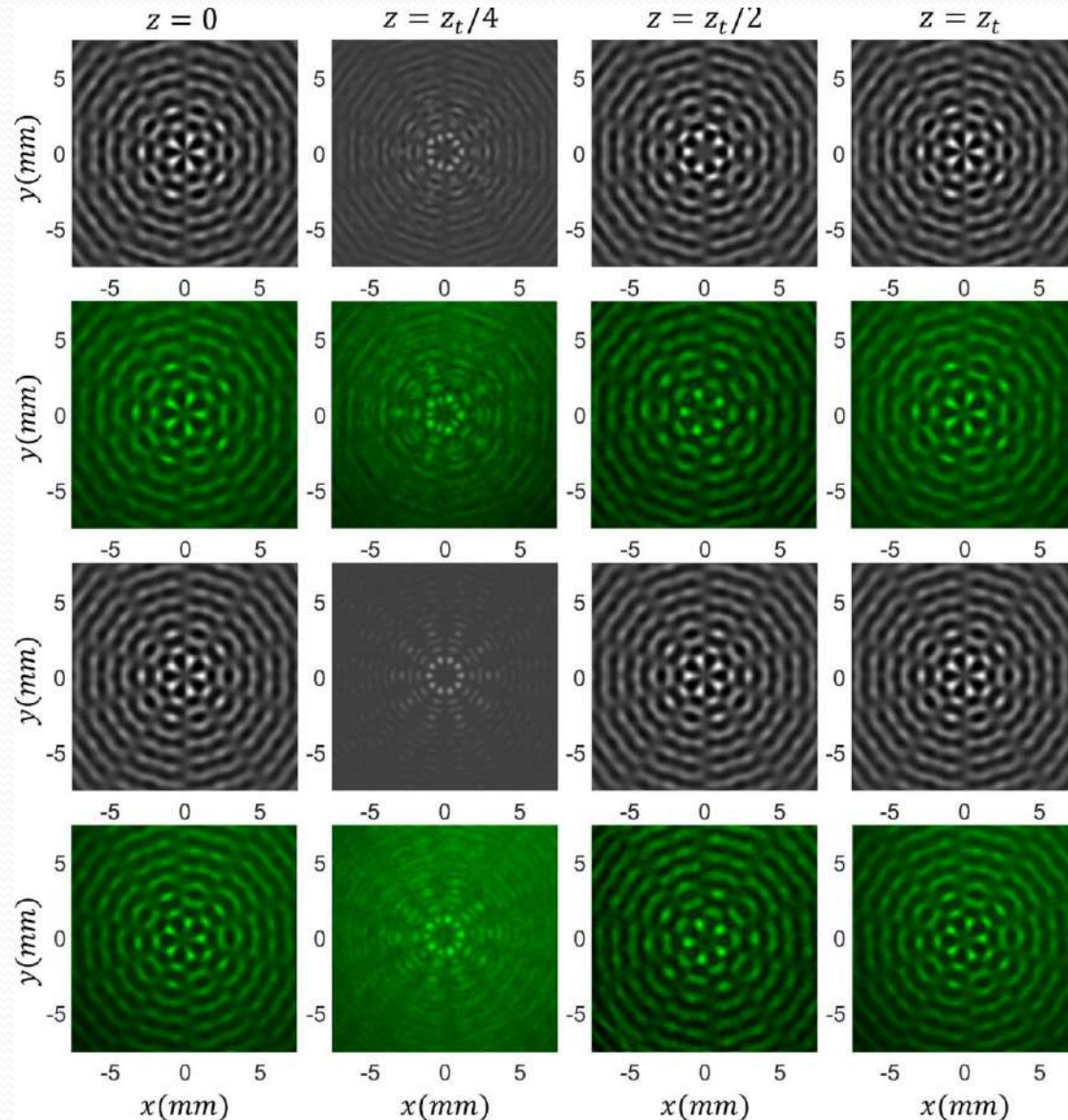
Transmittance of a binary-like multi-frequency APBBS

$$t(r, \theta) = \frac{1}{2} \left[1 + a \sum_{l=1}^{\infty} \sum_{q=1}^{\infty} \frac{s_q}{l^2} J_{qm}(2\pi\rho_l r) \cos(qm\theta) \right]$$

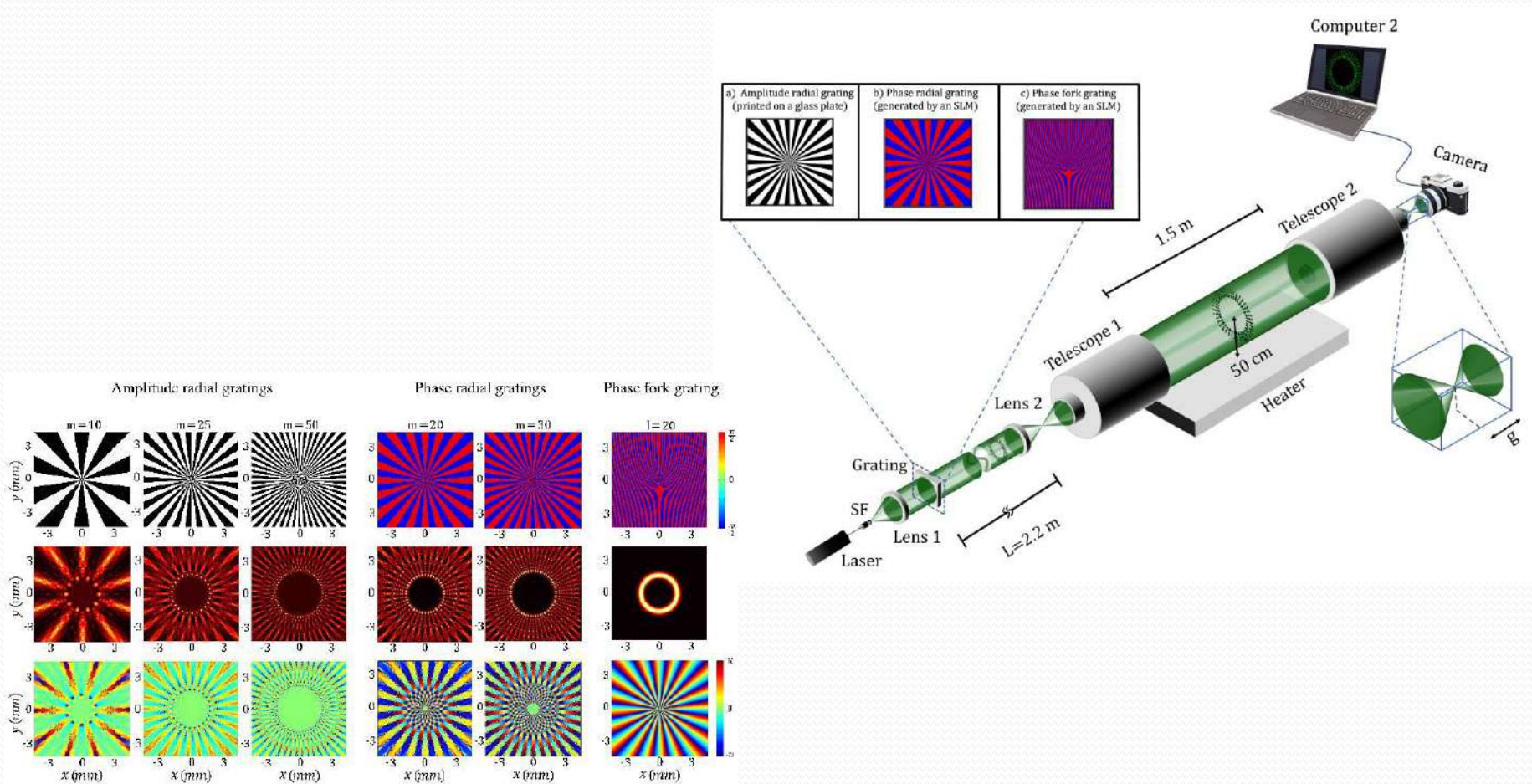
$$l = 1, 2, 3, \dots$$

or

$$l = 1, 3, 5, \dots$$



Resilience of radial carpet beams under propagation through indoor convective air turbulence



Resilience of radial carpet beams under propagation through indoor convective air turbulence

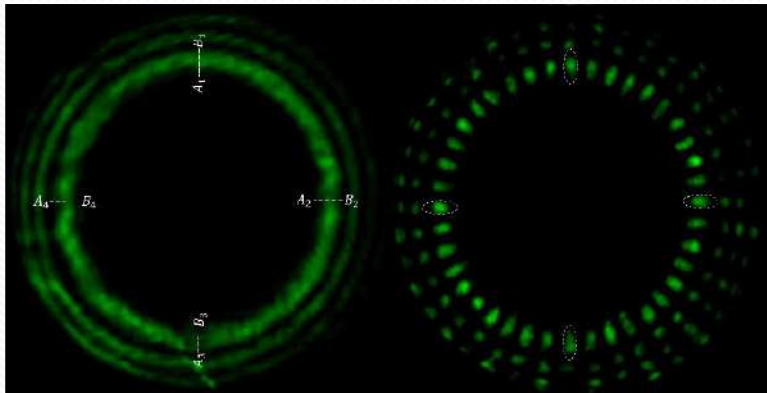
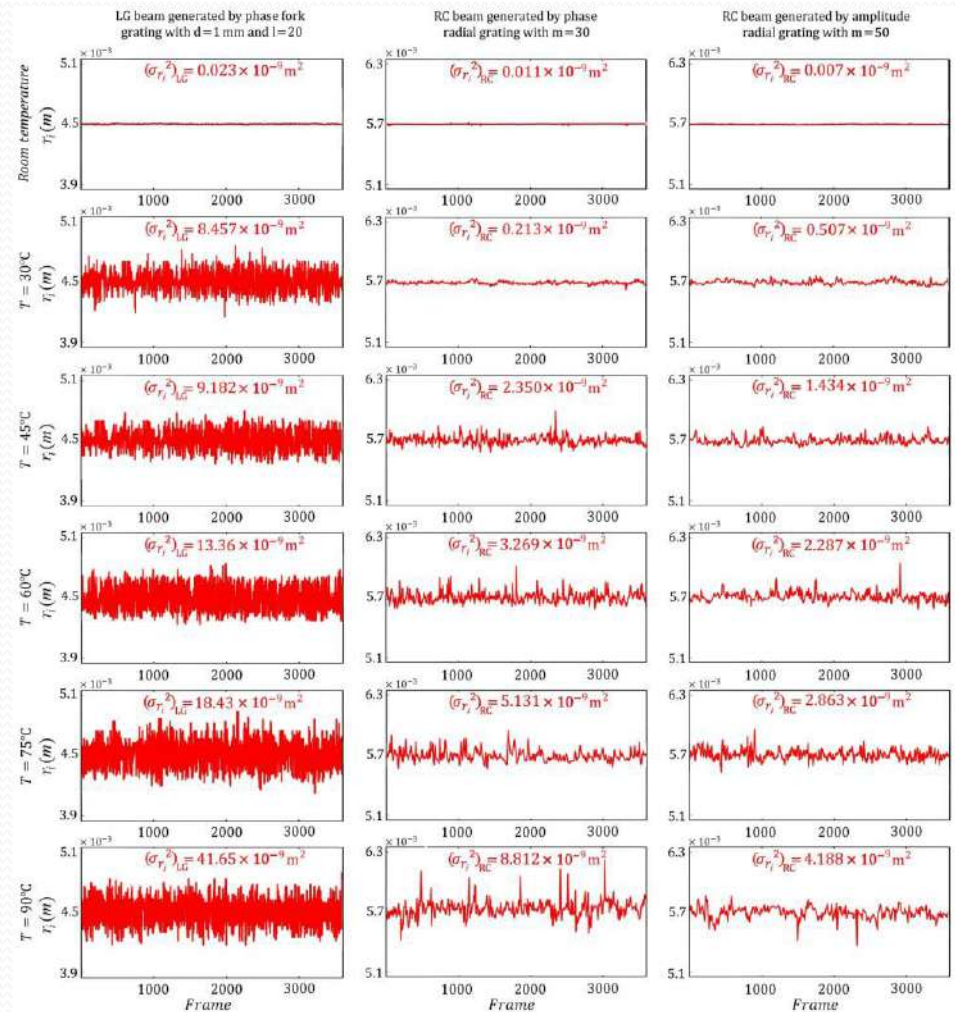
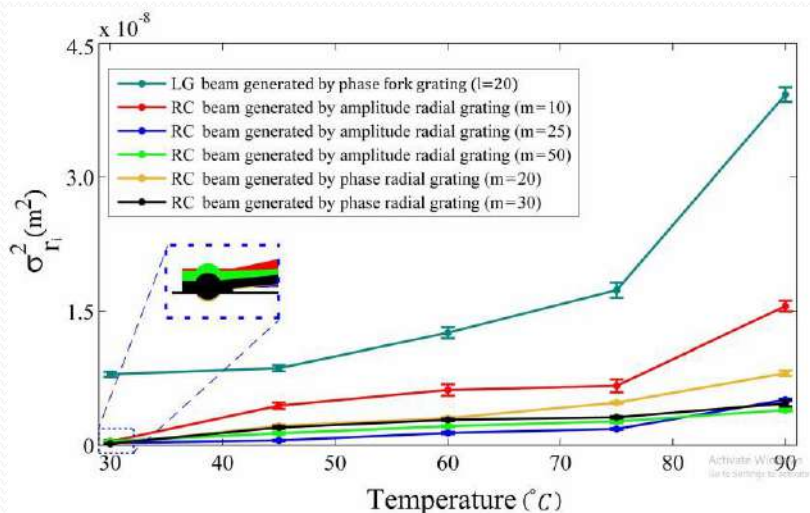


Illustration of location of four points on the beams' cross sections used for the measurement of the displacements. (the LG beam was generated by a phase fork grating with $l = 20$, and the RC beam was generated by a phase radial grating with $m = 20$ under plane wave illumination (both of the gratings are generated by the SLM). The temperature of the heater was 45 C.

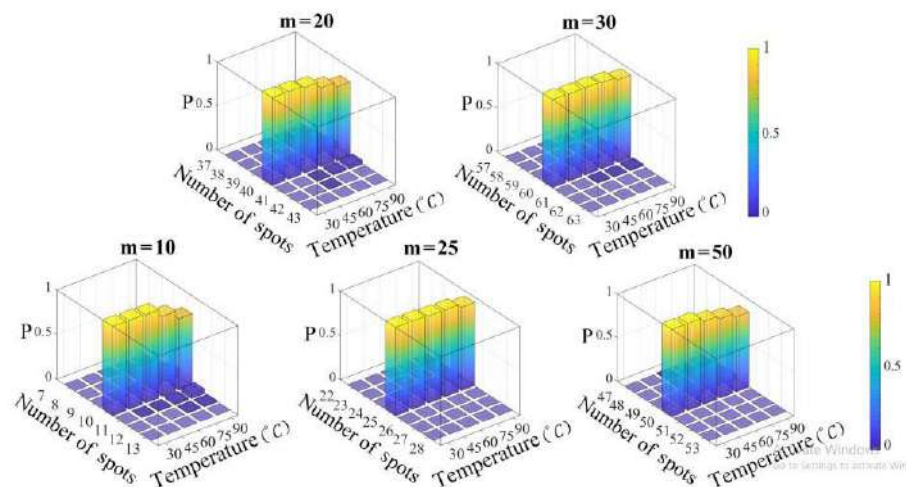


Resilience of radial carpet beams under propagation through indoor convective air turbulence



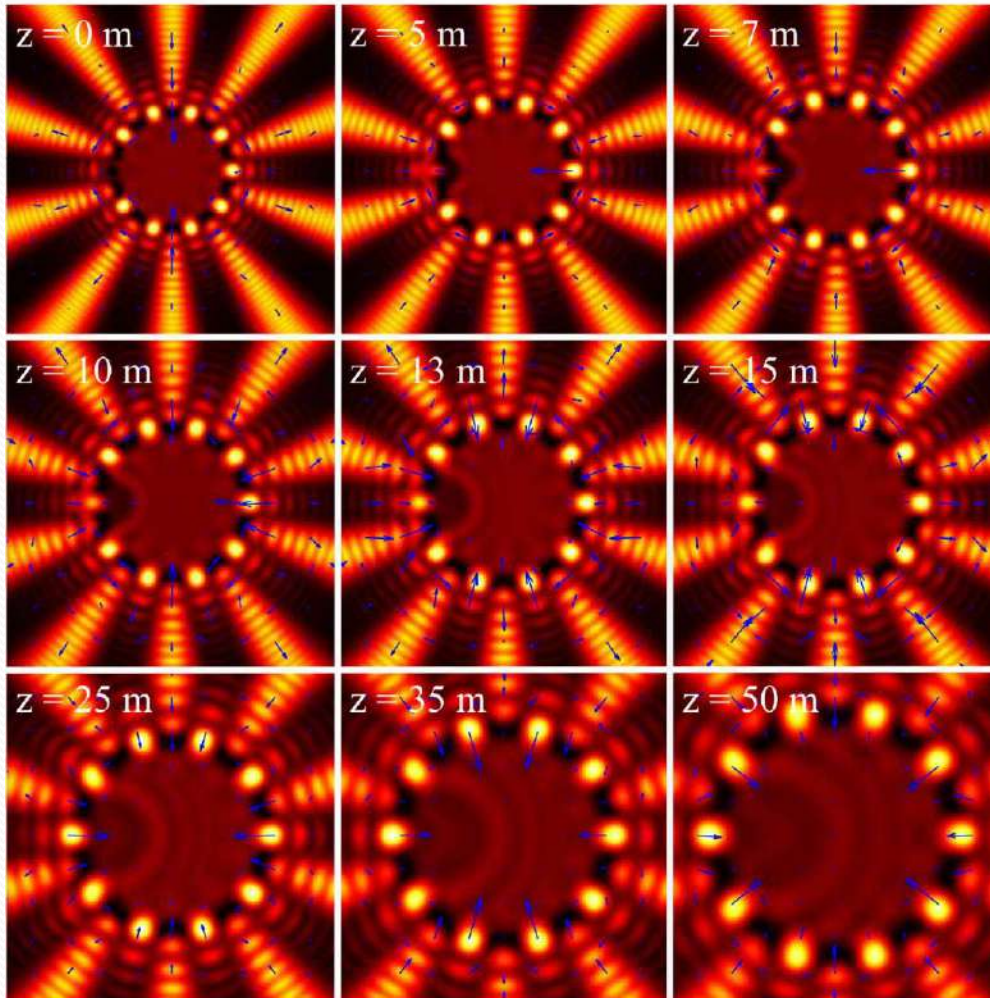
Calculated variance of r_i for the LG and RCBs at different temperatures of the heater

Although there are slight changes in the RCBs transverse intensity distribution, the number of the main intensity spots rarely changes. This feature makes the RCB a good candidate for the transmission of information.



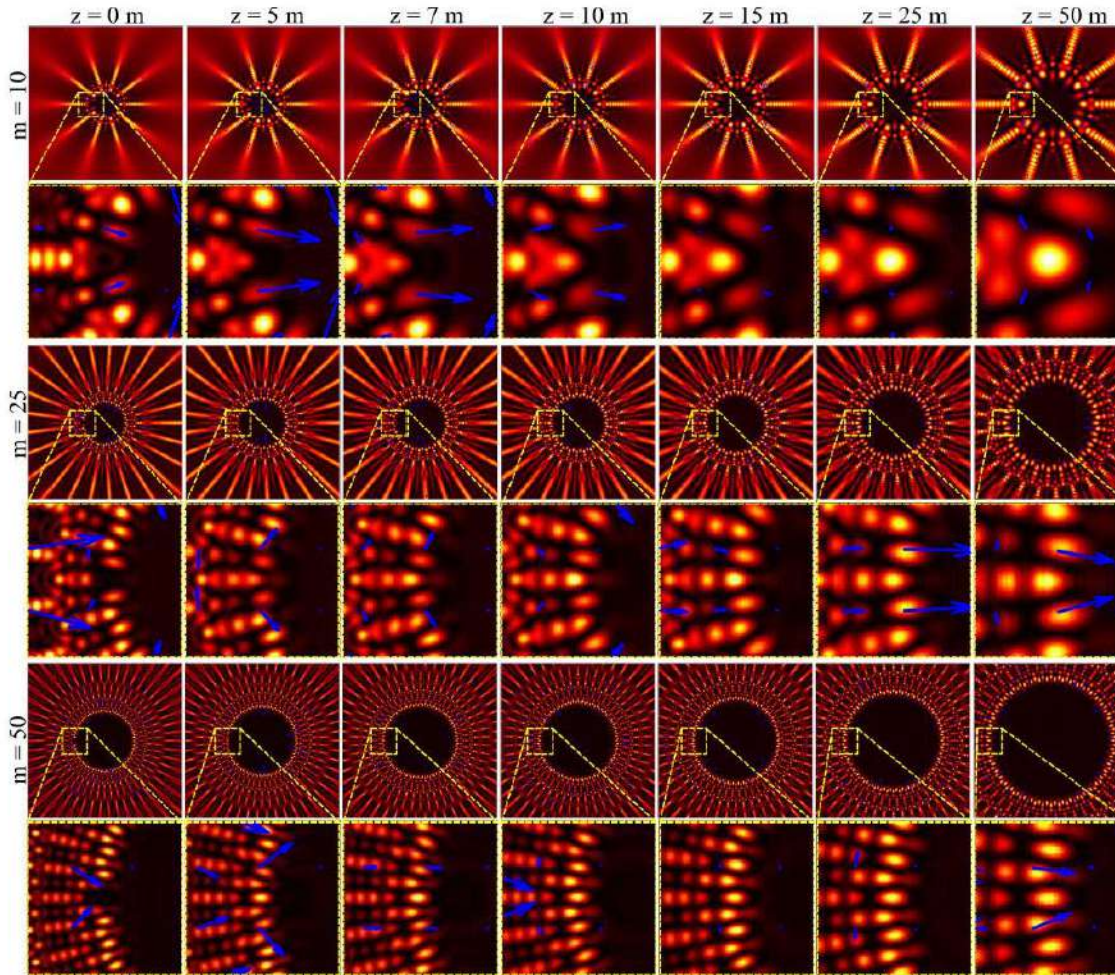
Relation of the number of the main intensity spots of the generated RCBs at the entrance plane and at the received plane at the end of turbulence medium for different values of the heater temperature. The first (second) row shows the results of the RCBs generated with phase (amplitude) radial gratings.

A quantified approach for estimating the strength of self-healing of RCBs is in terms of the beams' specifications



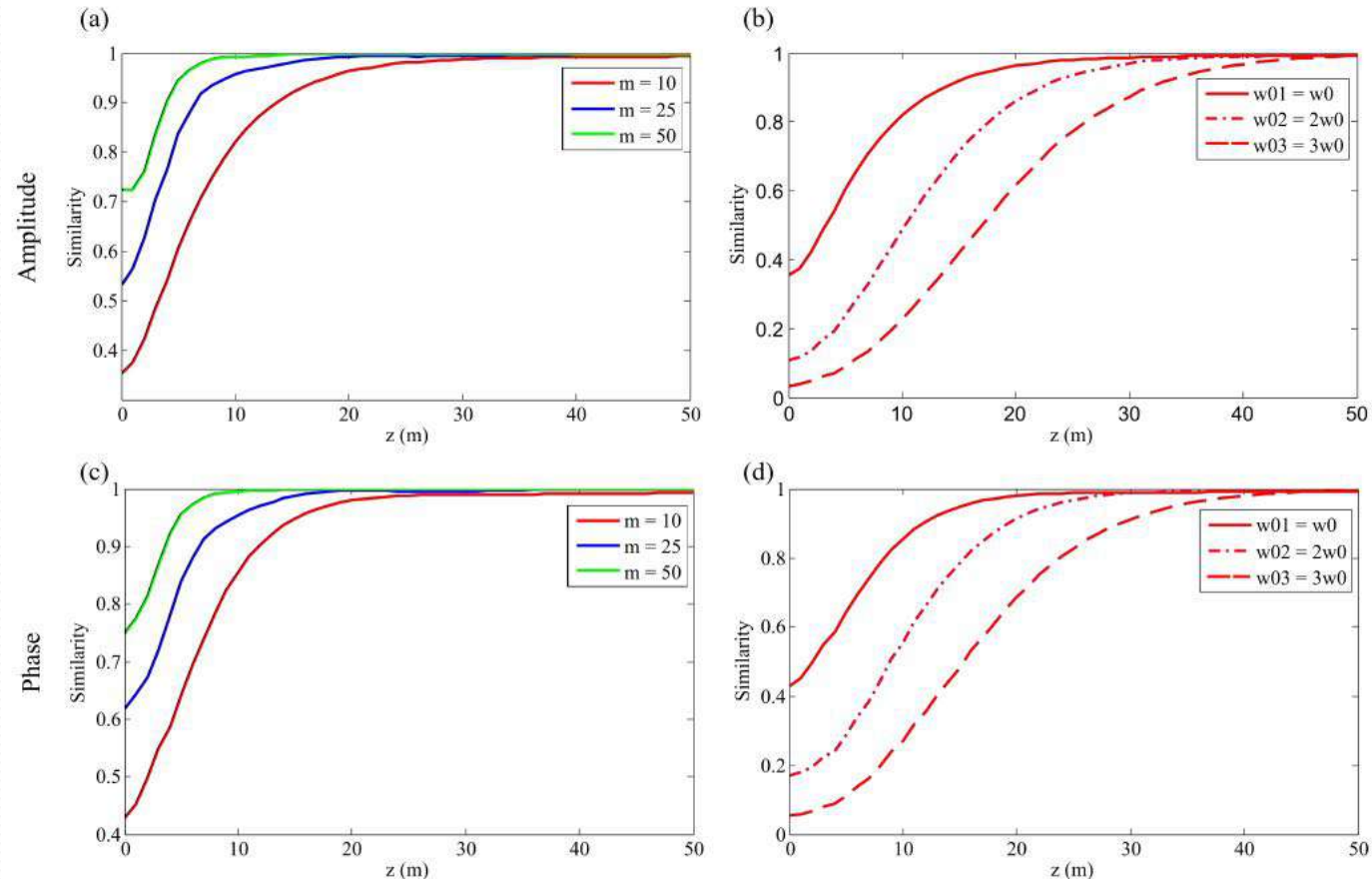
Transverse power flows (blue arrows) of a disturbed RCB with $m = 10$ after passing through of a finite opaque obstacle with a Gaussian absorption coefficient, at several propagation distances.

A quantified approach for estimating the strength of self-healing of RCBs is in terms of the beams' specifications



Self-healing of a RCB under propagation, which is generated in the diffraction of a plane wave from a radial phase grating having a sinusoidal profile and one of the main spots is blocked. Insets show enlarged intensity profiles of the neighborhood lobes at different propagation distances.

A quantified approach for estimating the strength of self-healing of RCBs is in terms of the beams' specifications



(a) Calculated similarity of the RCBs with different spoke numbers m . (b) With different w_0 of the Gaussian mask for $m = 10$ ((a),(b) similarities for RCBs produced in the diffraction of a plane wave from an amplitude radial grating).(c) Similarity of the RBBs with different spoke numbers m . (d) With different w_0 of the Gaussian mask for $m = 10$ ((c),(d) similarities for RCBs produced in the diffraction of a plane wave from a phase radial grating).

Summery and Conclusion:

- *It is shown that, in the diffraction of a plane wave from an amplitude radial grating, the boundaries of geometric shadow, near- and far-field diffraction regimes to be curved.*
- *Talbot carpet can be generated at the transverse plane in the diffraction of a plane wave from an amplitude radial grating.*
- *“Diffraction-based rainbow” was introduced and formation of colorful radial Talbot carpet at the transverse plane is investigated. An exceptional sample of spectrum-invariant propagation is also presented.*
- *An azimuthally-modified linear phase grating was introduced and generation of varied radial carpet beams over the different diffraction orders with controlled intensity sharing among the generated beams was presented.*
- *Existence of the self-imaging in the polar coordinates for the azimuthally periodic Bessel-based structures was proved.*
- *“Combined half-integer Bessel-like beams” were introduced and It was shown that, this family of beams satisfies a “radial structured” boundary condition at $z = 0$ plane, therefore they can be produced by the diffraction of a plane wave from suitable “radial structures.”*
- *The use of RCBs for “multiple particle trapping” was presented.*
- *A comparison the propagation of Laguerre-Gaussian (LG) and RCBs through an indoor convective air turbulence under weak to strong turbulence conditions was presented, and it was shown that the RCB experiences less disturbance and is more resilient to turbulence, especially when it has a complicated structure. It is also shown that a set of RCBs having different values of the main intensity spots can be used as an orthogonal bases for free-space optical communication.*
- *The strength of self-healing of RCBs is quantified in terms of the beams’ specifications.*

Thank you for your attention.

Any questions and suggestions!